

# Integration of a Multi Reflection Time of Flight Isobar Separator into the TITAN Experiment at TRIUMF

by

Andrew Finlay

B.Sc., University of Guelph, 2014

A THESIS SUBMITTED IN PARTIAL FULFILLMENT OF  
THE REQUIREMENTS FOR THE DEGREE OF

MASTER OF SCIENCE

in

The Faculty of Graduate Studies

(Physics)

THE UNIVERSITY OF BRITISH COLUMBIA

(Vancouver)

August 2017

© Andrew Finlay 2017

# Abstract

The TITAN experiment at TRIUMF performs high-precision mass measurements on rare isotopes using Penning trap mass spectrometry. A major challenge is the presence of isobaric contamination introduced by the rare isotope production process. To remove these a new Multi-Reflection Time-of-Flight (MR-ToF) mass spectrometer and isobar separator has been integrated into the TITAN system.

To facilitate the integration of the MR-ToF the TITAN beamline has been studied using a combination of computer based ion optics simulations and experimental measurements. Simulations were benchmarked against a measurement of the ion beam's transverse emittance using an Allison meter, and beam time profiles measured with multichannel plate detectors. Computer models were found to be able to reproduce experimental results within a factor of 2. The key source of differences appears to be the modeling of the cooler buncher TITAN uses for beam preparation.

Simulations were used to identify optimal settings on ion optical elements to facilitate the maximum efficiency of ion transport into the MR-ToF and from the MR-ToF to the measurement Penning trap. Additional tests of the impact of new optics on the beamline when bypassing the MR-ToF show beam properties before and after the changes to be identical within uncertainty. Suggested settings have successfully been used to guide the injection of ions into the MR-ToF.

Once the MR-ToF was installed in the TITAN system, tests were performed to demonstrate the functionality of the MR-ToF using externally produced beam. The ISAC Off-Line Ions Source was used to produce a  $^{40}\text{Ar}^+$  ion beam for testing. This was merged with  $^{40}\text{K}^+$  ions from the MR-ToF internal ion source to demonstrate the resolving power of the MR-ToF. Mass measurements were performed at a resolving power of 200 000, exceeding performance expectations by a factor of 2. Isobar separation was used to remove either Ar or K, requiring a mass resolving power  $\geq 25000$ . The MR-ToF is now a functioning part of the TITAN system, and has already been used to perform mass measurements of rare isotopes.

# Lay Summary

The TITAN experiment at TRIUMF uses ion traps to very quickly perform mass measurements of short-lived rare isotopes, providing insights into nuclear structure and astrophysics. A major challenge in this work is the presence of contaminants mixed with the ionized isotopes being measured. To filter these out we have added a device called a Multi-Reflection Time-of-Flight (MR-ToF) mass spectrometer.

Preparing for this integration, computer simulations were used to study the passage of ions inside the TITAN system. These were validated with experimental measurements, then used to calculate settings which would best allow the efficient movement of ions into and out of the MR-ToF. Finally the MR-ToF was tested with ion beams produced externally from TITAN to demonstrate the operating abilities of the MR-ToF. Here the MR-ToF was shown able to identify and remove contaminants at a resolution exceeding design expectations.

# Preface

The experimental work of this thesis was carried out at TRIUMF's Ion Trap for Atomic and Nuclear science (TITAN) experimental facility in Vancouver, BC.

Simulations of the TITAN cooler buncher described in Chapter 3 are based on a reproduction of code developed by M. Smith with buffer gas code rewritten by D. Short. Experimental work in Chapter 3 and 4 was lead by C. Babcock and M.P. Reiter respectively. I was a contributing member of during the preparation and data collection process. Data analysis presented is my own.

Figures 1.4, 4.1, 1.6, 1.5 and 4.2 reproduced with permission.

# Table of Contents

<b>Abstract</b>	ii
<b>Lay Summary</b>	iii
<b>Preface</b>	iv
<b>Table of Contents</b>	v
<b>List of Tables</b>	vii
<b>List of Figures</b>	viii
<b>Acknowledgements</b>	xiv
<b>Dedication</b>	xv
<b>1 Introduction</b>	1
1.1 Penning traps	1
1.1.1 Ion motion	1
1.1.2 Mass measurement	2
1.1.3 Preparation traps	3
1.2 Paul traps	3
1.3 Multi-Reflection Time-of-Flight mass spectrometer and isobar separator	4
1.4 Beam purity	4
1.5 TITAN Experiment	6
1.5.1 ISAC Facility	6
1.5.2 Cooler Buncher	7
1.5.3 EBIT	7
1.5.4 Measurement Penning trap	7
1.5.5 TITAN MR-ToF	9
1.6 Outline of this thesis	9
<b>2 Principles of ion transport needed for MR-ToF integration</b>	11
2.1 Understanding beam dynamics using emittance	11
2.1.1 Transverse emittance	13
2.1.2 Longitudinal emittance	14
2.1.3 Acceptance	14
2.2 Ion optics	15
2.2.1 Electrostatic	16
2.3 Radio Frequency Quadrupole Optics	24
2.3.1 RF Ion Guides	25

2.3.2	Linear Paul Traps . . . . .	28
2.4	Summary . . . . .	31
<b>3</b>	<b>Beamline studies for MR-ToF integration . . . . .</b>	<b>34</b>
3.1	The TITAN beamline prior to integrating the MR-ToF . . . . .	34
3.1.1	Beamline simulations . . . . .	36
3.1.2	Allison meter emittance measurements . . . . .	38
3.1.3	Beam time profiles . . . . .	44
3.2	MR-ToF integration . . . . .	49
3.2.1	Beamline modification for MR-ToF . . . . .	49
3.2.2	MR-ToF acceptance . . . . .	49
3.2.3	Beam profiles out of the MR-ToF . . . . .	55
3.2.4	Bypassing the MR-ToF . . . . .	58
3.3	Summary . . . . .	58
<b>4</b>	<b>First tests of MR-ToF integrated into TITAN . . . . .</b>	<b>61</b>
4.1	Tests of MR-ToF with OLIS beam . . . . .	61
4.1.1	Ion transport efficiency . . . . .	62
4.1.2	Mass measurement . . . . .	62
4.1.3	Isobar separation . . . . .	66
4.2	Summary . . . . .	69
<b>5</b>	<b>Summary and outlook . . . . .</b>	<b>71</b>
<b>Appendices</b>		
<b>A</b>	<b>Introduction to SIMION . . . . .</b>	<b>80</b>
<b>B</b>	<b>Experimental operating parameters for emittance and time profile measurements . . . . .</b>	<b>81</b>
<b>C</b>	<b>Allison meter data analysis methodology . . . . .</b>	<b>83</b>
<b>D</b>	<b>Allison meter data analysis Lua code . . . . .</b>	<b>86</b>

# List of Tables

3.1	A summary of the labels and corresponding purpose for the ion optics and apertures in the TITAN beamline. Positions of these are indicated in Figure 3.1. . . .	36
3.2	Comparison of CB simulation results produced for this thesis to results obtained in [65]. Differences between the simulations range from 1% to 35%. Unit convention for reporting transverse emittance follows that of [65]. . . . .	37
4.1	Literature masses [79] for isotopes of K and Ar used for calibration and comparison.	65
4.2	Comparison of the measured mass of $^{40}\text{K}^+$ to the literature mass reported in Reference [79]. . . . .	66
B.1	A summary of the voltages applied to the TITAN beamline electrodes for the time-profile measurements discussed in Section 3.1.3. Positions of the electrodes in the TITAN beamline are indicated in Figure 3.1. . . . .	82

# List of Figures

1.1	An overview of a Penning trap structure and the motion of a trapped ion. a) A diagram of a Penning trap showing a typical electrode structure with the applied voltages and magnetic field. b) Calculated motion of an ion in a Penning trap highlighting the components of the ion motion: cyclotron $\omega_+$ (yellow), magnetron $\omega_-$ (blue), axial $\omega_z$ (green), and combined (black). . . . .	2
1.2	Diagrams of two Paul trap designs showing the electrode structure and an example of typical driving voltages. . . . .	4
1.3	Outline of the principle of time-of-flight mass spectrometry showing three ions becoming separated over a given time of flight. Top: Flight over long distance. Middle: Flight over same distance as top, but fit into smaller physical space through multiple reflections. Bottom: Time of flight spectrum at start and finish of the above mass separations. . . . .	5
1.4	A schematic overview of the TITAN experiment a) before the MR-ToF and b) with the MR-ToF installed. Arrowed lines are used to indicate paths the ion beam may take to TITAN from the ISAC ion sources, inside TITAN, or from TITAN to the ISAC collinear laser spectroscopy experiment. . . . .	7
1.5	Diagrams of TITAN EBIT showing: a) Components of the trap along the beam axis, with the path of ions indicated by a black double arrow. b) The arrangement of SiLi gamma-ray detectors around the trapping region. Figures found in [39]. . . . .	8
1.6	Schematic of the MR-ToF and its interface with the TITAN beamline. Ion optical electrodes are indicated in yellow; the MR-ToF vacuum chamber is highlighted in green; detectors are shown in blue; red arrowed lines are used to indicate possible beam paths through the TITAN beamline and MR-ToF. . . . .	10
2.1	Example of a) an elliptical emittance and b) a filamented emittance. . . . .	12
2.2	Top: Visualisation of transverse emittance at different positions of a beam, for where the beam is converging, at a focus point (beam waist), and when it is diverging. Bottom: Example plots of the transverse emittance for the positions indicated by the blue dashed line over each plot. The left plot includes a direct illustration of the relation between the spatial distribution $\Delta x$ and beam divergence $\Delta x'$ to the trace-space plot. As shown, the orientation of the ellipse changes and in real scenarios it may change shape, but the total area is invariant for constant beam energy in a vacuum. . . . .	13

2.3	An example of a time focus for a distribution of particles. Top: Illustrated here are a set of particles moving with different velocities represented by right pointing arrows. Represented are three moments in time as the faster particles start behind the slower particles then move to overtake the slower particles. The moment where the faster particles are passing the slower is known as the time focus. Bottom: For each moment in time, an example of a corresponding longitudinal emittance plot is shown. . . . .	14
2.4	An example phase space plot where device acceptance is greater than beam emittance but their orientations cause them not to match. The unmatched portion of the beam will be lost, resulting in a lower beam transport efficiency. Such a mismatch may be eliminated through the use of ion optical lenses to re-orient the beam emittance into alignment with the acceptance. . . . .	15
2.5	Simulations of ion trajectories (red lines) and ion optical elements (brown) for an Einzel lens showing a) an isometric view of the lens and the ion trajectories. b) and c) show the Einzel lens operating with a decelerating and accelerating potential respectively, along with contour lines of the electric potential (black curves). The example here shows a parallel beam being focused to a point, the position of which is determined by the potential $V_{Lens}$ . Ion trajectories portrayed here are from ions flying from left to right. Simulations produced in SIMION [50].	17
2.6	Examples of parallel plate bender designs. a) A simple rectangular plate design, used in TITAN for small beam path corrections, up to $9^\circ$ . b) A $90^\circ$ cylindrical bender, and c) a $90^\circ$ spherical bender. The direction of the electric field between the bender plates is indicated by the blue arrows. . . . .	19
2.7	An illustration of how the time focus is shifted by an electrostatic mirror. Dashed lines indicate the trajectories followed by individual ions. Ellipses are drawn around the ions to indicate snapshots in time, showing the process of the time shift. The direction of the electric field is indicated with the blue lines, though this field would be present through the mirror. . . . .	20
2.8	Simulation of an electrostatic mirror using a grid electrode. Ion trajectories (red) start on a) the left, b) the top. Ion collisions with the grid electrode (brown) or the boundary of the simulation area are marked in green. Electric potential contour lines are shown in black in b). Simulation produced in SIMION [50]. . .	21
2.9	Schematic of the TITAN MR-ToF ion optics. . . . .	21
2.10	An illustration of the time focus shift (TFS) in the TITAN MR-ToF from injection into the MR-ToF to setting a final time focus on a detector. . . . .	22
2.11	Cross-sectional diagram of a typical quadrupole lens with a potential focusing in the $x$ -direction. a) The arrangement of physical rods with the applied electric potentials. b) A simulation of the resulting electric potential distribution produced in SIMION [50]. . . . .	23
2.12	Different views of a simulation of ion trajectories (red) through a quadrupole quadruplet (brown). Trajectories are shown for ions flying left to right parallel to the $z$ -axis. Black contour lines indicate the electric potential around the electrodes. Simulation produced in SIMION [50]. . . . .	23
2.13	Schematic of radio frequency quadrupole (RFQ) rods and their applied bias. Also shown is the radius between rods $r_0$ . . . . .	24

2.14	Simulated radial ion motion in an RFQ as a function of time for different q-values. Here an ion of mass 133 u is simulated in a trap with $r_0 = 10$ mm operated at a frequency of 1 MHz with the voltage varied to change the q-value. Simulations produced in SIMION [50]. . . . .	25
2.15	Two schematics and corresponding linear potentials of RFQ ion guides. . . . .	27
2.16	Images of RFQ switchyard. a) Photo of the switchyard partially assembled. The carbon-doped plastic electrodes are visible here. b) Rendered model showing the phases of the applied biases on the switchyard in red and blue. . . . .	28
2.17	Diagrams of the RF switchyard ion guide indicating relative strengths of the DC potentials to allow ions to pass through the switchyard in: a) a straight path, b) a $90^\circ$ path, or c) merge beams from two directions into a single path. . . . .	29
2.18	TITAN beamline electrostatic switchyard. . . . .	29
2.19	Top: Schematic of a linear Paul trap based on segmented rods. Bottom: Example of linear potential used to trap ions. . . . .	30
2.20	Schematic of the TITAN cooler buncher [34] electrode configuration. a) The arrangement of 24 rod segments which can each be given a different DC potential. Ions are trapped in the region of segment 23, then segments 22 and 24 are switched to allow ions to escape the trap and be directed into the TITAN beamline. b) A SIMION [50] calculation of the DC potential for cooling (blue) and ejection (red) as a function of linear position in the CB. . . . .	32
3.1	Schematic overview of the TITAN beamline optics between the Cooler Buncher and MPET as relevant for simulations presented herein. Electrodes are labelled first with a section label, then the optics type and assigned number. Electrode types are summarized in Table 3.1. Black lines appearing before and after many electrostatic optics are “skimmer” plates. Red arrows indicate the beam path and direction. The MR-ToF and EBIT optics are not shown. . . . .	35
3.2	Two examples of how a 5 mm diameter circular aperture is modelled in SIMION at different resolutions. . . . .	37
3.3	Schematic diagrams of an Allison meter used for measuring beam transverse emittance. Red lines indicate example paths of individual ions passing through the meter; the solid line shows a transmitted ion and the dashed line indicates a) an ion entering along a path which will not pass through the meter, or b) an ion which passes through the detector at the very edge of the detector slit. . . . .	39
3.4	Detected signals at MCP-1 and the Allison MCP as a function of time. Various peaks are indicated. Highlighted are the interpretations of specific peaks in the time-of-flight spectrum as well as the sections of data used to produce the emittance measurement. This example is an integration of all the time profiles for a specific measurement. . . . .	40
3.5	Detected MCP signal as a function of time as function of Measurement Index for a complete Allison meter emittance measurement. Individual time profiles are presented as density plots parallel to the $y$ -axis. The time profiles are arranged horizontally in the order they were taken. Integrated projections of the data along the $x$ - and $y$ -axes are shown above and to the right of the density plot. Allison meter MCP signal can be seen as dots at approximately $68 \mu\text{s}$ . . . . .	41

3.6	Emittance plots from one measurement of a $^{133}\text{Cs}^+$ beam out of the TITAN CB with a standard operating parameters (described in text), showing different levels of processing of the number of ions detected at each position and divergence. a) An emittance plot with no processing of the ion counts, showing a large biasing effect due to drift in the MCS. b) An emittance plot with ion count normalization and time-profile background removed, but before a threshold was set to remove background counts for rms emittance calculation. c) The same emittance plot as b), but scaled in the z-axis to highlight the degree of variation of the background counts. Background variations on the level of 2% of the peak ion counts can be seen. d) An emittance plot after the complete ion-count processing described in the text. This plot includes the calculated rms emittance and Twiss parameters. A white ellipse calculated from the Twiss parameters is overlaid on the plot with the size set by the equivalent emittance $4\epsilon_{rms}$ . . . . .	42
3.7	A simulation of the Allison meter emittance measurement of the TITAN CB beam shown in Figure 3.6. Left: SIMION simulation of ion trajectories (red) with collision points (green) and ion optical elements (brown). Right: Emittance plot with rms emittance, Twiss parameters, and the ellipse calculated from the Twiss parameters for equivalent emittance ( $4\epsilon_{rms}$ ) overlaid in white. For this simulation frequency was set at 480 kHz with a peak-to-peak voltage of 170 V, a gas pressure of $10^{-2}$ mbar, and temperature of 300 K. . . . .	44
3.8	A comparison of simulated and experimental time-profiles obtained at MCP-1 (top) and MCP-0 (bottom). . . . .	46
3.9	A SIMION simulation of the TITAN beamline between the CB and MPET. Beam trajectories are shown in red and points where ions collide with electrodes or reach the position of MCP-0 are marked in green with notable loss points circled in green. Most losses occur at TSYBL:DPA. . . . .	47
3.10	A plot of the change in transverse rms emittance as a function of beam time of flight from the CB. . . . .	47
3.11	Simulated trajectories (red) of ions passing through the differential pumping aperture TSYBL:DPA, and the points at which some ions collide with the aperture structure (green). Trajectories are going right to left here. Simulations produced in SIMION [50]. . . . .	48
3.12	Photos of the split Einzel lens added to the TITAN beamline to facilitate high ion transport efficiency into the MR-ToF. Top: SEL prior to installation. Bottom: SEL installed in its location in the TITAN beamline. . . . .	50
3.13	An example of the portion of trace-space tested (test area) and acceptance simulated in the investigation of the acceptance of the MR-ToF input optics. . . . .	51
3.14	SolidWorks model of the MR-ToF input optics indicating the electrode nomenclature. . . . .	52
3.15	Samples of the acceptances simulated for the MR-ToF input optics across a range of chosen voltages. Numerical estimates of the acceptance are shown in the upper right corner of each plot. For this investigation the voltages on S-In-A1 and S-In-Lens were varied. Other voltage settings are indicated in the text. . . . .	54
3.16	Simulated phase space of beam emittance (green) from the CB overlapped with the device acceptance (blue) of the MR-ToF input optics. This was achieved with EL5 set at -1650 V, SEL at -400 V, In-Lens at -1050 V and In-A1 at 800 V. . . . .	55
3.17	SolidWorks model of the MR-ToF output optics indicating electrode nomenclature. . . . .	56

3.18	Simulations of, Left: expected time-of-flight peak (blue) and, Right: energy spread (green) from the MR-ToF output optics detected at the position of MCP-0 for a beam energy of 1.3 keV. Gaussian fits of the data are shown with key results on each plot. Results with Out-Lens at -1900V, B4-OUT at 1225 V, Out-A1 at 1100 V and Out-A2 at 1000 V. . . . .	57
3.19	Simulated longitudinal emittance of beam ejected from the MR-ToF and detected at MCP-0 for a beam energy of 1.3 keV. This for the ion optical settings: Out-Lens at -1900V, B4-OUT at 1225 V, Out-A1 at 1100 V and Out-A2 at 1000 V. . . . .	57
3.20	A comparison of transverse emittance simulated after the 90° bend in the TITAN beamline and before TSYBL:DPA without and with the new optics for ion transmission into the MR-ToF. . . . .	59
4.1	A schematic overview of the TITAN experiment a) before the MR-ToF and b) with the MR-ToF installed. Arrowed lines are used to indicate paths the ion beam may take to TITAN from the ISAC ion sources, inside TITAN, or from TITAN to the ISAC collinear laser spectroscopy experiment. . . . .	62
4.2	Schematic of the MR-ToF and its interface with the TITAN beamline. Ion optical electrodes are indicated in yellow; the MR-ToF vacuum chamber is highlighted in green; detectors are shown in blue; red arrowed lines are used to indicate possible beam paths through the TITAN beamline and MR-ToF. . . . .	63
4.3	Photo of the MR-ToF installed and connected to the TITAN beamline. . . . .	64
4.4	Time-of-flight spectrum of potassium isotopes used to calibrate the MR-ToF mass measurements. . . . .	65
4.5	Three MR-ToF time-of-flight spectra used for mass measurements. Detected ions are marked in the plots; these ions were identified based on their mass. Time-of-flight mass measurements for each spectrum were calibrated use the $^{40}\text{Ar}^+$ peak. For the bottom spectrum $^{40}\text{K}^+$ was added to the beam using the MR-ToF internal ion source. . . . .	67
4.6	An example of mass-selective re-trapping performed in the TITAN MR-ToF using $^{40}\text{Ar}^+$ and $^{40}\text{K}^+$ ions. a) Number of ions detected for $^{40}\text{Ar}^+$ (blue) and $^{40}\text{K}^+$ (red) time-of-flight peaks for different re-trapping times. b) Time-of-flight spectra showing no re-trapping (black), then with different re-trapping times to capture either $^{40}\text{Ar}^+$ (blue) or $^{40}\text{K}^+$ (red) while removing the other isobar. . . . .	68
4.7	An example of ion motion in relation to axial potential during the process of isobar separation through re-trapping. Left: Retarding field slowing ions prior to trapping. Right: Shallow potential well applied to trap ion of interest. Ions are represented in red with the ion of interest and contaminant are represented as $m_1$ and $m_2$ respectively. Axial potentials are represented as blue lines. . . . .	69

C.1	Emittance plots from one measurement of the beam out of the TITAN CB with the current standard tune, showing different levels of processing of the number of ions detected at each position and divergence. a) An emittance plot with no processing of the ion counts, showing a large biasing effect due to drift in the MCS. b) An emittance plot with ion count normalization and time-profile background removed, but before a threshold was set to remove background counts for rms emittance calculation. c) The same emittance plot as b), but scaled in the z-axis to highlight the degree of variation of the background counts. Background variations on the level of 2% of the peak ion counts can be seen. d) An emittance plot after the complete ion count processing described in the text. This plot includes the calculated rms emittance and Twiss parameters. A white ellipse calculated from the Twiss parameters is overlaid on the plot with the size set by the equivalent emittance $4\epsilon_{rms}$ . . . . .	84
C.2	A plot of the calculated rms emittance as a function of the threshold for setting background noise to zero. . . . .	85

# Acknowledgements

My thanks to Pascal Reiter, Jens Dilling, Ania Kwiatkowski, Kyle Leach, Carla Babcock, Devin Short and all the other people in TITAN, TRIUMF, and Giessen who I forgot to mention here.

For my daughter Sonya whose birth gave me a rather compelling motivation to finish this thesis and get on with things.

# Chapter 1

## Introduction

Ion traps at rare-isotope-beam (RIB) facilities are increasingly popular for beam preparation and measurements [1]. Ion traps are either directly used for or assist in making measurements of atomic masses, decay properties, and nuclear moments. Such information is essential in probing nuclear structure of exotic species and understanding the nuclear decays and reactions which fuel stars. By utilizing the comprehensive theory of electricity and magnetism it is possible to carefully study the interactions of RIBs with electromagnetic fields to extract more details of the properties of individual isotopes.

There are three broad categories of ion traps used in experiments at modern RIB facilities: Penning traps use a combination of electric and magnetic fields to trap ions and perform precision measurements or beam preparation [2][3][4]. Paul or radio frequency (RF) traps use dynamic fields to trap ions and are primarily used at RIB facilities for beam preparation [5][6][7]. Multi-Reflection Time-of-Flight (MR-ToF) mass spectrometers and isobar separators use static electric fields to distinguish ion masses based on their time of flight [8][9]. The last of these is the focus of this thesis.

### 1.1 Penning traps

In RIB facilities Penning traps are primarily used for mass measurements to a relative precision of  $\frac{\delta m}{m} \sim 10^{-9}$ . The requirements for ion confinement in a Penning trap are an electric field providing axial confinement and a magnetic field confining ions radially. Typically the electric field is produced by a set of three electrodes in a radially symmetric quadrupolar arrangement where two end caps are biased higher than a middle electrode (Figure 1.1 a). Alternatively, a series of cylindrical electrodes may be used to approximate the necessary quadrupolar electric field [10]. To prevent ions from escaping in the radial direction an axial magnetic field is applied to curve ion paths away from the trap edges. Together the electric and magnetic field can ideally confine ions indefinitely in static fields.

#### 1.1.1 Ion motion

To describe ion motion within a Penning trap we start with the cyclotron motion due to the magnetic field. This motion occurs in a magnetic field with a frequency  $\nu_c$  (or expressed as an angular frequency  $\omega_c = 2\pi\nu_c$ ). The cyclotron frequency is determined as,

$$\omega_c = \frac{Qe}{m}B, \quad (1.1)$$

in which  $Q$  is the charge state of the ion,  $e$  is the elementary charge,  $B$  is the magnetic field strength, and  $m$  is the mass of the charged particle.

The cyclotron motion of ions in a Penning trap is complicated by the electric field. The interaction of ions in the presence of magnetic and electric fields within a Penning trap may be described analytically if the electric potential takes the form of a quadratic saddle potential.

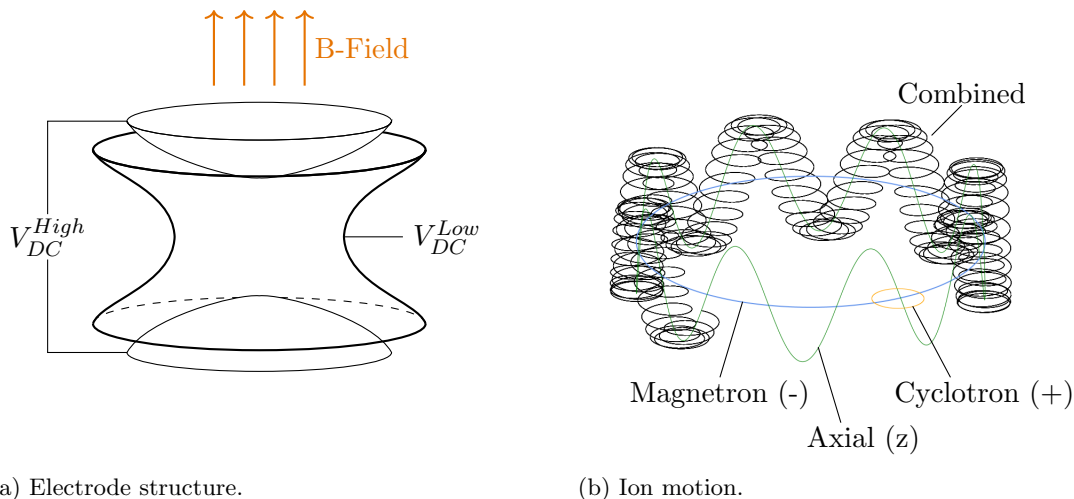


Figure 1.1: An overview of a Penning trap structure and the motion of a trapped ion. a) A diagram of a Penning trap showing a typical electrode structure with the applied voltages and magnetic field. b) Calculated motion of an ion in a Penning trap highlighting the components of the ion motion: cyclotron  $\omega_+$  (yellow), magnetron  $\omega_-$  (blue), axial  $\omega_z$  (green), and combined (black).

Calculated with the origin at the centre of the trap volume this is proportional to  $V(r, z) = r^2 + z^2$ . Such an electric potential will cause the cyclotron motion of the ion in the trap to split into two radial eigenmotions: small reduced cyclotron rotations of frequency  $\omega_+$  and a larger magnetron rotation of frequency  $\omega_-$  (Figure 1.1 b). In addition to the radial motion, ions will have an axial oscillation frequency of  $\omega_z$ . The frequencies of these motions will follow the invariance relations [11],

$$\omega_+ + \omega_- = \omega_c, \quad (1.2a)$$

$$\omega_+ \omega_- = \frac{\omega_z^2}{2}, \quad (1.2b)$$

$$\omega_+^2 + \omega_-^2 + \omega_z^2 = \omega_c^2. \quad (1.2c)$$

### 1.1.2 Mass measurement

High-precision mass measurements are achieved with Penning traps by determining  $\omega_c$ . The primary means of measuring the cyclotron frequency at RIB facilities is the time-of-flight ion-cyclotron-resonance (TOF-ICR) technique [2][12]. The precision of such measurements can be shown to be inversely proportional to the charge state of the ion. Therefore, one means to improve the precision is charge breeding.

Beam purity is an important consideration in Penning trap mass measurements. Contaminant ions simultaneously trapped with the desired species negatively affect the accuracy and precision of its mass determination. This impact on the measurement quality is due to Coulomb interactions between the ions in the trap. For ions of the same mass there is an equal driving field acting on the centre of the cloud, resulting in no frequency shift; however, unequal ion masses will cause frequency shifts [13]. The removal of contaminants is a key motivation to the work of this thesis.

### 1.1.3 Preparation traps

Penning traps have also found applications in improving beam properties prior to injection into a mass measurement Penning trap. For Penning trap mass spectrometry, a number of beam purification techniques have been developed and are discussed in [14] or [15]. These techniques can be broadband with low resolving power or for a specific nuclear state with resolving powers  $R \sim 10^7$  [3]. These traps and techniques are typically used to prepare the beam for TOF-ICR mass determinations.

Penning traps are not however the only ion trap solution available in mass spectrometry and beam preparation. Particularly for beam preparation, Paul traps are an essential tool for ion trapping in a RIB facility.

## 1.2 Paul traps

In contrast to the use of static electric and magnetic fields to trap ions in a Penning trap, purely electric fields may be used to trap ions if they are dynamically changing. An ion trap relying on dynamic electric fields is sometimes referred to as a Paul trap after Wolfgang Paul who invented the first such device [16][17]. Most Paul traps use quadrupole electric fields oscillating at radio frequencies to provide ion confinement. An important property of Paul traps is that only a limited range of ion mass-to-charge ratios can be stably trapped, the precise range being determined by the trap geometry, electrode voltages, and RF frequency. By adjusting the trapping voltages it is possible for a Paul trap to act as a mass filter or mass spectrometer [18].

It is often useful to introduce a neutral buffer gas to a Paul trap to keep ions close to the centre of the trap, reduce the spread of momentum and position (or phase space distribution) of ions ejected from the trap, and thereby improve transport efficiency [18]. These effects are accomplished through collisions between the ions and the buffer gas which can transfer some of the energy from the ions to the gas. Through these collisions the ions tend towards thermal equilibrium with the gas. If the gas is in an open system, maintaining a lower temperature than the ions injected into the trap, the ions become cooled, reducing the phase space of an ion bunch.

Here we shall discuss two examples of Paul trap electrode geometries: 3D, and linear (Figure 1.2). A 3D Paul trap uses the same electrode geometry as a Penning trap, but achieves 3D confinement with an oscillating potential between the ring and endcaps instead of static electric and magnetic fields. However, at RIB facilities the preferred Paul trap design is the linear Paul trap.

A linear Paul trap is composed of four elongated parallel and segmented electrodes, as shown in Figure 1.2 b. The outermost electrodes are biased to axially confine the ions while the quadrupolar RF field traps them radially. With this trap design it is possible to trap larger quantities of ions than in a 3D Paul trap, which can be useful for the accumulation of a continuous charged particle beam into bunches. If we introduce a buffer gas to the trap we now have the basis for a cooler buncher which is an important use of Paul traps at RIB facilities. A cooled and bunched beam improves, for example, the measurement quality in Penning trap mass spectrometry.

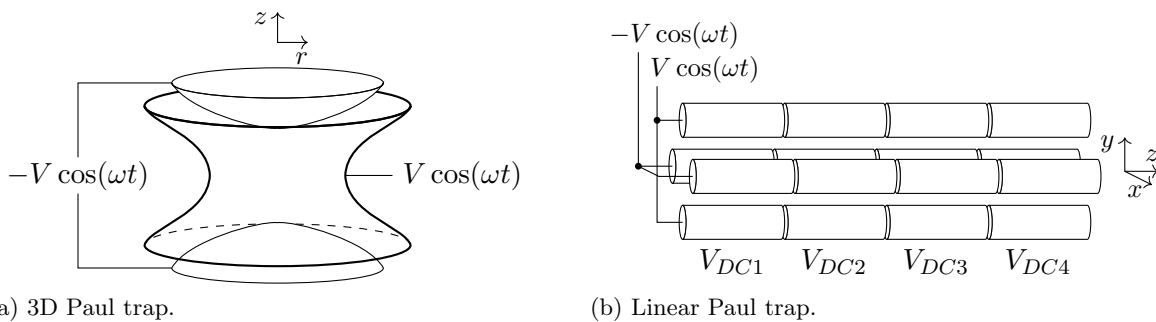


Figure 1.2: Diagrams of two Paul trap designs showing the electrode structure and an example of typical driving voltages.

### 1.3 Multi-Reflection Time-of-Flight mass spectrometer and isobar separator

Another type of ion trap which has quickly been proving its utility for RIB facilities is the MR-ToF mass spectrometer and isobar separator [19][20][21][22][23][24][25]. The core principle of a ToF mass spectrometer is that ions of different masses, moving in the same direction with the same kinetic energy may be distinguished by the time of flight over which they traverse a given distance (Figure 1.3). From the classical kinetic energy equation we may derive a mass resolving power  $R$  measuring mass  $m$  with uncertainty  $\Delta m$  based on time of flight  $t$  with an uncertainty  $\Delta t$  to be [26],

$$R = \frac{m}{\Delta m} = \frac{t}{2\Delta t}. \quad (1.3)$$

However, it may be necessary for ions to traverse hundreds of meters to resolve similar masses, requiring an impractically large amount of space. Instead, electrostatic mirrors are used to confine the path of the ions to a small space. By this method, ions of similar mass—such as isobars—may be rapidly separated based on their time of flight. If ions ejected from the MR-ToF after a desired time then hit a time-sensitive detector it is possible to measure ion masses, a method which has been shown able to achieve mass resolving powers on the order of  $10^5$  [9]. Alternatively, combining the MR-ToF with a fast deflector allows unwanted species to be deflected out of the beam once spatially separated after a sufficient time of flight. This way the MR-ToF can act as a mass filter capable even of removing isobaric contamination.

### 1.4 Beam purity

Many nuclear-physics experiments require high beam purity although most beam production techniques produce a multitude of species rather than the desired species alone. Decay products from contaminant species can hide the signal from the desired species or cause undesirable space-charge effects leading to efficiency losses. In the context of Penning trap mass spectrometry, interactions with contaminant ions can shift the measured cyclotron frequency of the desired species [13].

The most common class of beam contaminant to confound measurements at RIB facilities is isobars. Isobars are nuclides with the same total number of protons  $Z$  and neutrons  $N$ , expressed as the atomic mass number  $A = Z + N$ . Because protons and neutrons are very similar in mass, isobars will have very similar masses and become difficult to remove from

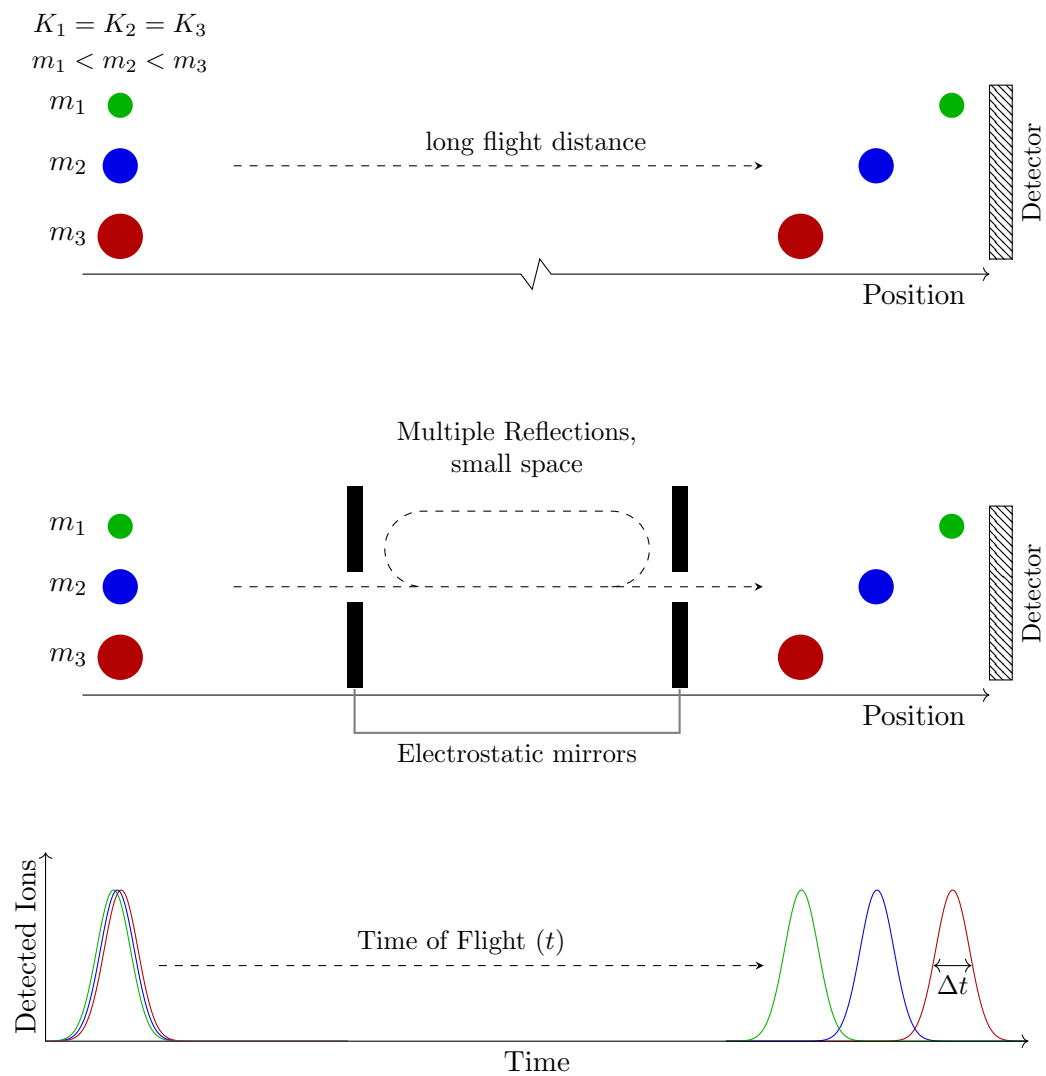


Figure 1.3: Outline of the principle of time-of-flight mass spectrometry showing three ions becoming separated over a given time of flight. Top: Flight over long distance. Middle: Flight over same distance as top, but fit into smaller physical space through multiple reflections. Bottom: Time of flight spectrum at start and finish of the above mass separations.

a RIB, thus contaminating the beam being measured. Non-isobaric contaminants are easily removed, only requiring resolving powers  $\sim 100$  which is easily provided by magnetic mass separators.

Dipole magnetic mass separators are one solution to beam purification essential in any RIB facility. These allow near instantaneous filtering of practically unlimited beam currents, removing the vast majority of contaminants produced during the initial RIB production process. In principle this method can achieve resolving powers more than sufficient to remove isobars; however, the necessary magnets are both large and expensive. For example, the high-resolution magnetic mass separator planned for the new ARIEL facility at TRIUMF is expected to be able to achieve resolving powers of  $R \approx 20\,000$  [27]. This resolving power is still insufficient to separate many isobars, such as  $^{40}\text{Ar}^+$  and  $^{40}\text{K}^+$  which have a relative mass difference of approximately 25 000.

Processes of beam purification within a Penning trap, such as dipole cleaning [14][15], have a different set of strengths and limitations. An attractive aspect of dipole cleaning is that it provides a high resolving power, up to  $\sim 10^7$  [3], sufficient even for the removal of nuclear isomers. However, dipole cleaning requires that ions be individually identified and removed, beam with a small space charge, and at least  $\approx 10$  ms.

The performance of a typical MR-ToF is situated between these two types of purification techniques. MR-ToFs have achieved  $R \approx 10^5$  in 5 ms [21] and are well suited for low-energy RIB production and experiments, such as TITAN [28] at ISAC-TRIUMF [29]. The implementation of an MR-ToF for TITAN designed and assembled by collaborators at the University of Giessen is the subject of this thesis.

## 1.5 TITAN Experiment

TRIUMF's Ion Trap for Atomic and Nuclear science (TITAN) [28][30] (Figure 1.4) is a part of the Isotope Separator and ACcelerator (ISAC) [29] experimental facility at TRIUMF. Its primary function is the study of rare-isotopes using a number of ion traps. The cornerstone of the TITAN experimental work has been Penning trap mass spectrometry. TITAN has also demonstrated the ability to perform in-trap decay spectroscopy. In the following, the ISAC facility and the individual components of TITAN will be introduced.

### 1.5.1 ISAC Facility

The ISAC facility at TRIUMF produces and delivers rare isotopes to experiments which focus on studying fundamental physics in areas such as nuclear structure and nuclear astrophysics. ISAC employs the production of RIBs through the Isotope Separation On-Line (ISOL) method. Rare isotopes are produced by impinging a 480 MeV proton beam accelerated in TRIUMF's main cyclotron [31] onto a target [32], causing a vast range of isotopes to be produced through nuclear fission, spallation, and fragmentation reactions. The resulting isotopes are ionized with an ion source so that they may be transported with electric and magnetic fields [33]. The ions are accelerated to 20–60 keV and passed through a magnetic mass separator with  $R \approx 3000$ . The isotopes of the selected mass may then be sent to various low-energy experiments—including TITAN—or may undergo acceleration to higher energies through a set of linear accelerators to meet the needs of medium- (0.15–1.8 MeV/u) to high-energy ( $\geq 6$  MeV/u) experiments.

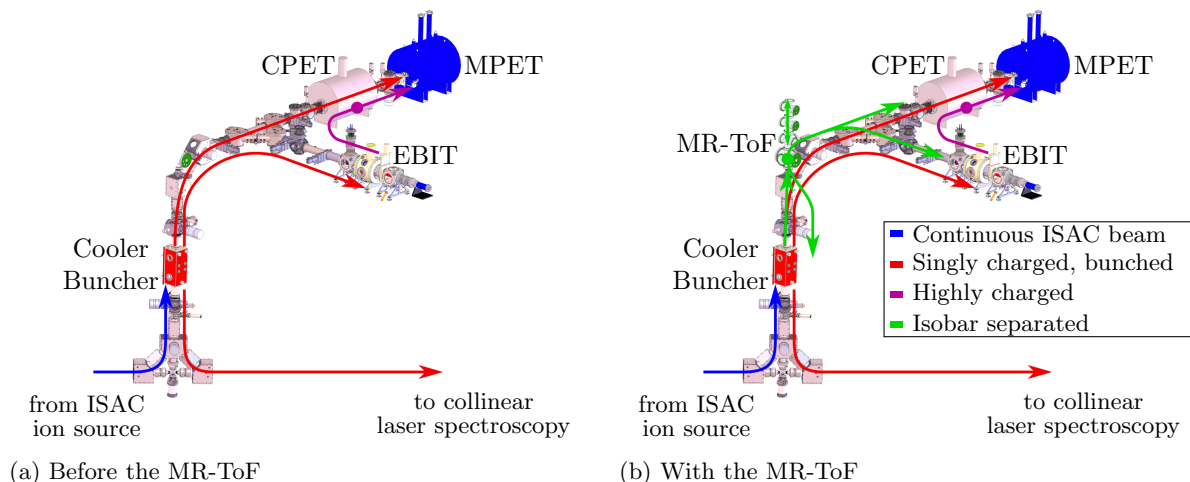


Figure 1.4: A schematic overview of the TITAN experiment a) before the MR-ToF and b) with the MR-ToF installed. Arrowed lines are used to indicate paths the ion beam may take to TITAN from the ISAC ion sources, inside TITAN, or from TITAN to the ISAC collinear laser spectroscopy experiment.

### 1.5.2 Cooler Buncher

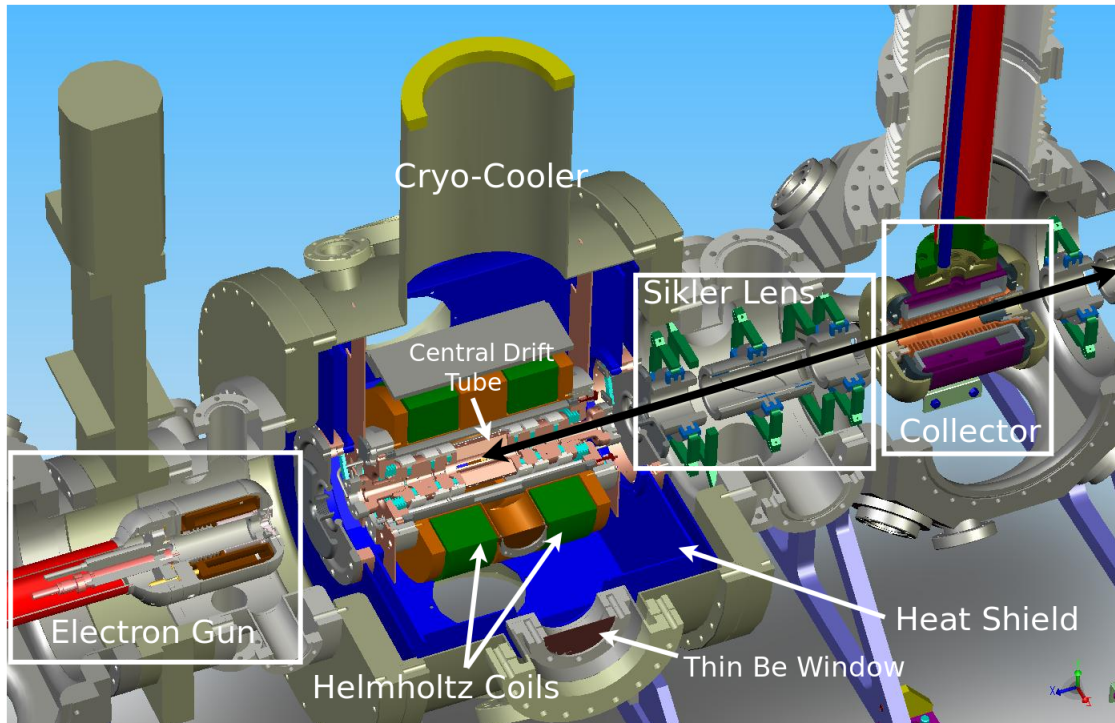
The first component of the TITAN system is a radio frequency quadrupole (RFQ) cooler buncher (CB) [34]. The CB is a linear Paul trap which converts the continuous ISAC beam to bunched beam of lower emittance. It ejects the ion bunches into the TITAN beamline, where the beam energy is lowered to around 2.4 keV using a pulsed drift tube. The low-energy, low-emittance bunched beam is transported to the various other ion traps in the TITAN system for beam preparation and measurements.

### 1.5.3 EBIT

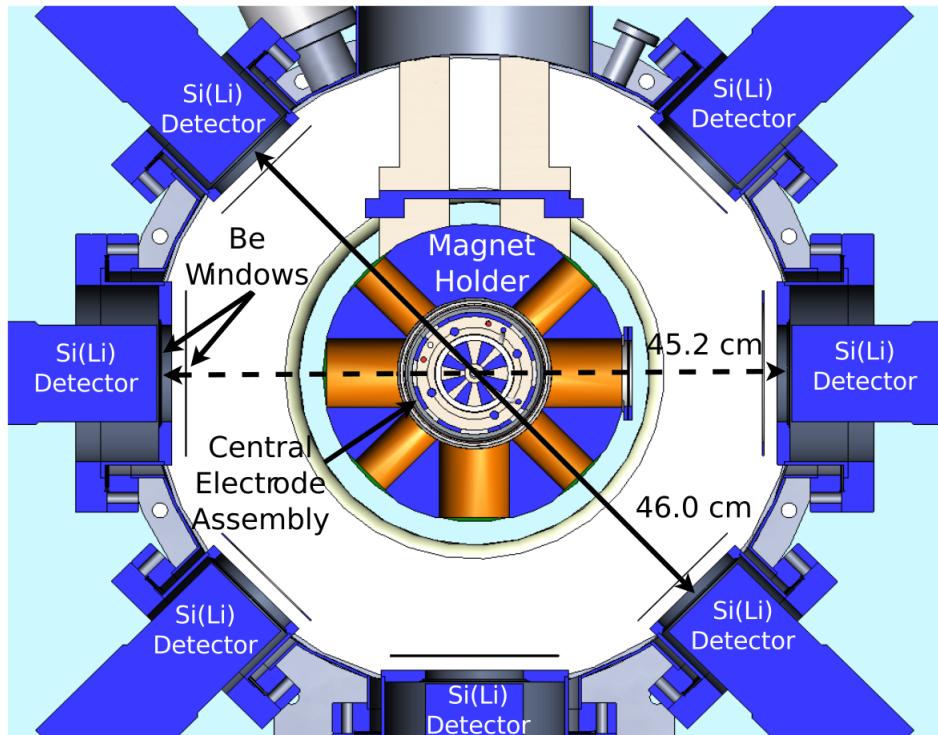
TITAN uses an electron beam ion trap (EBIT) [35] charge breeder to increase the charge state of ions undergoing Penning trap mass measurement (Figure 1.5 a). An EBIT superimposes an electron beam axially upon a Penning trap providing radial confinement. Successive electron impacts remove electrons, increasing the ion charge states. A recent high-voltage upgrade [36] to the TITAN EBIT brings the electron beam energy up to 62 keV which is expected to be able to strip ions bare for elements up to tellurium ( $Z=65$ ); as well, the electron gun has been designed to be able to reach electron beam currents up to 5 A. This EBIT is also equipped with SiLi gamma-ray detectors (Figure 1.5 b) for in-trap decay spectroscopy [37]. The decay spectroscopy benefits from the effect of positrons being guided away from the decaying ion bunch thereby suppressing background noise in gamma-ray spectra from electron-positron annihilation. An additional benefit of decay spectroscopy in the EBIT is the ability to investigate decay properties of highly charged ions [38].

### 1.5.4 Measurement Penning trap

High-precision mass measurements of rare isotopes are performed in the TITAN Measurement Penning Trap (MPET). MPET uses a 3.7 T magnetic field to provide radial confinement



(a) EBIT.



(b) SiLi gamma-ray detectors.

Figure 1.5: Diagrams of TITAN EBIT showing: a) Components of the trap along the beam axis, with the path of ions indicated by a black double arrow. b) The arrangement of SiLi gamma-ray detectors around the trapping region. Figures found in [39].

of ions within the trap and then measures ion masses through the TOF-ICR method. Precisions on the order of  $\delta m/m = 10^{-9}$  have been achieved in MPET [40]. MPET has also been able to achieve very rapid mass measurements of short-lived nuclides having successfully performed a mass measurement of  $^{11}\text{Li}$ , with a half-life of 8.8 ms [41].

### 1.5.5 TITAN MR-ToF

The most recent addition to the TITAN system has been an MR-ToF mass spectrometer and isobar separator (Figure 1.6). As outlined in Section 1.3, an MR-ToF provides an intermediate speed and resolving power for the removal of contaminants from a beam while also providing a broad-band mass spectrometer. The TITAN MR-ToF was designed to be able to perform mass measurement with a resolving power of 100 000 and also to be able to remove isobaric contaminants with a resolving power of 20 000 within 10 ms, using the mass-selective re-trapping method [42].

## 1.6 Outline of this thesis

The focus of this thesis work has been the integration of the TITAN MR-ToF into the TITAN beamline, showing that it performs mass measurement and isobar separations as designed and that it can be bypassed without impacting performance of the established TITAN system. Previous work with the TITAN MR-ToF includes its construction which is discussed in Reference [43] and offline commissioning, outlined in Reference [44].

In this thesis we shall first discuss some of the core principles of ion optics and the ion optical devices used in the transport and confinement of charged-particle beams.

These ion optical principles will then be applied to an investigation of the TITAN beamline and the performance of the beam within. To maximize beam transport efficiency into the MR-ToF, new optics were added into the existing TITAN beamline. With the introduction of the new ion optics, simulations were performed to examine how the optics transport ions into the MR-ToF or bypass it. Simulations were performed of the TITAN beamline from the TITAN CB to MPET, from the CB to the MR-ToF, and from the MR-ToF to the CB to provide insights into the TITAN beam properties where diagnostic components are not available and to predict operating parameters.

Once the MR-ToF was installed in the TITAN beamline, a commissioning experiment was performed showing the capability of the MR-ToF to perform mass measurements and isobar separation as part of the TITAN facility. Studies of ion transport efficiency into the MR-ToF were also performed.

We end by discussing an outlook for how the TITAN MR-ToF may be used to expand the scientific program being pursued with TITAN.

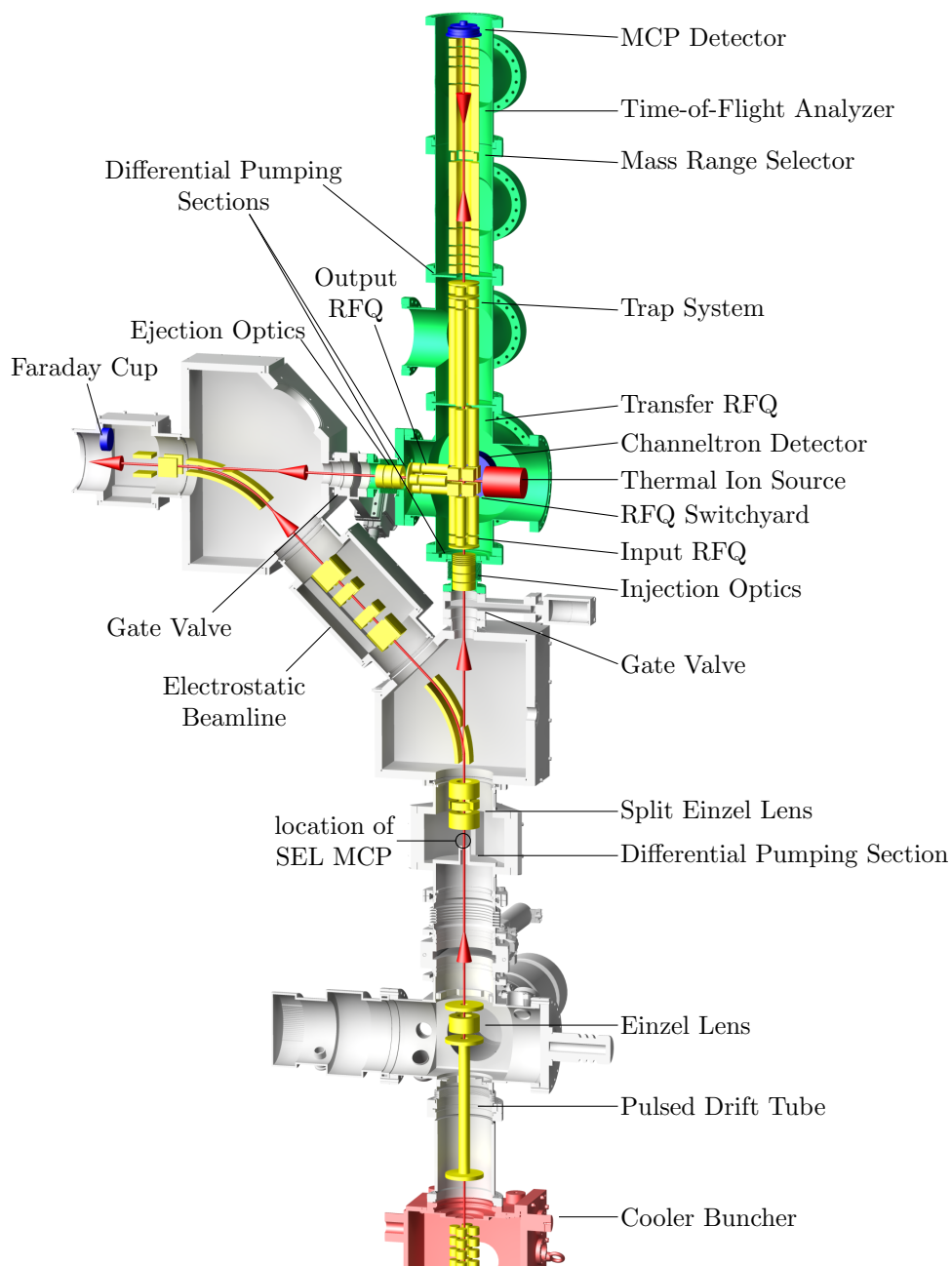


Figure 1.6: Schematic of the MR-ToF and its interface with the TITAN beamline. Ion optical electrodes are indicated in yellow; the MR-ToF vacuum chamber is highlighted in green; detectors are shown in blue; red arrowed lines are used to indicate possible beam paths through the TITAN beamline and MR-ToF.

## Chapter 2

# Principles of ion transport needed for MR-ToF integration

The TITAN experiment seeks to provide valuable insights into nuclear astrophysical processes and nuclear structure by means of precise mass measurements of rare isotopes using Penning trap mass spectrometry. The presence of contaminant ions in a Penning trap mass measurement can cause shifts in the measured cyclotron frequency of the ion of interest, impeding both the accuracy and precision of the measurement. This reduced quality of mass measurement motivates the need for a pure ion beam entering the trap. The most common contaminants entering the trap are isobars. In order to remove these isobaric contaminants from the beam quickly ( $< 10$  ms) and without prior knowledge of the specific contaminants a Multi-Reflection Time-of-Flight (MR-ToF) mass spectrometer and isobar separator was designed, built, commissioned, and installed in the TITAN beamline.

An essential part of integrating the MR-ToF into TITAN was ensuring fast and efficient transport of beam into the MR-ToF. The purified beam needs to be transferred to the Measurement Penning Trap (MPET). To accomplish this beam transport it was important to have an understanding of the principles of charged particle transportation.

### 2.1 Understanding beam dynamics using emittance

A key tool used in the study of charged particle optics is the concept of emittance. Emittance provides a means of quantifying beam quality which—for example—sets constraints on the ability to deliver the beam within given parameters. The definition of emittance is directly related to the 6-dimensional phase space volume occupied by a set of particles.

According to Liouville's theorem this phase space volume is invariant under the conservative forces which can be defined by a Hamiltonian [45]. Because of this invariance, by measuring the phase space volume in one location, it is known in all other locations the volume may occupy at different times. To introduce the concept of emittance we look at the 2-dimensional phase space planes of the total phase space volume. One definition of emittance ( $\epsilon$ ) is the phase space area occupied by the particle distribution, expressed in the x-axis case for positions  $x$  and momenta  $p_x$  as,

$$\epsilon_x = \iint dx dp_x. \quad (2.1)$$

This quantity is invariant for constant beam energy, similar to the invariance of the total phase space volume. The beam energy dependence however behaves in a predictable fashion and in the non-relativistic approximation the emittance at a particular energy  $E$  may be compared to some reference emittance  $\epsilon_{ref}$  at energy  $E_{ref}$  by the relation,

$$\epsilon = \sqrt{\frac{E_{ref}}{E}} \epsilon_{ref}. \quad (2.2)$$

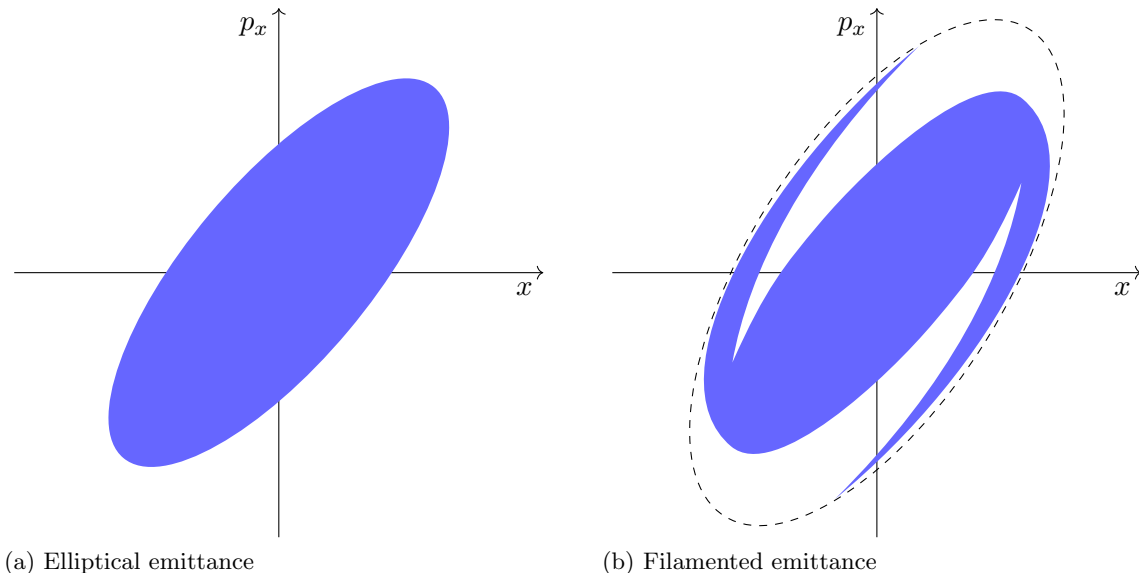


Figure 2.1: Example of a) an elliptical emittance and b) a filamented emittance.

An alternative definition of emittance is known as the root mean square (rms) emittance,

$$\epsilon_{rms} = \sqrt{\langle xx \rangle \langle p_x p_x \rangle - \langle x p_x \rangle^2}. \quad (2.3)$$

Here we use angle brackets to denote mean values of contained variables. This is a statistical description which is very useful for describing beams which lack clearly defined boundaries, such as gaussian or similar distributions typical of experimental measurements.  $\epsilon_{rms}$  is not an invariant quantity, it will grow if the area of the emittance becomes distorted. It is common for the emittance to be elliptically distributed (Figure 2.1 a), but the beam evolution may undergo non-uniform shifts in the emittance distribution. Such a beam evolution can lead to arm-like patterns in the emittance distribution referred to as filaments. An example of a filamented emittance is shown in Figure 2.1 b where the filaments diverge from an otherwise elliptical distribution. The examples in Figure 2.1 both fill the same phase space area; however in the filamented case the rms emittance will be larger. Emittance filamentation also creates challenges for beam matching which may require complex ion optical lens arrangements or larger acceptance (as indicated with the dashed line). Another difference with  $\epsilon_{rms}$  is that it typically gives a smaller value than the emittance defined as the phase space area. In the case of a uniform elliptical distribution,  $\epsilon_{rms} = \frac{\epsilon}{4\pi}$  [46].

The rms emittance provides a basis for further description of the emittance distribution through what are known as Twiss parameters. These parameters are used to describe an emittance ellipse and may be used to calculate how it evolves through various ion optics. The Twiss parameters are defined as,

$$\beta = \frac{\langle xx \rangle}{\epsilon_{rms}} \quad (2.4a)$$

$$\gamma = \frac{\langle p_x p_x \rangle}{\epsilon_{rms}} \quad (2.4b)$$

$$\alpha = -\frac{\langle x p_x \rangle}{\epsilon_{rms}}. \quad (2.4c)$$

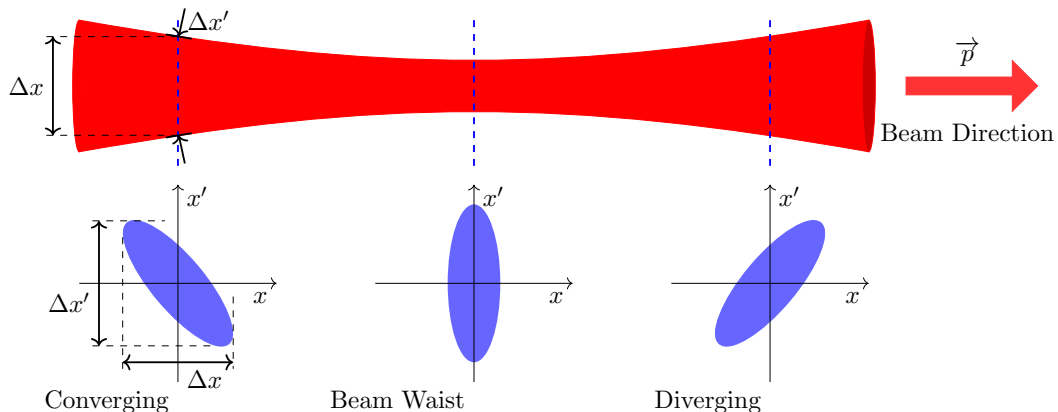


Figure 2.2: Top: Visualisation of transverse emittance at different positions of a beam, for where the beam is converging, at a focus point (beam waist), and when it is diverging. Bottom: Example plots of the transverse emittance for the positions indicated by the blue dashed line over each plot. The left plot includes a direct illustration of the relation between the spatial distribution  $\Delta x$  and beam divergence  $\Delta x'$  to the trace-space plot. As shown, the orientation of the ellipse changes and in real scenarios it may change shape, but the total area is invariant for constant beam energy in a vacuum.

From this we may calculate an ellipse as,

$$\gamma x^2 + 2\alpha x p_x + \beta p_x^2 = \epsilon_{rms}. \quad (2.5)$$

### 2.1.1 Transverse emittance

The convention used in this thesis is to define the  $z$ -direction to be the average direction of beam propagation and to refer to the associated emittance as the longitudinal emittance; emittance in the transverse directions  $x$  and  $y$  are then known as the transverse emittances. Experimentally it is more practical for measuring and computing transverse emittance to describe the transverse momentum  $p_x$  with its derivative in the longitudinal direction  $x' = \frac{dp_x}{d|\vec{p}|}$ . If  $p_z \gg p_x$  we may use the small angle approximation to relate  $x'$  to the ion trajectory's angle away from the beam axis—its divergence—by  $x' = \tan(\theta) \approx \theta$ , measured in radians. This  $x$ - $x'$  description of the phase space is often referred to as the trace space [46]. An example of the spatial evolution and the corresponding trace space evolution of a beam can be seen in Figure 2.2.

For the scales typical of ion optics it is convenient to express measurements of  $x$  in mm and  $x'$  in mrad. Using these units, emittance may be expressed in units of mm mrad; since radians are not formally an SI unit this may be expressed more concisely as  $\mu\text{m}$ . Some communities prefer to divide the trace-space area by  $\pi$  and express the emittance in units of  $\pi$  mm mrad. In the case of an elliptical trace space distribution removing the factor of  $\pi$  makes the emittance simply the product of the semimajor and semiminor axes, it also creates a more natural link to  $\epsilon_{rms}$ . For this thesis the division by  $\pi$  is eschewed in favour of expressing transverse emittances in units of  $\mu\text{m}$ .

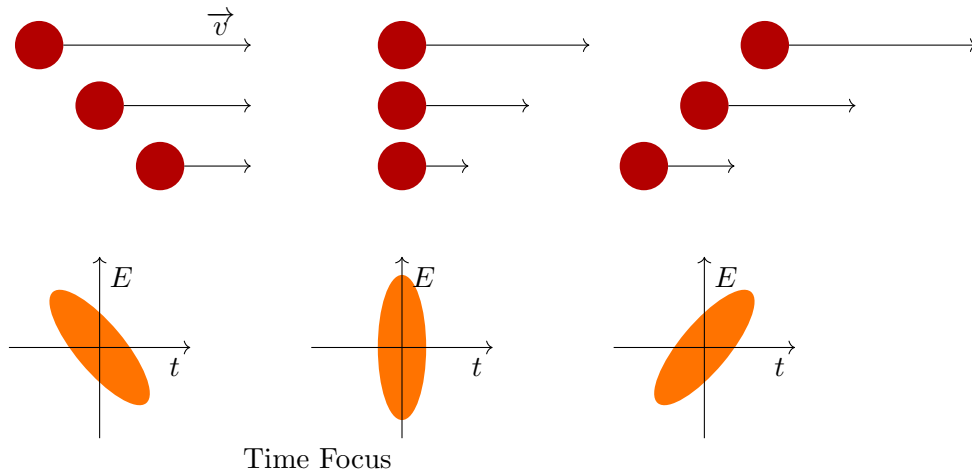


Figure 2.3: An example of a time focus for a distribution of particles. Top: Illustrated here are a set of particles moving with different velocities represented by right pointing arrows. Represented are three moments in time as the faster particles start behind the slower particles then move to overtake the slower particles. The moment where the faster particles are passing the slower is known as the time focus. Bottom: For each moment in time, an example of a corresponding longitudinal emittance plot is shown.

### 2.1.2 Longitudinal emittance

To discuss longitudinal emittance we must first note that this concept is only useful in the case of bunched beam; such beams consist of packets of ions with a finite longitudinal position and momentum spread, able to be described with emittance. Similar to the approximation of the transverse momentum  $p_x$  by the divergence  $x'$ , if the longitudinal momentum spread is small compared to the beam central momentum we may represent the longitudinal emittance by its spread in energy  $E$  and time  $t$ . As with  $x'$ , expressing longitudinal emittance in terms of energy and time has the added benefit of being more practical to measure experimentally.

An application of longitudinal emittance is the concept of a time focus. The time focus is the longitudinal analogy to the beam waist seen in Figure 2.2. Let us imagine a set of ions are distributed longitudinally as in the left-hand side of Figure 2.3. In the figure we start with the higher energy ions located behind lower energy ions in the direction of propagation. As the faster ions overtake the slower ions there is a moment where the time distribution is at its narrowest, this moment is the time focus. In time-of-flight mass spectrometry the time focus is extremely important as performing measurements away from this focus will unnecessarily increase the time width and reduce resolving power.

### 2.1.3 Acceptance

Having quantified the quality of a beam using emittance, a key application is to match the beam emittance to the so-called *acceptance* ( $\alpha$ ) of a given device. Acceptance corresponds to the maximum emittance which can be transported into the device without losses for which it is defined ( $\alpha = \epsilon_{maximum}$ ). In matching emittance to acceptance it is important that  $\epsilon_{maximum} \leq \alpha$  and that the phase space volume described by the emittance be contained within that of the acceptance.

If the phase space orientation of the beam emittance does not match that of the device

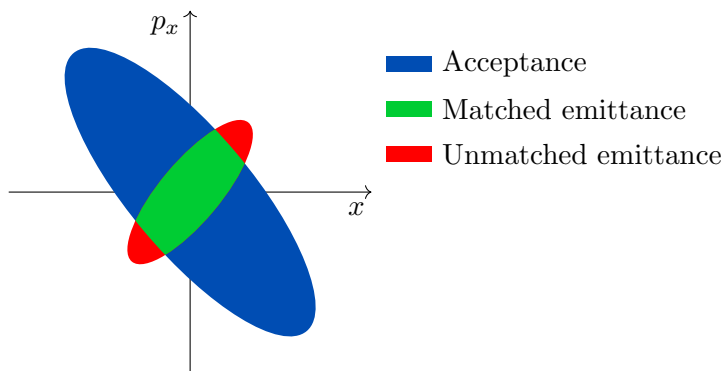


Figure 2.4: An example phase space plot where device acceptance is greater than beam emittance but their orientations cause them not to match. The unmatched portion of the beam will be lost, resulting in a lower beam transport efficiency. Such a mismatch may be eliminated through the use of ion optical lenses to re-orient the beam emittance into alignment with the acceptance.

acceptance as is, there exist a number of ion optical elements which may be used to match the two. If  $\epsilon \leq \alpha$  but the beam emittance shape and/or orientation do not match as in Figure 2.4, then lenses such as electrostatic lenses may be used to match the beam (Section 2.2.1). In cases where  $\epsilon > \alpha$  the emittance may be reduced without increasing the beam energy by using buffer gas cooling in a Paul trap (Section 2.3.2).

## 2.2 Ion optics

Ion optics are an essential part of any rare-isotope-beam (RIB) facility as they allow the RIB to be transported quickly and efficiently, while having appropriate emittance for matching the beam to the acceptance of various experiments. Ion optics also play a crucial role in the design and operation of ion traps. This control of RIBs is accomplished through the careful shaping of electric and magnetic fields.

An important consideration in the design of ion optical systems is the creation of aberrations in the beam properties. These aberrations refer to deviations in ion motion from an ideal ion path with no beam width. We describe these ion motions by their position and momentum, and deviations in flight time, kinetic energy, and mass-to-charge ratio. When applying Taylor series expansions to these descriptions the first order terms are known as the paraxial (linear) coefficients which form the basis of a linear approximation. Higher order terms are referred to as aberration coefficients and describe the non-linear evolution of a beam passing through given optics. For this thesis we will limit ourselves to referring to the order on which beam aberrations occur for a sense of scale, however a deeper discussion of this formalism and other ion optical topics may be found in References [46], [47] and [48].

The focus of this thesis has been on ion transport within a low energy beam transport (LEBT) beamline ( $E \leq 60$  keV) and ion confinement within a Paul trap or MR-ToF. This requires an understanding of electrostatic and radio frequency (RF) ion optics.

### 2.2.1 Electrostatic

Electric fields are an attractive option for ion optics due to their high field energy density which allows them to be produced with compact devices. Static electric fields are limited however by discharges which begin happening for fields around 10–20 kV/mm in high vacuum ( $P < 10^{-3}$  mbar). The precise field strength at which breakdown occurs is substantially influenced by the material and structure of the surfaces between which the discharges would occur [49]. This limitation makes purely electrostatic ion optics for beam transport only appropriate for LEBT; magnetic optics become essential for higher energy beams. When electrostatic optics are a viable option, their design benefits from their independence from mass-to-charge ratios, allowing the same optics and settings to be used for a wide range of ion masses.

The types of electrostatic ion optics most important for this thesis are Einzel lenses and quadrupole lenses for focusing beams and matching emittance, and parallel plate benders to redirect ion paths. Another type of electrostatic ion optic—the electrostatic mirror—will be discussed in the context of MR-ToF optics.

#### Einzel lens

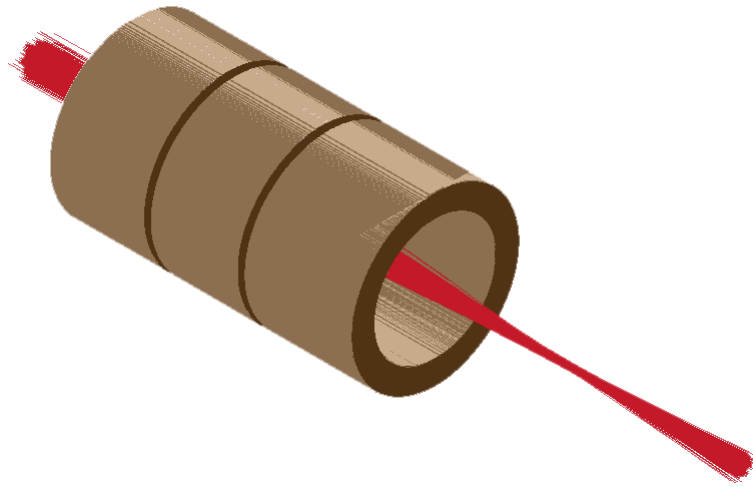
An Einzel lens (from the German *Einzellinse* for single lens) consists of three hollow cylindrical electrodes with the outer two electrodes typically at an electric potential of zero and the centre electrode having some non-zero potential ( $V_{lens}$ ) (Figure 2.5 a). So long as  $V_{lens}$  is not high enough to prevent passage of ions, the resulting electric field will have an overall focusing effect on the beam. The radial component of the electric field becomes stronger further from the beam axis causing ions at various radial positions to converge to a focus point, the position of which is determined by  $V_{lens}$ . There are two basic modes in which an Einzel lens may be operated: decelerating, where  $V_{lens} > 0$  (Figure 2.5 b), and accelerating, where  $V_{lens} < 0$  (Figure 2.5 c)). Due to restrictions incurred by Laplace’s equation, the electric fields cannot be shaped in an arbitrary fashion, this leads to aberrations in the beam properties. Third order angular aberrations (specifically referred to as spherical aberrations); as well as second order aberrations in the correlation between ion flight time and position, and ion divergence and energy. These effects will normally be larger with decelerating lenses as the ions will tend to diverge more from the beam axis before being focused [48].

For TITAN, Einzel lenses are spread along the beamline to maintain beam confinement through long straight sections. They are also used to focus the beam on narrow differential pumping apertures which separate beamline sections with different gas pressures.

#### Parallel plate deflector

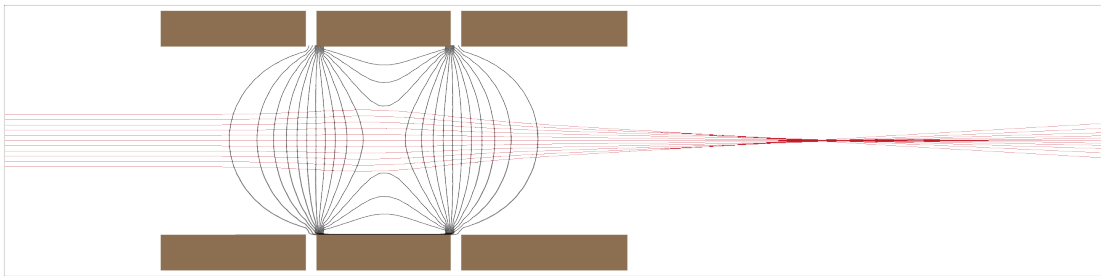
A simple but important type of ion optic is the parallel plate deflector; the plates of the deflector are given different potentials which ideally produces a constant electric field between the two. The most basic parallel plate deflector consists of two straight rectangular plates (Figure 2.6 a). Such an arrangement is commonly used for applying small corrections ( $\leq 9^\circ$ ) to beam trajectories to ensure a straight beam path. Rectangular parallel plates have the capacity to apply much larger angular shifts in the beam path, but this does not maintain the beam focus which would be desirable where a well defined beam emittance is important.

For a beam being bent in the  $y$ -direction we can maintain a well defined beam emittance first by curving the bender electrodes in the  $y$ -direction as in Figure 2.6 b. Such a bender design is known as a cylindrical bender. The variation in the radial electric field strength suggested by the field lines in Figure 2.6 b has a focusing effect on the beam in the  $y$ -direction. The



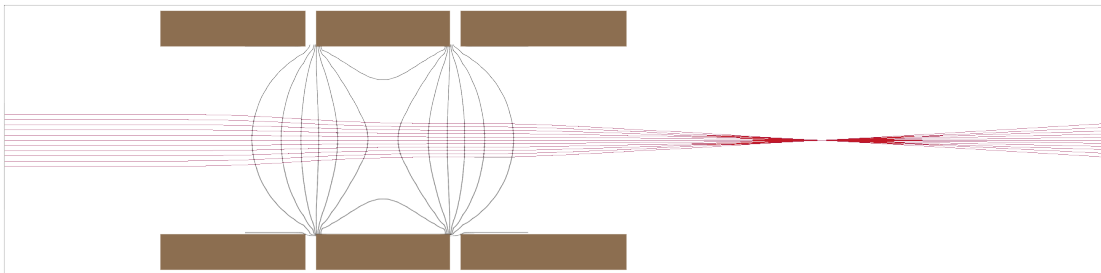
(a) Isometric image of Einzel lens with focused beam.

$$V = 0 \quad V_{Lens} > 0 \quad V = 0$$



(b) Decelerating Einzel lens.

$$V = 0 \quad V_{Lens} < 0 \quad V = 0$$



(c) Accelerating Einzel lens.

Figure 2.5: Simulations of ion trajectories (red lines) and ion optical elements (brown) for an Einzel lens showing a) an isometric view of the lens and the ion trajectories. b) and c) show the Einzel lens operating with a decelerating and accelerating potential respectively, along with contour lines of the electric potential (black curves). The example here shows a parallel beam being focused to a point, the position of which is determined by the potential  $V_{Lens}$ . Ion trajectories portrayed here are from ions flying from left to right. Simulations produced in SIMION [50].

associated radial dependence of the electric potential is described as,

$$V(r) = \frac{1}{\ln(r_2/r_1)} [(V_2 - V_1) \ln r (V_1 \ln r_2 - V_2 \ln r_1)], \quad (2.6)$$

in which  $r_1$  and  $r_2$  are the radii of the inner and outer plates with  $V_1$  and  $V_2$  being the corresponding potentials. The effect of this radial dependence of the potential is that faster moving ions will travel through the bender at a larger radius and experience a slight retarding field relative to a beam axis at  $r_0 = (r_2 - r_1)/2$ . Slower moving ions will have a smaller bend radius, causing them to experience an accelerating potential towards  $r_0$ . Together these have the effect of focusing the beam towards the beam axis along  $r_0$ . However, in the  $x$ -direction there is no focusing effect, so the beam behaves as though it were in a field-free region in the  $x$ -direction.

To provide equal focusing in the  $x$ - and  $y$ -directions through a bend the cylindrical bender design may be modified to have an electrode curvature of equal radius in the  $x$ - and  $y$ -directions. Such a design is known as a spherical bender, a diagram of which is shown in Figure 2.6 c. Spherical benders are used as a standard optic in the TRIUMF ISAC Low Energy Beam Transport (LEBT) area [51] and are also used in the TITAN beamline. Two designs of spherical bender are used: a  $45^\circ$  bender which bends beam from one direction; and a  $36^\circ$  bender which can bend beam from two perpendicular directions and allow transport straight through from a third direction. The  $36^\circ$  bender is coupled with a rectangular parallel plate which bends the beam by an additional  $9^\circ$ , in total bending the beam by  $45^\circ$ .

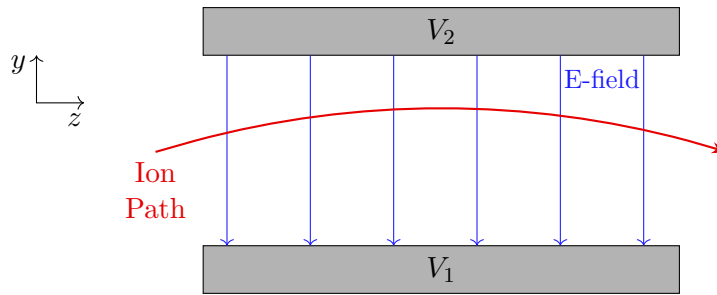
These parallel plate designs all seek to produce electric fields perpendicular to the ion path to redirect the ions without changing the average beam energy. However, there are cases where it is useful to redirect an ion beam with electric fields near antiparallel to the beam path using electrostatic mirrors.

### Electrostatic Mirrors and MR-ToFs

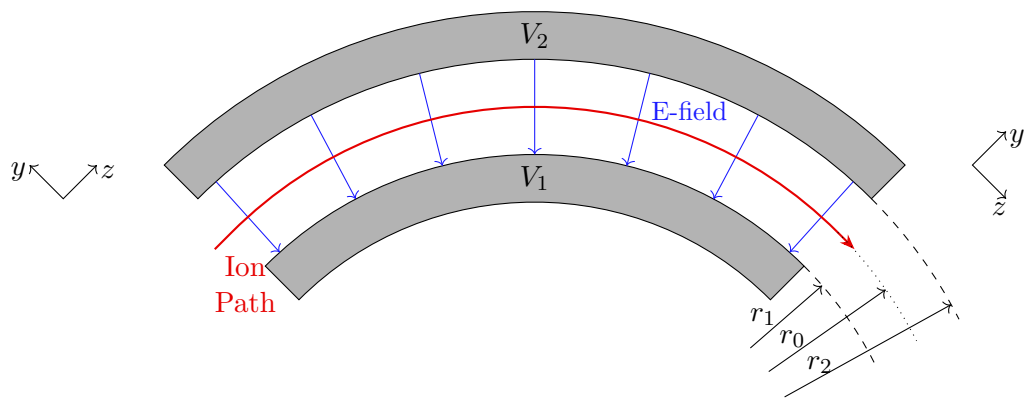
The invention of the electrostatic mirror was a key advance in the development of time-of-flight mass spectrometry. Prior to their invention, time-of-flight mass spectrometry could only provide resolving powers of several hundred [52]. In contrast, modern time-of-flight based mass spectrometers are able to achieve resolving powers three orders of magnitude greater [9].

An electrostatic mirror requires a region with a higher potential than the beam energy which reflects the beam path. The electric field is primarily perpendicular to the initial motion of the ions, causing them to slow and reverse direction at some turning point. The depth to which ions reach in the mirror field is energy dependent such that higher energy ions will penetrate deeper into the field and thus take longer to be reflected than lower energy ions. In the case of bunched beams, the net effect is to shift the time focus of a reflected beam (Figure 2.7). The electric field strength may then be modified to change the location of the time focus in order to set it on a time-sensitive detector or another desired location.

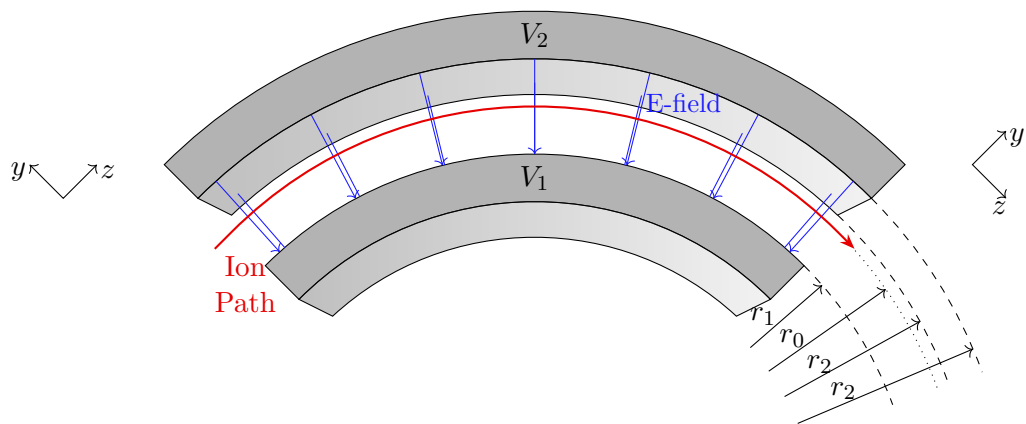
Early versions of electrostatic mirrors used parallel plate grid electrodes to produce constant electric fields for reflecting ions [52]. Such grids would cause ions to be lost through collisions with the grid, reducing the efficiency of transmission through the mirror. Figure 2.8 shows an example of an electrostatic mirror using a grid electrode and the resulting ion losses at the grid. If ions are to undergo multiple reflections on an electrostatic mirror—as is the case in an MR-ToF—the ion losses to grid electrodes would become very large. Such ion losses would be unacceptably large in the context of RIB experiments where efficiency is very important, thus a gridless mirror needed to be developed. The design of a gridless mirror has the beam path surrounded by one or more electrodes, such as a series of hollow cylindrical electrodes;



(a) Rectangular parallel plate bender.



(b) 90° cylindrical bender.



(c) 90° spherical bender cross-section.

Figure 2.6: Examples of parallel plate bender designs. a) A simple rectangular plate design, used in TITAN for small beam path corrections, up to 9°. b) A 90° cylindrical bender, and c) a 90° spherical bender. The direction of the electric field between the bender plates is indicated by the blue arrows.

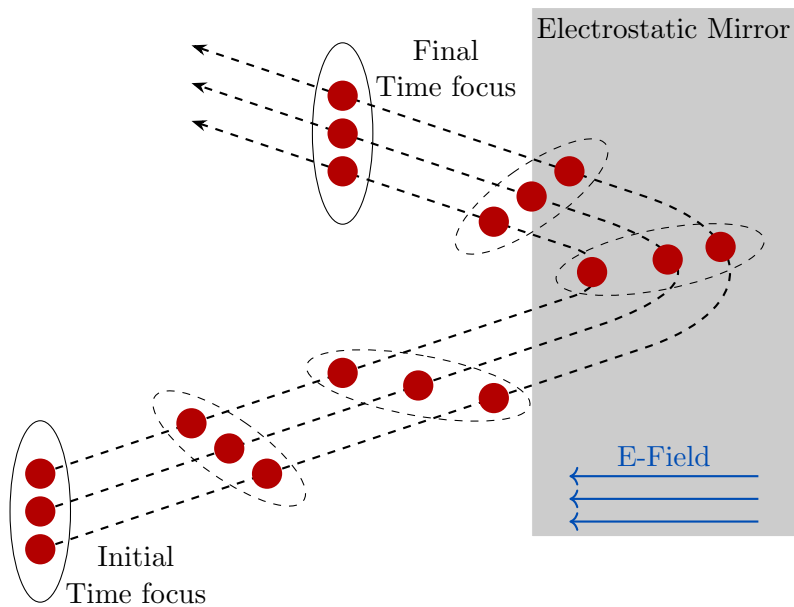


Figure 2.7: An illustration of how the time focus is shifted by an electrostatic mirror. Dashed lines indicate the trajectories followed by individual ions. Ellipses are drawn around the ions to indicate snapshots in time, showing the process of the time shift. The direction of the electric field is indicated with the blue lines, though this field would be present through the mirror.

however, these introduce problematic field inhomogeneities [48]. These inhomogeneities were first overcome in a rotationally symmetric mirror by having an additional cylindrical electrode with an accelerating potential before the reflecting portion of the mirror, effectively acting as an Einzel lens [53].

The decelerating portion of a gridless electrostatic mirror will typically be made of multiple electrodes in order to remove time-of-flight aberrations. These aberrations need to be reduced because they diminish the precision and resolving power of a time-of-flight mass measurement. Increasing the number of electrodes used increases the degrees of freedom for the removal of aberrations, meaning that higher order aberrations can be removed by increasing the number of electrodes. The TITAN MR-ToF uses three mirror electrodes on either end (Figure 2.9) to provide third-order time-of-flight focusing. The gains in mass resolution from adding mirror electrodes are tempered by voltage instabilities in the power supplies (currently  $\sim 10$  mV) which set the potential on each electrode. Such instabilities are a major limiting factor in the resolution achievable in contemporary MR-ToFs [54].

In the TITAN MR-ToF the mirrors are tuned to provide a time focus in the centre of the analyzer during the multiple-reflection phase of its operation (Figure 2.10). Ions entering the analyzer do not initially have this desired time focus, so they must undergo a time focus shift (TFS) in their first reflection. After the TFS the mirrors are set to maintain a constant time focus until it is time for the ions to be ejected. Ejected ions undergo a second TFS to give a time focus on the detector. This focusing scheme allows the number of “turns” (ions reflecting off both mirrors and returning to an arbitrary start point) to be changed without additional tuning of electrode potentials. Further discussion of this concept may be found in Reference [55].

One challenge which arises in MR-ToF mass spectrometry is that as ions undergo many turns the lighter ions will experience more turns than heavier ions. This difference in turn numbers at

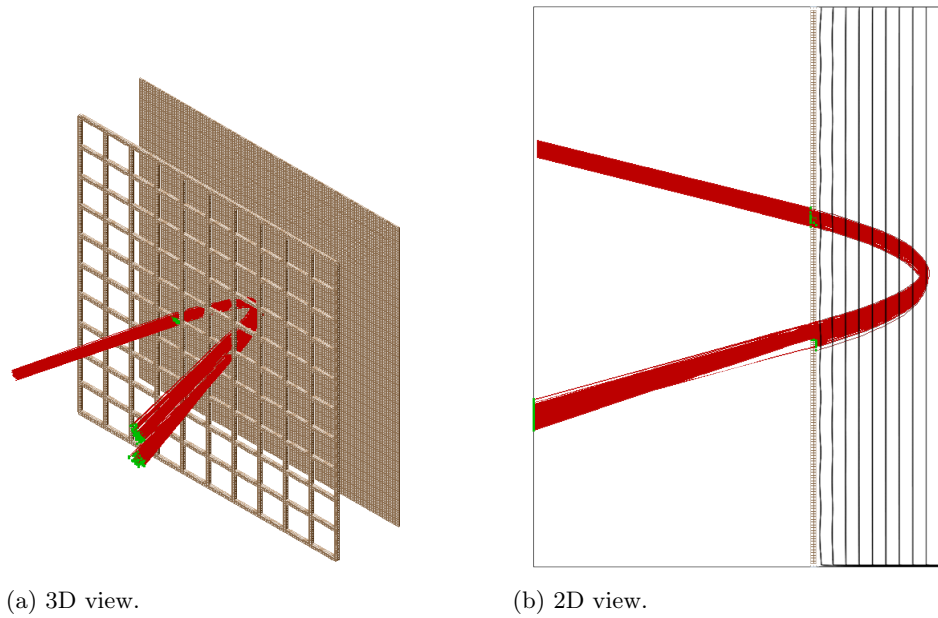


Figure 2.8: Simulation of an electrostatic mirror using a grid electrode. Ion trajectories (red) start on a) the left, b) the top. Ion collisions with the grid electrode (brown) or the boundary of the simulation area are marked in green. Electric potential contour lines are shown in black in b). Simulation produced in SIMION [50].

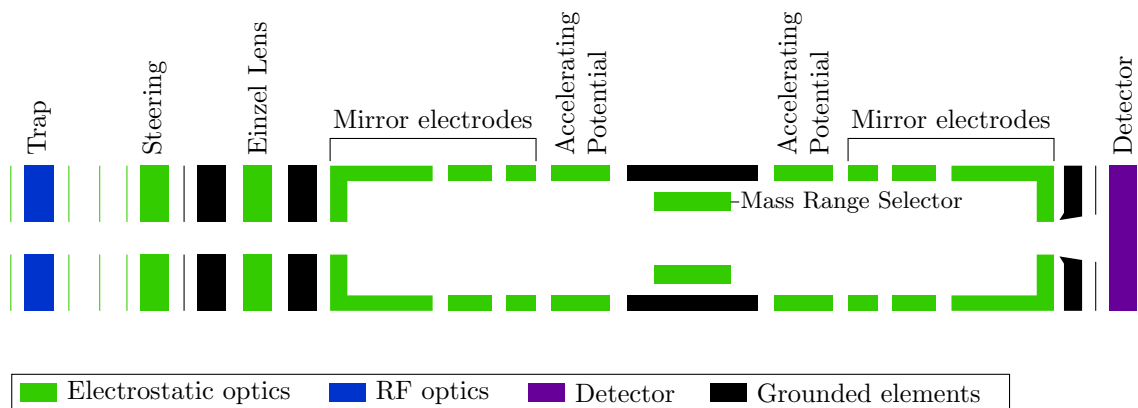


Figure 2.9: Schematic of the TITAN MR-ToF ion optics.

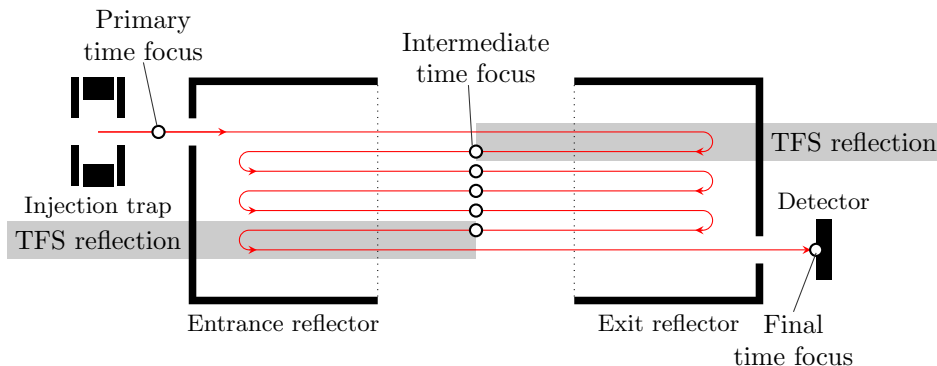


Figure 2.10: An illustration of the time focus shift (TFS) in the TITAN MR-ToF from injection into the MR-ToF to setting a final time focus on a detector.

best causes the time-of-flight mass spectrum to be more difficult to read and analyze; at worst it causes interference between a signal of interest and that of a contaminant. The solution for this problem used in the TITAN MR-ToF is a Mass Range Selector (MRS). The MRS is a set of electrodes in the centre of the MR-ToF analyzer (Figure 2.9) which can be given a dipole potential to deflect unwanted ions out of the beam. The MRS is pulsed on and off so that only a limited mass range is measured at the detector [56].

### Quadrupole lenses

An additional type of ion optical lens uses a transverse quadrupolar field to focus the beam. This field is typically produced by a quadrupolar arrangement of cylindrical electrodes as in Figure 2.11. This radial potential variation contrasts with the mostly longitudinal potential change of an Einzel lens. For the Einzel lens most of the potential gradient is longitudinal, yet it is the small radial component which provides the focusing effect. The result is that a quadrupole lens may achieve similar focusing power with a much lower electric potential on its electrodes. Quadrupole lenses also benefit from allowing separate control of the beam properties in the two transverse directions. However quadrupole lenses require a higher degree of complexity for their design and operation due to the larger number of electrodes and related power supplies.

First we must consider that a single electrostatic quadrupole lens can only focus in one transverse direction and necessarily defocuses the beam in the other. For this thesis we will refer to electrostatic quadrupole lenses focusing in the  $x$ -direction as focusing lenses (F) and those focusing in the  $y$ -direction as de-focusing (D). In order for quadrupole lenses to focus in both transverse directions, sets of individual lenses must be arranged into quadrupole multiplets. Two lenses are the minimum needed for focusing in both transverse directions [47], but larger numbers of quadrupoles can be used to provide greater control of the beam focus as well as for reducing aberrations in the beam. A minimum number of four quadrupole lenses would be needed to mimic the action of an Einzel lens to first order by arranging their focusing action in an axial symmetric fashion, such as DFFD [48]. Such an arrangement is referred to as a quadrupole quadruplet, a simulated example of which may be seen in Figure 2.12.

In the TITAN beamline DFFD quadrupole multiplets are used in  $90^\circ$  bend sections to provide focusing between  $45^\circ$  bends from spherical and rectangular benders. This provides the beam confinement in both transverse direction similar to an Einzel lens while providing the

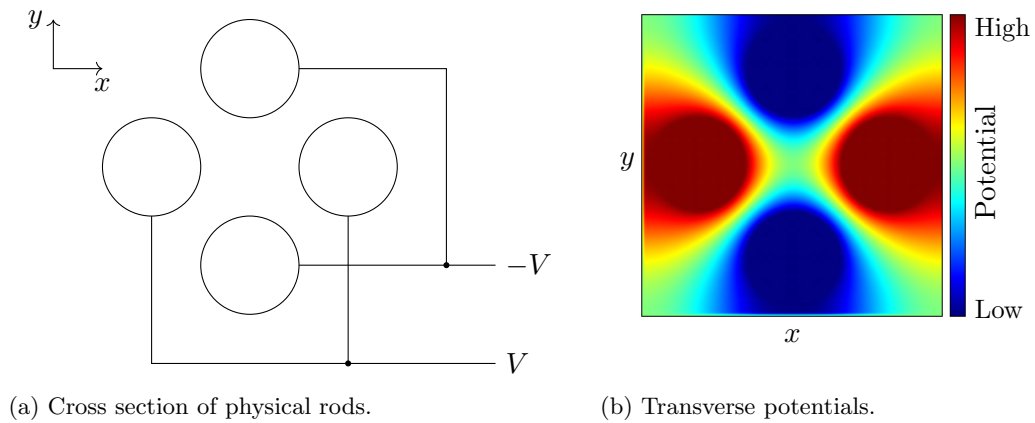


Figure 2.11: Cross-sectional diagram of a typical quadrupole lens with a potential focusing in the  $x$ -direction. a) The arrangement of physical rods with the applied electric potentials. b) A simulation of the resulting electric potential distribution produced in SIMION [50].

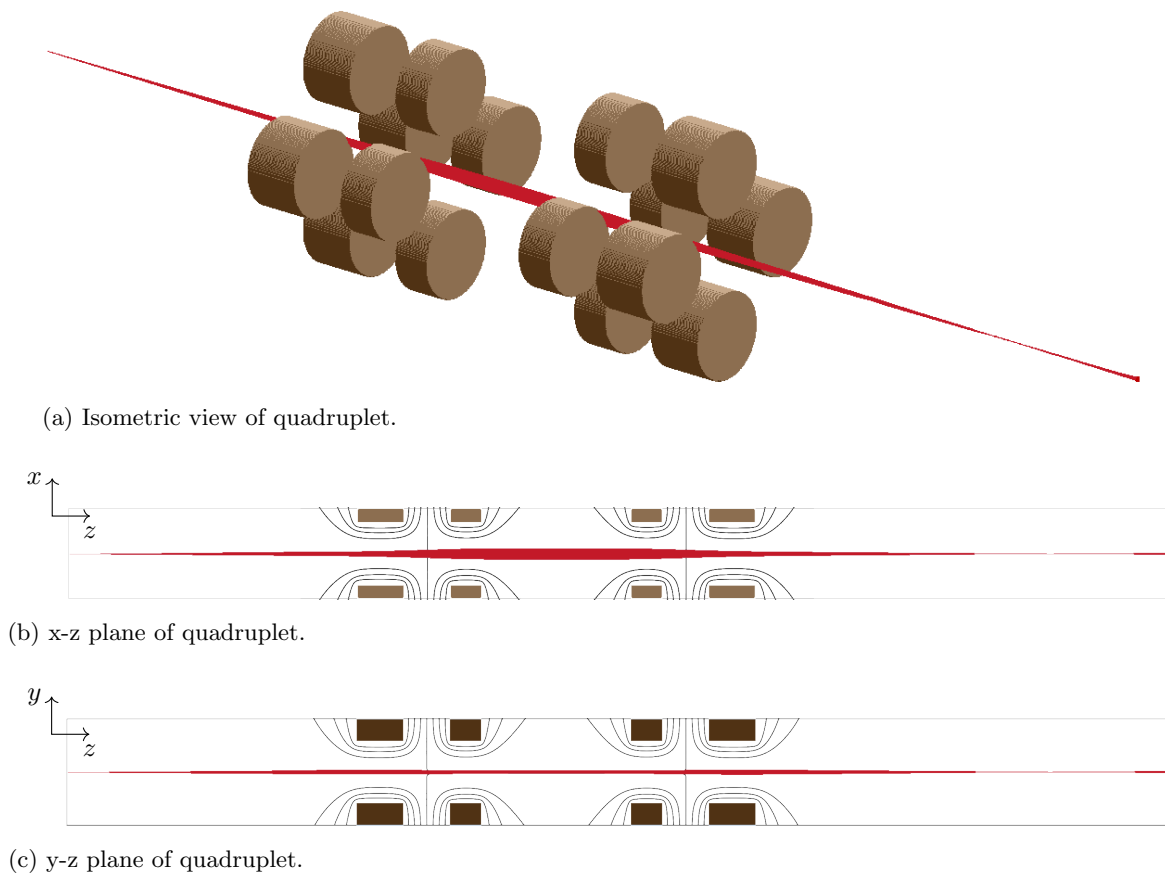


Figure 2.12: Different views of a simulation of ion trajectories (red) through a quadrupole quadruplet (brown). Trajectories are shown for ions flying left to right parallel to the  $z$ -axis. Black contour lines indicate the electric potential around the electrodes. Simulation produced in SIMION [50].

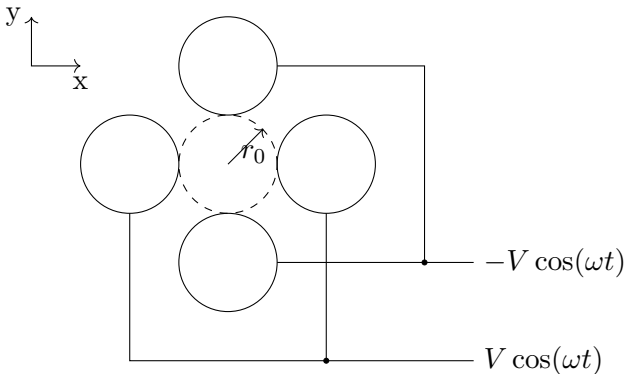


Figure 2.13: Schematic of radio frequency quadrupole (RFQ) rods and their applied bias. Also shown is the radius between rods  $r_0$ .

ability to adjust  $x$  and  $y$  focusing independently.

A limitation faced by all electrostatic optics is that at very low beam energies (10s of eV) ion trajectories become unstable. This instability is due to slow moving ions staying longer within the influence of a given ion optic and any small inhomogeneities in its field [48]. To address this limitation we now introduce dynamic fields to our ion optics.

## 2.3 Radio Frequency Quadrupole Optics

A popular and robust solution for maintaining confinement of low energy ions is to introduce a time-dependent oscillation to the polarities of a quadrupole lens (Figure 2.13). Such oscillations are typically driven in the radio frequency range, creating a category of ion optics known as radio frequency quadrupole or RFQ. RFQ ion optics provide a basis for some mass spectrometer designs, mass filters, ion guides, as well as cooler bunchers and other preparation traps [10][18].

We know from the Laplace equation in electrostatics ( $\nabla^2 V = 0$ ) that a static electric potential must have its maxima and minima at physical boundaries, which in practice are electrodes. However, in RF optics it is possible to have a *time-averaged* field which guides ions *away* from boundaries. We describe the approximation of these average fields by introducing the concept of a *pseudopotential* ( $U^{(PS)}$ ) [18][48]. Just like in real electric potentials, ions in a pseudopotential well experience a force towards minima in the potential. This provides a convenient conceptual tool for understanding and describing the average force experienced by ions in RF fields. In the case of RFQ optics, the minimum in the transverse direction is in the centre of the rod arrangement and the pseudopotential is described as [48],

$$U_{quad}^{(PS)} = \frac{QeV^2}{m\omega r_0^2} \left( \frac{r^2}{r_0^2} \right). \quad (2.7)$$

Here  $Q$  is the charge state of particle,  $e$  the elementary charge,  $r$  the radial position of the particle,  $r_0$  the radius to the inner edge of the quadrupole rods (Figure 2.13),  $V$  the 0-to-peak time varying electric potential on the rods,  $m$  is the particle mass and  $\omega$  is the RF angular frequency.

We see in Figure 2.14 simulations of the transverse motion of an ion relative to the axis of a linear Paul trap. Shown is the combination of a larger macro motion corresponding to the

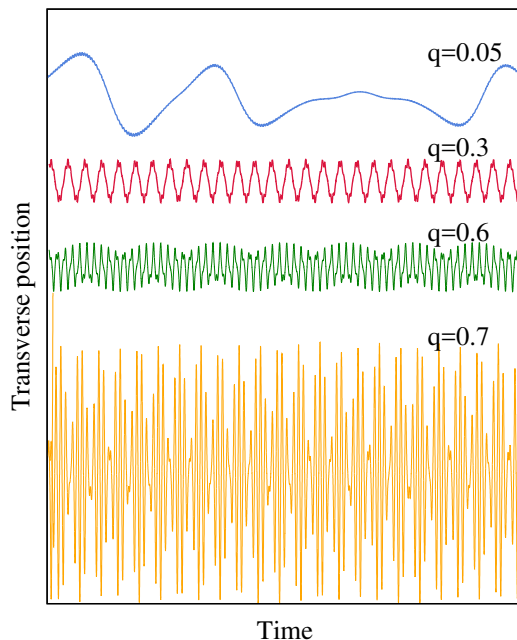


Figure 2.14: Simulated radial ion motion in an RFQ as a function of time for different  $q$ -values. Here an ion of mass 133 u is simulated in a trap with  $r_0 = 10$  mm operated at a frequency of 1 MHz with the voltage varied to change the  $q$ -value. Simulations produced in SIMION [50].

time-averaged fields described by the pseudopotential as well as smaller micro motions arising from the instantaneous states of the RF fields.

Though the pseudopotential is useful for developing an intuition of ion confinement, it does not provide a complete description of the conditions necessary for RFQ ion confinement. An indispensable tool for understanding ion confinement within an RF field is the *stability parameter* ( $q$ )[18], which is calculated as,

$$q = \frac{4QeV}{m\omega^2 r_0^2}. \quad (2.8)$$

In the absence of additional factors such as buffer gas (discussed in the next subsection) or a DC offset in the quadrupole potential [18] ions will be stably confined in an RFQ field if  $q$  is in the interval  $0 < q \lesssim 0.908$  [48]. We see in Figure 2.14 how ion motion becomes larger and more chaotic as it approaches the upper limit of this stable range.

### 2.3.1 RF Ion Guides

If an RF potential is only applied transverse to the beam direction to provide radial confinement we may now introduce a static (DC) axial potential gradient to guide the motion of low energy ions. Methods of creating this gradient include segmenting the RFQ rods [57][58] or rods made of a resistive material which allows a continuous variation in potential [59] (Figure 2.15). Frequently RF ion guides are also filled with a neutral buffer gas to reduce the ion phase space [18][48][10].

### Gas-filled ion guides

We now introduce ion interactions with a buffer gas; this causes ions to tend towards filling a smaller space in the bottom of a pseudopotential well with a smaller emittance. Ions interacting with an ideal gas will tend towards establishing thermal equilibrium with the gas through collisions between molecules. If an ion beam is interacting with a buffer gas with a lower average kinetic energy than the beam, then the beam will typically establish a lower energy thermal equilibrium through a process known as collisional cooling. If the gas is in an open system (constant gas exchange) the beam will be cooled to a consistent temperature which causes a reduction in the energy and spatial spread of the ion beam. To prevent ion losses through charge exchange with the gas we typically use a noble gas such as helium, thus enabling a higher transport efficiency.

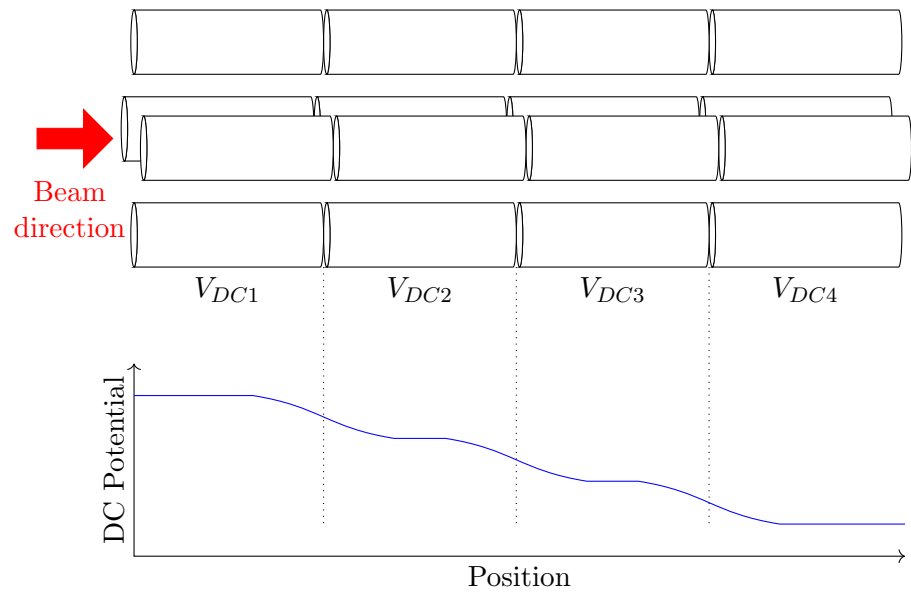
The combination of RF fields with buffer gas creates complications in the theoretical behaviour of particles in both gas and RF fields which must be accounted for. The oscillatory RF field has the effect of “pumping” energy into the system which balances with the cooling effect of the gas. This leads to a higher equilibrium energy than in the absence of RF fields, an effect known as RF heating [60]. RF heating limits the range of values  $q$  may take on to provide stable ion confinement. In the presence of a buffer gas we typically have an upper limit of  $q \approx 0.8$ , though large increases in average kinetic energy may already be observed for  $q > 0.6$  [48]. However, we can typically keep  $q < 0.6$  to safely benefit from the smaller phase space afforded by gas-filled RF ion guides and traps.

### Segmented rods

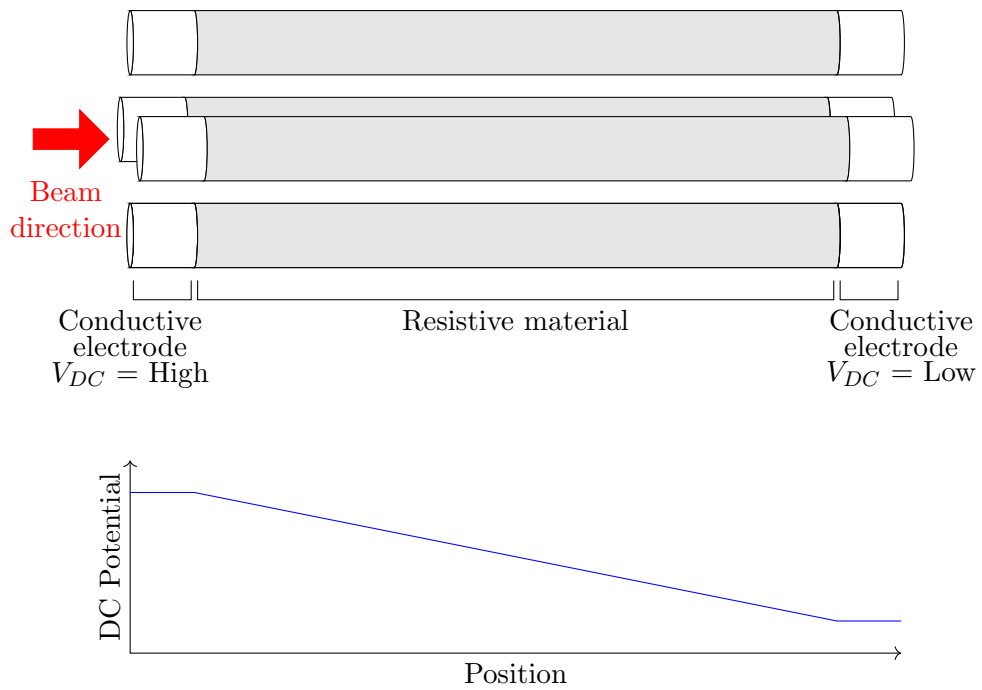
An option for guiding ions in the desired direction through an RF ion guide is to segment the RFQ rods (Figure 2.15 a). Segmented rods are often connected electrically with resistor chains to create a desired DC potential gradient along the length of the rod. Alternatively the segments of such RFQ rods may have independently powered DC potentials to allow greater flexibility in defining the shape and direction of the axial fields, as well as giving the option to trap ions. A key limitation of segmented rods stems from the finite length of the rods which creates flat regions in the axial potential as seen in Figure 2.15 a, which has in some cases inhibited ion transport [59]. Furthermore, segmented rods are more complex to build and operate than resistive rods.

### Resistive rods

Another approach to producing an axial electric field in RFQs is to build the rods from a plastic doped with carbon such as carbon-fibre-reinforced plastic (CFRP) [59]. These rods give a constant resistance per length, allowing an even axial gradient along the rod and are used for ion transport in the TITAN MR-ToF. A photo of an RF ion optical device built with such a material can be seen in Figure 2.16. To control this axial gradient, conductive electrodes must be placed at either end of the resistive rod. The principal disadvantage of these rods stems from the plastic used in their construction. Plastics typically have higher outgassing rates than metals [61] which tends to increase the gas pressure, as well as adding contamination to the beam in the form of organic molecules. As a result, it may be necessary to have high pumping capacity to maintain a high vacuum, also there may be greater ion losses through charge exchange with the organic molecules. Low pressures can be very important in contexts such as an MR-ToF where large losses in efficiency have been observed at pressures greater

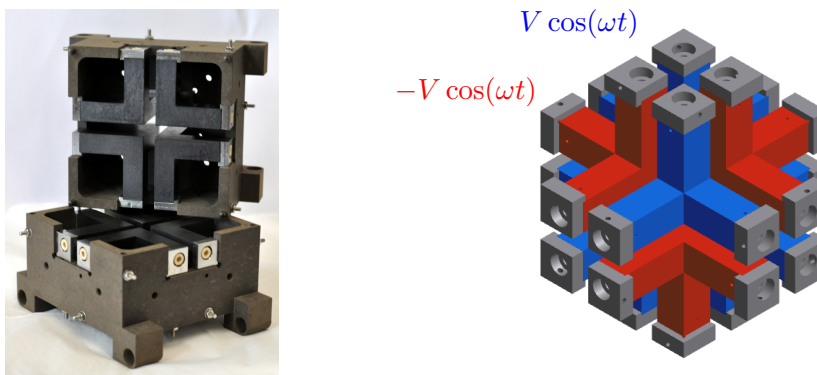


(a) Segmented RFQ rod.



(b) Resistive RFQ rod.

Figure 2.15: Two schematics and corresponding linear potentials of RFQ ion guides.



(a) Photo of switchyard.

(b) RF arrangement of electrodes.

Figure 2.16: Images of RFQ switchyard. a) Photo of the switchyard partially assembled. The carbon-doped plastic electrodes are visible here. b) Rendered model showing the phases of the applied biases on the switchyard in red and blue.

than  $10^{-7}$  mbar [54]. One benefit of building RF optics out of plastic is that it becomes easier to construct different shapes, creating curved paths or other complex arrangements [48].

### RF switchyard (cube)

One of the complex RF ion guide constructions which benefits from resistive carbon doped plastics is the RF switchyard or “cube” designed for the TITAN MR-ToF [62]. The design of this switchyard is reminiscent of six quadrupole ion guides converging to a single intersection from perpendicular directions. There are eight electrodes built in a three dimensional “L” shape with conductors at the ends to set the electric potentials along the electrodes (Figure 2.16). As with other RF ion guides, radial confinement is maintained through the RF switching potentials and ions are moved in the desired direction through application of DC potentials. An overview of the DC potentials used for its operational modes is shown in Figure 2.17. This design is used in the TITAN MR-ToF transport system to allow a robust transport of ions into or out of the switchyard from any of the six directions as well as merging beams from two directions which is then extracted in a third direction. The RF switchyard provides greater flexibility than electrostatic counterparts, such as the switchyard in the TITAN beamline for transport to the EBIT (Figure 2.18). The EBIT switchyard lacks the capacity to merge two beams and is also a much larger structure ( $\sim 1 \text{ m}^2$  compared to  $\sim 10 \text{ cm}^2$ ). A diagram of the TITAN MR-ToF and its transport system, including the various RF optics described here is shown in Figure 1.6.

### 2.3.2 Linear Paul Traps

There are a variety of cases in which one may want to use the principles of RF ion confinement for the trapping of ions. Applications of RF ion traps include mass spectrometry, ion storage [18], and cooling and bunching continuous ion beams [5] to prepare them for injection into another device. To accomplish these goals, we may for example take an RFQ ion guide built with segmented rods then set a high potential on the end segments of the rods and low potentials on the middle segments (Figure 2.19). The result of such an arrangement is a class of ion trap known as a linear Paul trap or simply a linear ion trap [18].

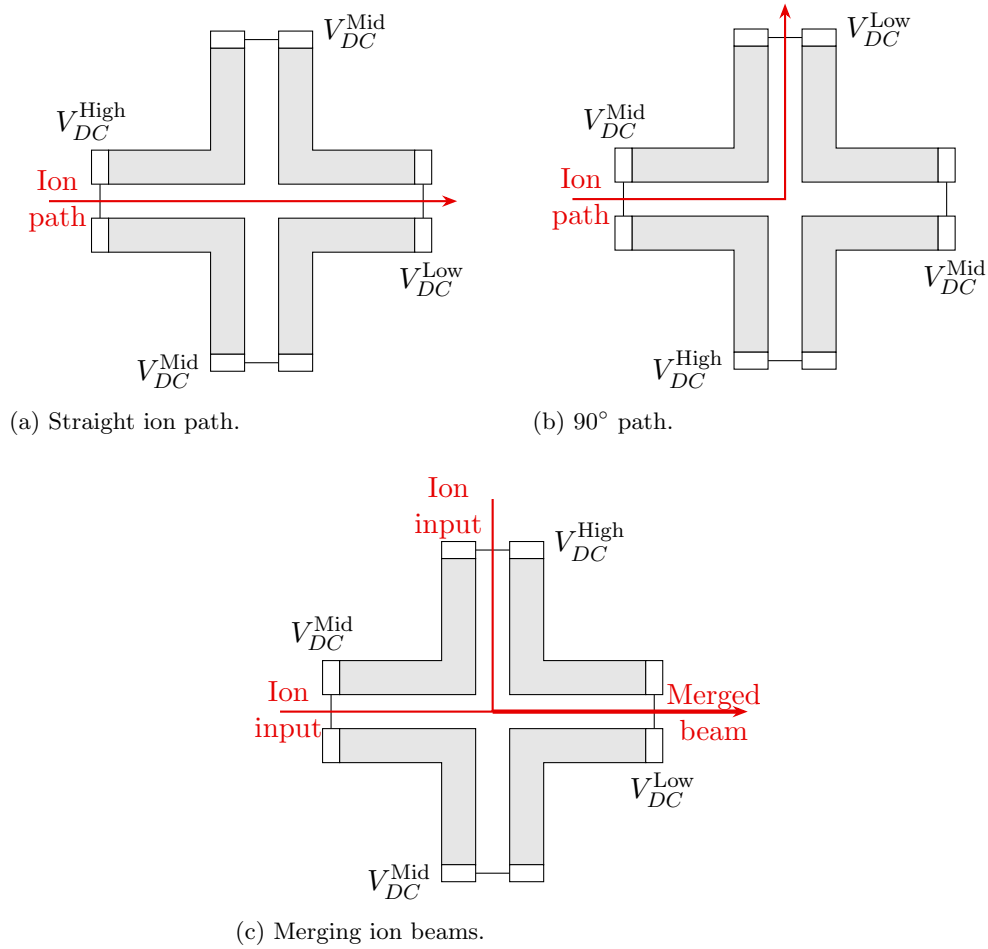


Figure 2.17: Diagrams of the RF switchyard ion guide indicating relative strengths of the DC potentials to allow ions to pass through the switchyard in: a) a straight path, b) a 90° path, or c) merge beams from two directions into a single path.

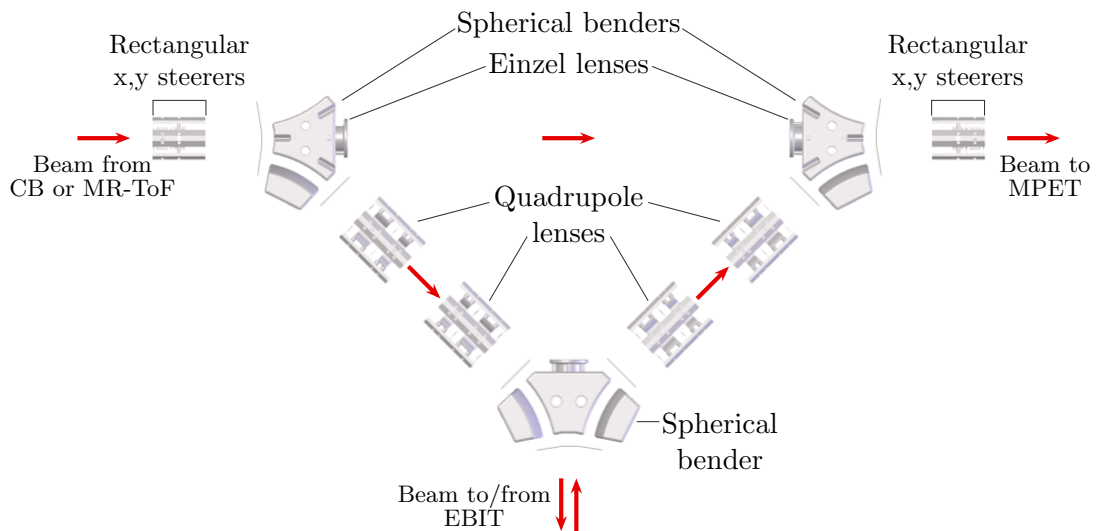


Figure 2.18: TITAN beamline electrostatic switchyard.

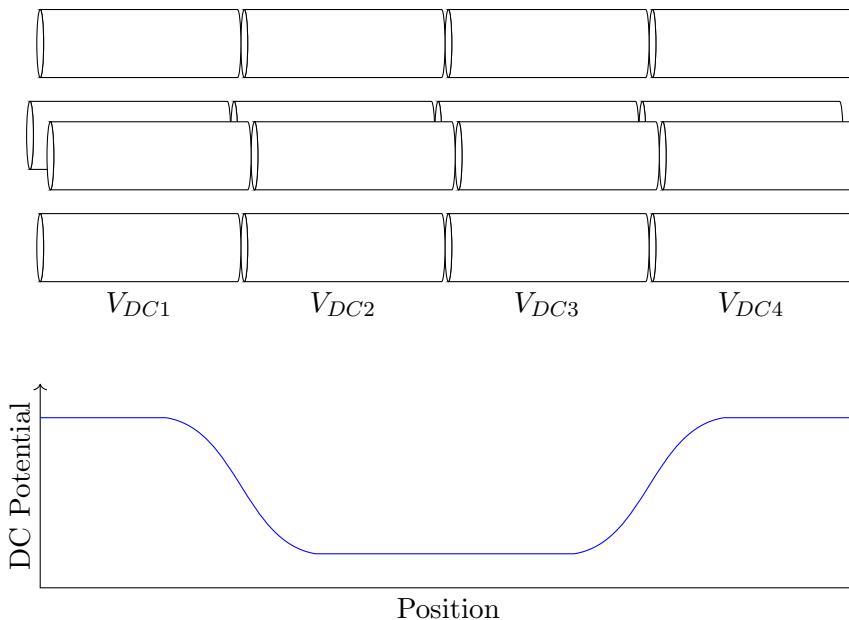


Figure 2.19: Top: Schematic of a linear Paul trap based on segmented rods. Bottom: Example of linear potential used to trap ions.

### RFQ Cooler Buncher

Trapping can typically be achieved with fewer ion losses and higher mass separation resolving power with bunched beams, yet often ion sources produce continuous beam. In addition, a continuous high-energy beam of modest emittance will have a much larger emittance when slowed to very low energies for trapping due to the relation described by Equation 2.2. For example, in the LEBT section of the ISAC facility a typical beam might be at an energy of 60 keV with a transverse emittance of  $150 \mu\text{m}$  [34]; electrostatically slowing this beam to 4 keV we would expect the transverse emittance to increase to  $580 \mu\text{m}$ . To avoid this, TITAN uses a class of linear Paul trap called an RFQ cooler buncher (CB) to achieve an emittance of  $12.5 \mu\text{m}$  at 4 keV [63]. Thus using a CB we are able to convert the higher energy continuous ISAC beam to a low-energy, low-emittance bunched beam to facilitate Penning trap mass measurements.

As with gas-filled RF ion guides a CB is filled with a neutral buffer gas which reduces the phase space of incoming ions through collisional cooling. Collisional cooling is only effective for cooling beams with energy on the order of 10 eV; at higher energies the beam would be moving too quickly to be cooled in the trap. To compensate for this cooling limitation the entire trap will typically be given a DC bias potential slightly below the incoming beam energy to slow the beam electrostatically before entering the trap. A DC potential gradient is then set such that ions will be guided to the extraction end of the CB while remaining trapped prior to ejection. The quantity of ions in a given bunch will be determined by the continuous beam current entering the trap, the collection time in the trap, and the limit at which Coulomb repulsion will force ions out of the trap (space-charge limit).

Ions cooled in the CB are gathered to an axial DC potential well near the end of the trap as like that shown in Figure 2.20 b. Ions are gathered in this well to form a bunch prior to being ejected from the CB. Typically extraction is accomplished by lowering the DC potential on the output end of the trap to allow ions to escape, creating a field which “pulls” the ions out of the trap. Sometimes this pull may be accompanied by a raising of the potential behind the bunch

to add a “push”. Various electrode arrangements on the extraction end may be used to shape the electric field extracting the ions to control the longitudinal emittance of the bunch leaving the trap [5].

A small linear Paul trap is used for injection of ions into the TITAN MR-ToF (“Trap System” in Figure 1.6). This trap also is used to recapture ions which have been separated in the MR-ToF mass analyzer and remove isobaric contamination through mass-selective re-trapping, described in Reference [42].

The main CB in the TITAN beamline provides the entry point for ions into the TITAN beamline, applying the cooling and bunching process to continuous 20 keV ISAC beam. The import of this CB to TITAN is such that we adopt the short-hand of referring to it as *the* TITAN CB. This CB uses segmented RFQ rods to control axial potentials for ion trapping and ejection. The rods each have 24 segments, with shorter segments near the ends of the CB to allow greater control of the electric fields near the ejection point. An overview of the rod segments and their numbering is shown in Figure 2.20 a). During ion cooling and bunching the segments have DC potentials set for trapping, with segment 23 having the lowest potential, defining where ions will gather. For ion ejection, segments 22 and 24 are switched to allow the ions to escape the CB. These DC potentials are shown in Figure 2.20 b).

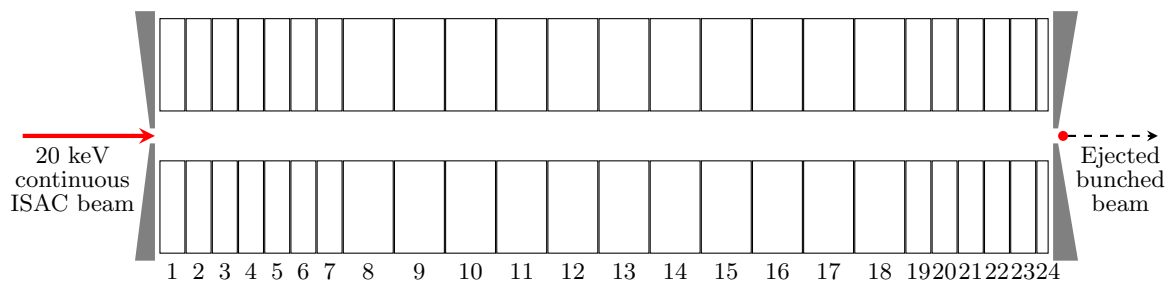
This particular CB uses square-waves to drive the RF switching of electrodes [34] instead of the more common sinusoidal waves. The advantage of the square-wave driven RFQ is in the flexibility of frequency achievable. Most sinusoidal driven RFQs have a specific optimal operational frequency, effectively limiting the RFQ to a single frequency thus limiting the range of masses which may be stably confined. The electronics necessary for the square-wave drive allow a range of frequencies to be used, making a larger range of masses accessible using this CB.

Ions ejected from the CB enter a pulsed drift tube which is set with a potential below that of the CB so as to accelerate ions to the chosen beam energy. Pulsing of the drift tube is set so that when ions are in the middle of the tube, the drift tube potential will be lowered to ground. This allows the potential energy of the ions to be lowered without subjecting the ions to any accelerating field. Once the ions have left the drift tube they may then be transported through an electrostatic beamline towards the other ion traps in TITAN for further preparation and/or measurement.

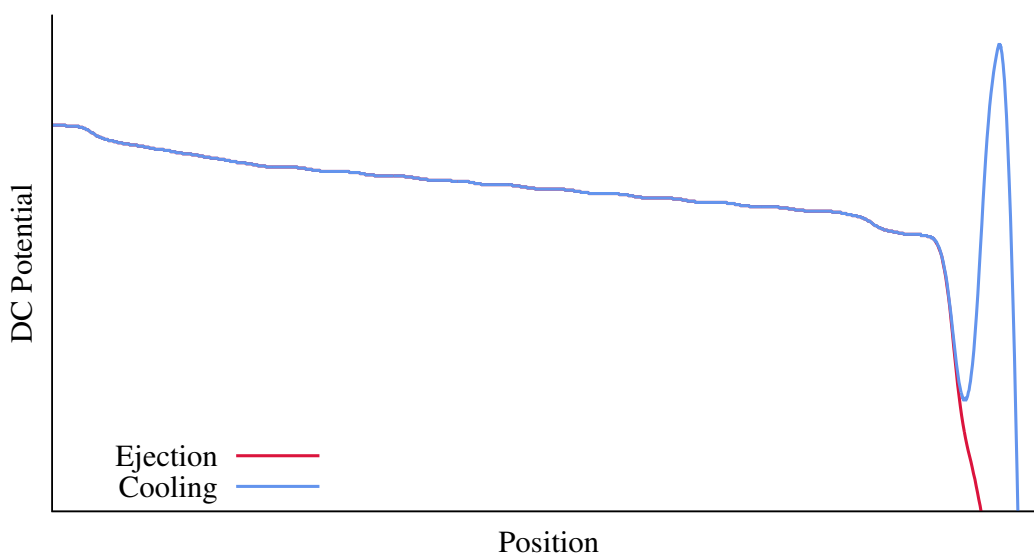
## 2.4 Summary

Through this chapter we have discussed the ion optics which are relevant for the work of this thesis. The main focus of the following is: transporting ions into the TITAN MR-ToF for mass measurement and isobar separation; transport of isobar separated ions from the MR-ToF to MPET; and bypass of the MR-ToF when not in use. To accomplish this goal a variety of electrostatic ion optics have been discussed including Einzel lenses and quadrupole multiplets for beam confinement and focusing. Parallel plate benders are used to curve and correct ion paths, of these, rectangular and spherical benders are used in the TITAN beamline. In addition to the electrostatic optics used for ion transport we also discussed the electrostatic mirrors used to perform mass measurement and isobar separation in the MR-ToF mass analyzer.

Various RFQ ion optics are used for beam preparation and as ion guides. 20 keV continuous ISAC beam entering TITAN is cooled and bunched in an RFQ CB before injection into the TITAN electrostatic beamline. The TITAN CB uses segmented RFQ rods to gather ions near the end of the trap before ejection. The TITAN MR-ToF has a set of gas-filled RF ion guides



(a) Cooler Buncher segments and their numbering.



(b) Cooler Buncher potentials.

Figure 2.20: Schematic of the TITAN cooler buncher [34] electrode configuration. a) The arrangement of 24 rod segments which can each be given a different DC potential. Ions are trapped in the region of segment 23, then segments 22 and 24 are switched to allow ions to escape the trap and be directed into the TITAN beamline. b) A SIMION [50] calculation of the DC potential for cooling (blue) and ejection (red) as a function of linear position in the CB.

built with resistive RFQ rods to transport ions in and out of the MR-ToF mass analyzer. The MR-ToF transport section includes a novel RF switchyard which enables ions to enter and exit a cube-like structure from any of six directions as well as allowing the merging of two ion beams.

With an understanding of the principles of these ion optics we are now ready to apply this knowledge to an investigation of the TITAN beamline, particularly for transport of ions into, out of, and around the MR-ToF.

## Chapter 3

# Beamline studies for MR-ToF integration

The value of the MR-ToF to the scientific program at TITAN depends on the ability of the MR-ToF to function as an integrated part of the whole TITAN system. Previous work has included the design, construction and initial testing of the device [43]; then offline commissioning which showed the TITAN MR-ToF is capable of performing mass measurements and isobar separation at or above required performance [44]. For offline commissioning the MR-ToF and its transport system were operated as a standalone device, performing tests with an ion source located just below the input optics seen in Figure 1.6. With the completion of this previous work, the next step was to integrate the MR-ToF into the TITAN beamline. Simulations were performed to examine beam behaviour when being transported into, out of, or bypassing the MR-ToF. As a result, a new split Einzel lens was introduced into the TITAN beamline to improve transmission into the MR-ToF. The impact of this lens on the TITAN beamline has been examined. Simulations were validated against experimental studies, looking at time profiles of the beam at two locations as well as measurements of the transverse emittance of a beam transported towards the MR-ToF.

### 3.1 The TITAN beamline prior to integrating the MR-ToF

A schematic overview of the TITAN beamline prior to the installation of the MR-ToF is shown in Figure 3.1, with clarification on notation found in Table 3.1. This portion of beamline has been the focus of study for this chapter. Also indicated is where the MR-ToF was installed and locations of modifications made to the beamline optics to improve the efficiency with which ions can be transported into the MR-ToF from the CB. The function of most of the ion optics outlined in Figure 3.1 have been explained in Chapter 2 with a few exceptions: The indicated skimmer plates are grounded under normal operation and used to limit the range of the electrostatic fields to near the electrodes producing the fields. Most of the spherical benders are  $36^\circ$  benders with an additional  $9^\circ$  provided by neighbouring rectangular benders, with the exception of the B1 bender which is a  $45^\circ$  spherical bender. Differential pumping apertures are used to limit gas flow between regions of the beamline at different pressure levels. For example, the right side of the TSYBL:DPA aperture is typically at  $10^{-7}$  mbar, whereas to the left a pressure of  $10^{-10}$  mbar is maintained.

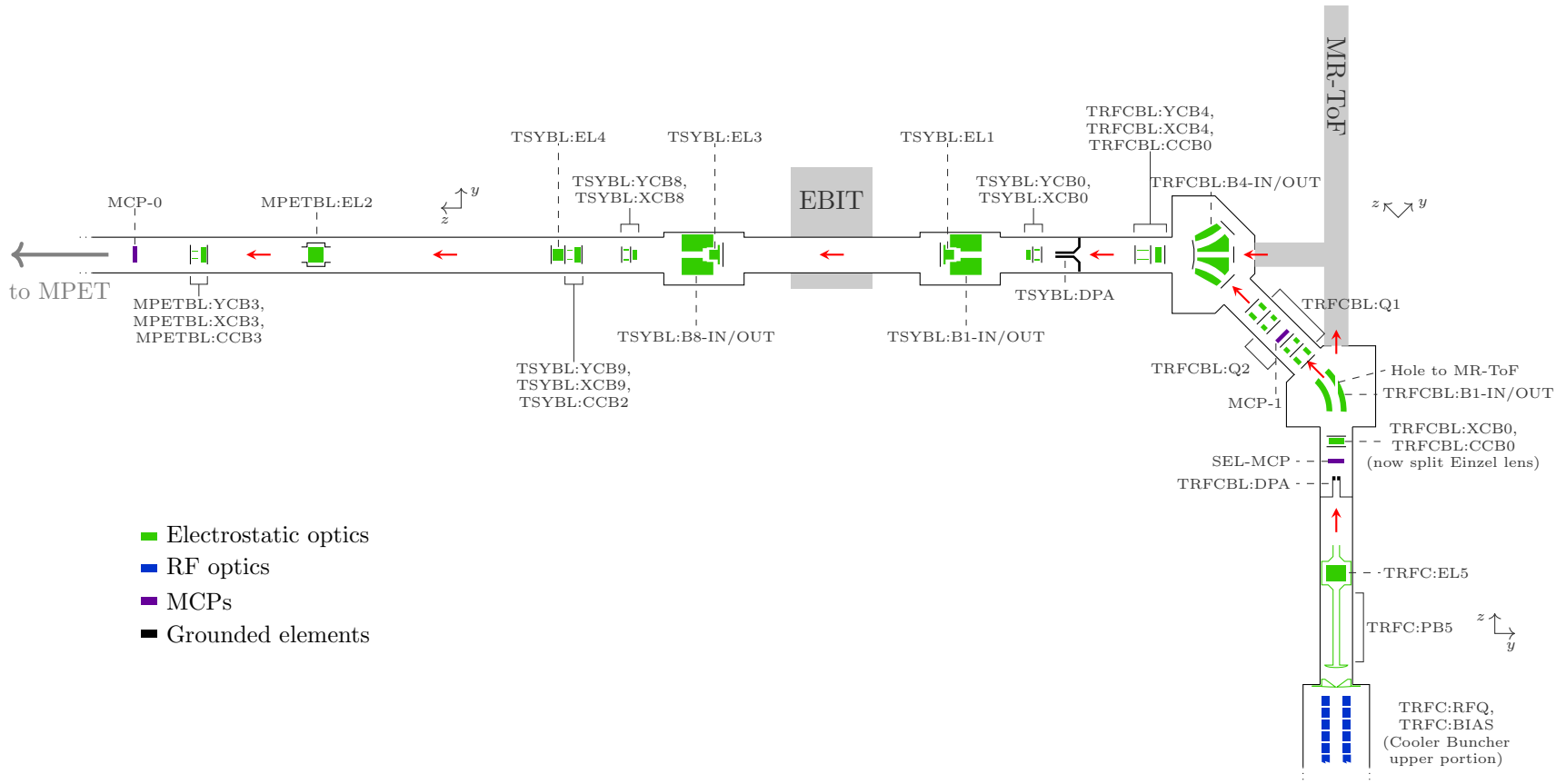


Figure 3.1: Schematic overview of the TITAN beamline optics between the Cooler Buncher and MPET as relevant for simulations presented herein. Electrodes are labelled first with a section label, then the optics type and assigned number. Electrode types are summarized in Table 3.1. Black lines appearing before and after many electrostatic optics are “skimmer” plates. Red arrows indicate the beam path and direction. The MR-ToF and EBIT optics are not shown.

Table 3.1: A summary of the labels and corresponding purpose for the ion optics and apertures in the TITAN beamline. Positions of these are indicated in Figure 3.1.

Label	Purpose
RFQ	CB RFQ rod segment DC voltage
BIAS	DC bias on CB
PB	Pulsed drift tube
EL	Einzel lens
XCB	Rectangular parallel plate benders for x-direction
YCB	Rectangular parallel plate benders for y-direction
CCB	Power supply shared between XCB and YCB benders
B-IN	Spherical bender inside electrode
B-OUT	Spherical bender outside electrode
DPA	Differential pumping aperture

### 3.1.1 Beamline simulations

As a preparation for integrating the MR-ToF the TITAN beamline was modelled in the simulation software SIMION 8.1 [50]. SIMION allows numerical calculations of electric and magnetic fields and resulting trajectories of charged particles through these fields [64]. Further discussion of SIMION may be found in Appendix A. These simulations were used to better understand ion transport in the beamline and to predict optimal settings on the ion optics to facilitate ion transport into, out of, and bypassing the MR-ToF.

#### Cooler Buncher

To define initial conditions of ions, simulations of the TITAN CB were created based on previous work described in [65]. Past simulations focused on the cooling of 20 keV ISAC beam and extraction into optics planned for offline testing of the CB. For this thesis work the focus was not on the cooling process—as it is well established—but instead, the TITAN beamline and the role of the CB therein. As such, only segments 18–24 of the CB were simulated. By neglecting the other 17 segments, sufficient computing resources were available to increase the PA resolution from 1 grid unit per mm to 0.5 grid unit per mm. This allowed a more accurate modelling of a 5 mm diameter circular aperture at the exit of the CB. We can see in Figure 3.2 differences in how the aperture edge is modelled at different resolutions. 2–3% of ions ejected from the CB in simulation were lost at this aperture, thus it is important to ensure that the portion of ion phase space being removed reflects what is lost in the real aperture.

$^{133}\text{Cs}^+$  ions were created in simulation in a random spherical Gaussian phase space distribution determined from previous CB simulations of cooled ions. Specifically, with a standard deviation in position of 0.62 mm and velocity of 0.1 mm/ $\mu\text{s}$ . This was centred on the  $z$ -axis in the middle of the length of segment 23 (see Figure 2.20). To protect against any possible errors in this initial phase space distribution, simulations allowed ions to cool for 100  $\mu\text{s}$  in the buffer gas before ejection into the TITAN beamline.

An initial benchmark used for this CB simulation was a comparison to results reported in Reference [65] shown in Table 3.2.  $\Delta V_{22}$  and  $\Delta V_{24}$  refer to the DC potentials on segments 22 and 24 relative to segment 23 (see figure 2.20), then the rms emittance values for these settings were simulated and recorded. Reference [65] reports using a q-value of 0.4 and  $V_{pp}$  of 400 V for simulating  $^{133}\text{Cs}^+$  ions, requiring a simulated RF frequency of 606 kHz. The reported gas

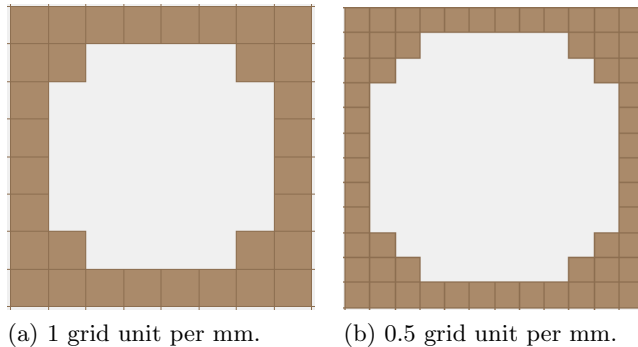


Figure 3.2: Two examples of how a 5 mm diameter circular aperture is modelled in SIMION at different resolutions.

Table 3.2: Comparison of CB simulation results produced for this thesis to results obtained in [65]. Differences between the simulations range from 1% to 35%. Unit convention for reporting transverse emittance follows that of [65].

$\Delta V_{22}$	$\Delta V_{24}$	This Thesis		Reference [65]		Difference	
		$\epsilon_{trans}$ ( $\pi$ mm mrad)	$\epsilon_{long}$ (eV $\mu$ s)	$\epsilon_{trans}$ ( $\pi$ mm mrad)	$\epsilon_{long}$ (eV $\mu$ s)	$\epsilon_{trans}$	$\epsilon_{long}$
0	-30	$3.52 \pm 0.11$	$5.81 \pm 0.17$	$3.3 \pm 0.3$	$4.7 \pm 0.2$	6.7%	23.7%
0	-60	$4.16 \pm 0.12$	$7.5 \pm 0.2$	$4.2 \pm 0.1$	$7.4 \pm 0.3$	1.0%	1.0%
30	-30	$3.31 \pm 0.10$	$1.75 \pm 0.05$	$3.8 \pm 0.2$	$1.3 \pm 0.1$	12.8%	34.6%
60	-60	$3.39 \pm 0.10$	$1.79 \pm 0.05$	$3.6 \pm 0.1$	$1.4 \pm 0.1$	5.7%	27.7%
500	-500	$3.27 \pm 0.10$	$1.95 \pm 0.06$	$4.8 \pm 0.2$	$1.8 \pm 0.1$	31.9%	8.5%

pressure is  $2.5 \times 10^{-2}$  mbar with a temperature of 300 K. In addition, a rise time of 10  $\mu$ s was used for the switching of segments 22 and 24 from trapping to extraction mode.

The comparison in Table 3.2 shows emittance values differing between 1% and 35%. The known differences between these simulations and those in [65] are the difference in extraction optics, the initial phase space distribution, and the change in simulation resolution. Ion extraction from the CB was done with optics for a test stand used in offline testing, whereas for this thesis the extraction optics of the TITAN system were used. Inconsistencies may also arise due to any non-linear evolution of the rms emittance through the different optics. As noted on page 12, the calculated value for rms emittance depends on how ions are distributed in phase space and will, for example, be inflated by filamentation of the emittance. Another concern is any unanticipated sensitivity to the initial ion phase space distribution. The precise initial distribution used in [65] is unknown, thus this could not be exactly reproduced. Finally, the increased simulation resolution may have had an impact, though this has not been tested. It was observed that 2–3% of ions simulated in the CB are lost on extraction; the phase space properties of these will be affected by the shape and size of the aperture where the ion losses occur. As seen in Figure 3.2, this is impacted by the simulation resolution which could in turn have a measurable effect on the emittance. However, further exploration of these differences was eschewed in favour of the more crucial matter of reproducing experimental results. To this end we shall compare CB simulation results to measurements of transverse emittance and beam time profiles in the Sections 3.1.2 and 3.1.3 respectively.

### 3.1.2 Allison meter emittance measurements

To further our understanding of the CB performance and to experimentally test the validity of these CB simulations emittance measurements of the beam from the CB were performed. The tool used to measure the beam emittance was an Allison meter [66]. The principle of an Allison meter is to sample the number of ions detected across a grid of points in trace space one at a time. An outline of the components used in this sampling is shown in Figure 3.3. The meter is moved between  $x$ -positions using an actuator. At each position the divergence  $x'$  is measured by varying the voltage difference on the plates  $V$  such that only ions of a particular divergence will reach a MicroChannel Plate detector (MCP) [67] on the opposite end of the Allison meter. The divergence is calculated as,

$$x' = \frac{L_{eff}}{4gE}V, \quad (3.1)$$

where  $L_{eff}$  is the length of the parallel plates in the direction of beam propagation,  $g$  is the gap between plates, and  $E$  is the beam energy. At each position and voltage setting the number of ions successfully passing through the detector are counted with an MCP from which a density plot of the emittance may be determined. As explained earlier, because the edges of such distributions are not clearly defined we use rms emittance to quantify the emittance.

The Allison meter was placed at the top of the B1 bender box in the TITAN beamline (Figure 3.1) to measure beam emitted from the CB to the location where the MR-ToF input optics would eventually be located.

These measurements used  $^{133}\text{Cs}^+$  ions produced in the TITAN internal ion source (located below the CB [73]). The CB was operated at current standard operating parameters with a frequency of 480 kHz with a peak-to-peak voltage of 170 V ( $q = 0.27$ ) and gas pressure of  $10^{-2}$  mbar at room temperature. DC voltages are listed in Appendix B.

#### Analysis of raw data

Raw data from the Allison meter was analyzed using a script in the programming language Lua 5.1 (shown in Appendix D). The methodology is adapted from MATLAB code developed for beam analysis use at TRIUMF [68].

To convert the MCP signal into ion counts a Multi-Channel Scalar (MCS) was used. On the MCS a discriminator is used to set a voltage threshold which must be overcome for electrical pulses to be treated as real counts from the MCP. For each cycle the MCS would acquire counts over a time of 81  $\mu\text{s}$ , placing counts in bins 40 ns wide. The signal from the MCP could then be identified by the corresponding peak in the time profile recorded at the MCS.

Fluctuations were observed in the threshold set on the MCS discriminator which caused changes in the number of MCP ion detections counted. This effect on the counted ions is due to variations in the energy deposited on the detector by a given ion; some ions will deposit more energy, producing voltage spikes above the discriminator threshold, others of lower energy, falling below the threshold. The result is that a drifting threshold will change the average ions counted for a constant ion current. To minimize the uncertainty created by this drift, another MCP (MCP-1) was used to provide a constant beam current measurement for normalization of the Allison meter MCP signal. To produce this signal, a switch was used to turn the TRFCBL:B1 bender on and off so that ions would alternate between being sent to the Allison meter and being sent to MCP-1. By assuming a constant ion current to MCP-1 the signal detected by the Allison meter was normalized.

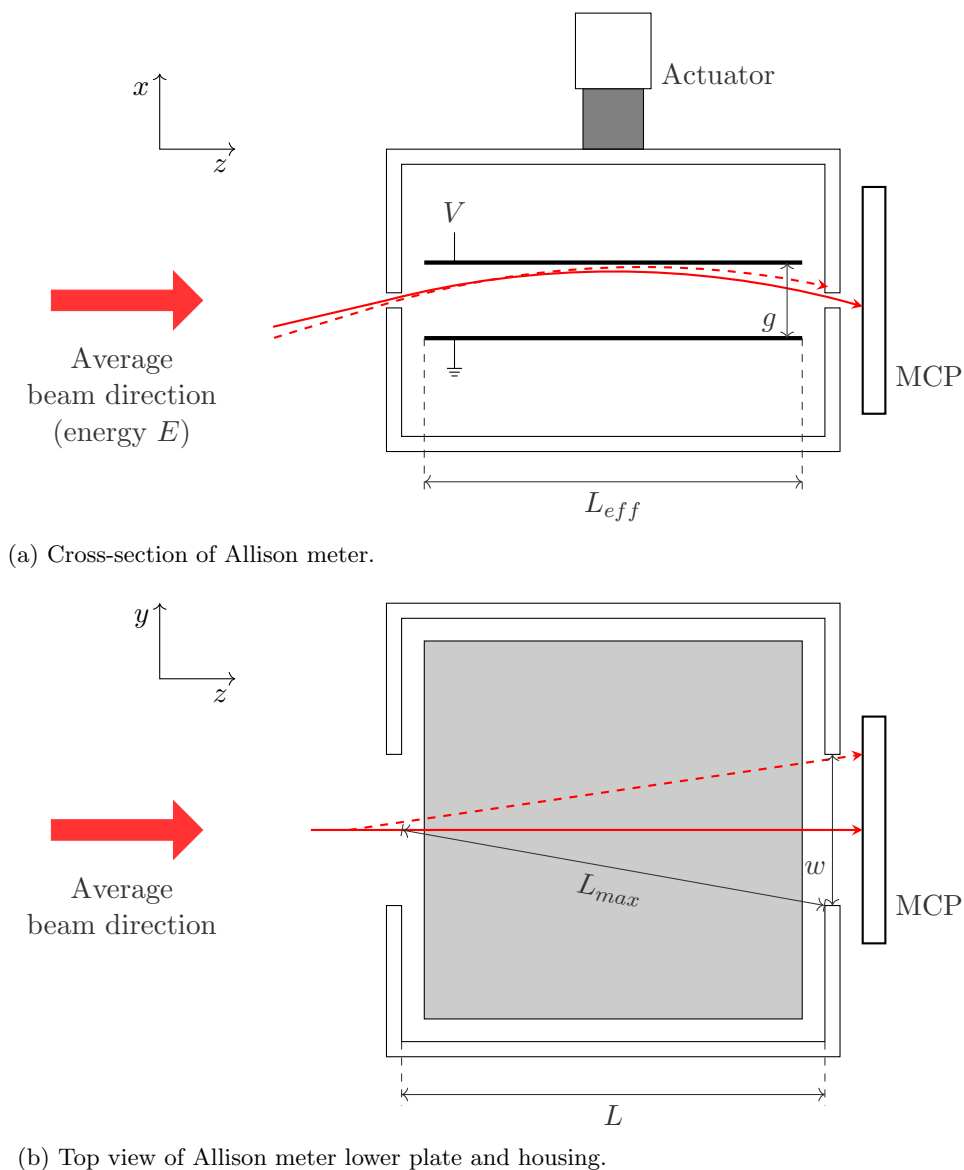


Figure 3.3: Schematic diagrams of an Allison meter used for measuring beam transverse emittance. Red lines indicate example paths of individual ions passing through the meter; the solid line shows a transmitted ion and the dashed line indicates a) an ion entering along a path which will not pass through the meter, or b) an ion which passes through the detector at the very edge of the detector slit.

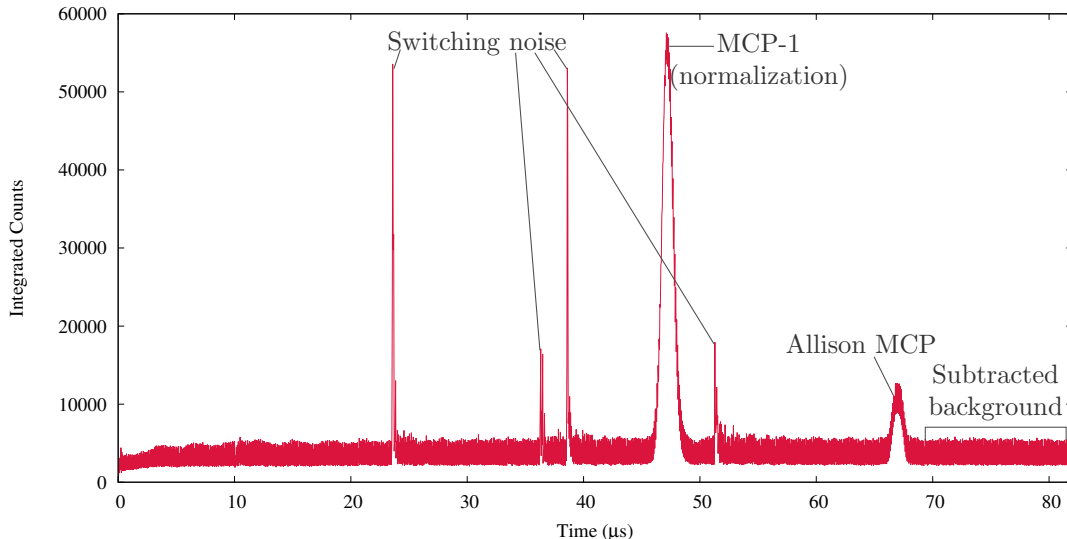


Figure 3.4: Detected signals at MCP-1 and the Allison MCP as a function of time. Various peaks are indicated. Highlighted are the interpretations of specific peaks in the time-of-flight spectrum as well as the sections of data used to produce the emittance measurement. This example is an integration of all the time profiles for a specific measurement.

An additional step in determining ion counts was accounting for background noise. A section of the detected time profile separate from any signal was selected to calculate the mean average of the background. This background was normalized to MCP-1. The mean background was subtracted from each bin counted by the Allison meter MCP.

An example of all time profiles for a complete emittance measurement is shown in Figure 3.4. It highlights the peak from the MCPs and the region used for background subtraction. Alternatively we may see a summary of all the MCS data recorded for an emittance measurement in Figure 3.5. This plot presents each time profile vertically as a density plot. Each successive time profile is numbered with a Measurement Index. The order in which the profiles were produced was to cycle through all voltage settings from most positive to most negative at a set Allison meter position. Then the meter would be moved to the next position and the process of cycling through the voltage settings would be repeated. We can see the effect of only some voltage and position settings allowing transmission of ions to the Allison meter MCP by what appear to be dots in the density plot at approximately  $68 \mu\text{s}$ .

Combining this Allison meter position, divergence (from voltage, using Equation 3.1), and ion count data we may produce a plot such as those in Figure 3.6. Figure 3.6 a and b show the impact of normalizing with MCP-1. In Figure 3.6 c the  $z$ -axis has been rescaled to make visible the background noise which is  $\lesssim 2\%$  of the maximum ion count. This noise must be excluded for rms emittance calculations, otherwise false counts will distort our results. To remove this effect we set a threshold which ion counts must surpass to be counted. This threshold was set as three standard deviations of the ion counts in a background region of the emittance plot, far from the real data. By setting ion counts below the threshold to zero, some real counts will be removed along with the noise, thereby artificially lowering the calculated emittance. To account for this effect we introduce an inflation factor  $ifac$  equal to the ratio total ion counts to ion counts removed by the threshold. Assuming a bi-Gaussian ion phase space distribution

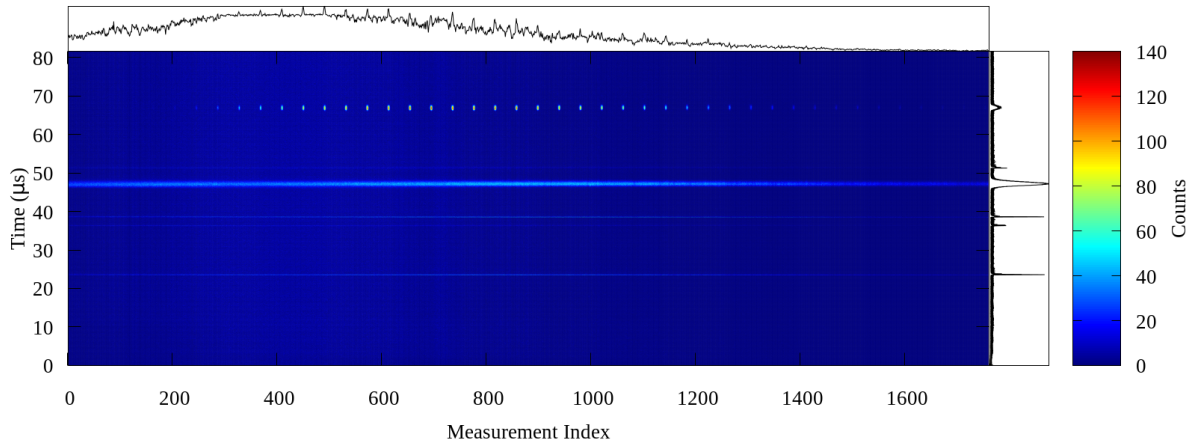


Figure 3.5: Detected MCP signal as a function of time as function of Measurement Index for a complete Allison meter emittance measurement. Individual time profiles are presented as density plots parallel to the  $y$ -axis. The time profiles are arranged horizontally in the order they were taken. Integrated projections of the data along the  $x$ - and  $y$ -axes are shown above and to the right of the density plot. Allison meter MCP signal can be seen as dots at approximately  $68 \mu s$ .

we find,

$$ifac = \frac{pfac}{pfac - (1 + \log(pfac))}, \quad (3.2)$$

where we define  $pfac$  is the ratio of the peak number of counts in the emittance distribution and  $thresh$  is the level of the threshold in counts:

$$pfac = \frac{peak}{thresh}. \quad (3.3)$$

We expect the real emittance value to be somewhere between  $\epsilon_{rms}$  and  $ifac \cdot \epsilon_{rms}$ .

The result of this analysis for the described CB operating parameters is shown in Figure 3.6 d. Further details of this analysis methodology are outlined in Appendix C.

### Measurement uncertainty

There are three quantities which are required for the measurement of an emittance value, each introducing its own uncertainty the: ion position, divergence, and counts per parameter set. The Allison meter was positioned using a Thermionics Northwest FLMR-275-50-4/MS actuator driven by a Lin Engineering 5718X-18DE-01 stepper motor. The actuator is specified as having 20 turns/inch and the stepper motor to have 200 steps per turn, together giving  $6.35 \times 10^{-3}$  mm/step, which was experimentally verified. From this we estimate the accuracy of the actuator precision to half a step, thus we assign an uncertainty of  $\delta x \approx 3.2 \times 10^{-3}$  mm.

The process of estimating the uncertainty of  $x'$  was a more complex process due to the multiple components in the measurement indicated in Equation 3.1. The energy spread  $\delta E$  had been estimated using a Retarding Field Analyzer (RFA) [69] and found to be 4 eV. The RFA is described in Reference [70], and these specific measurement are from diagnostics of the TITAN system [71].

The voltage  $V$  applied to the Allison meter was measured using an Agilent 34401A Digital Multimeter. The accuracy of this multimeter is specified as  $\pm(0.0002\%$  of the reading +  $0.0001\%$

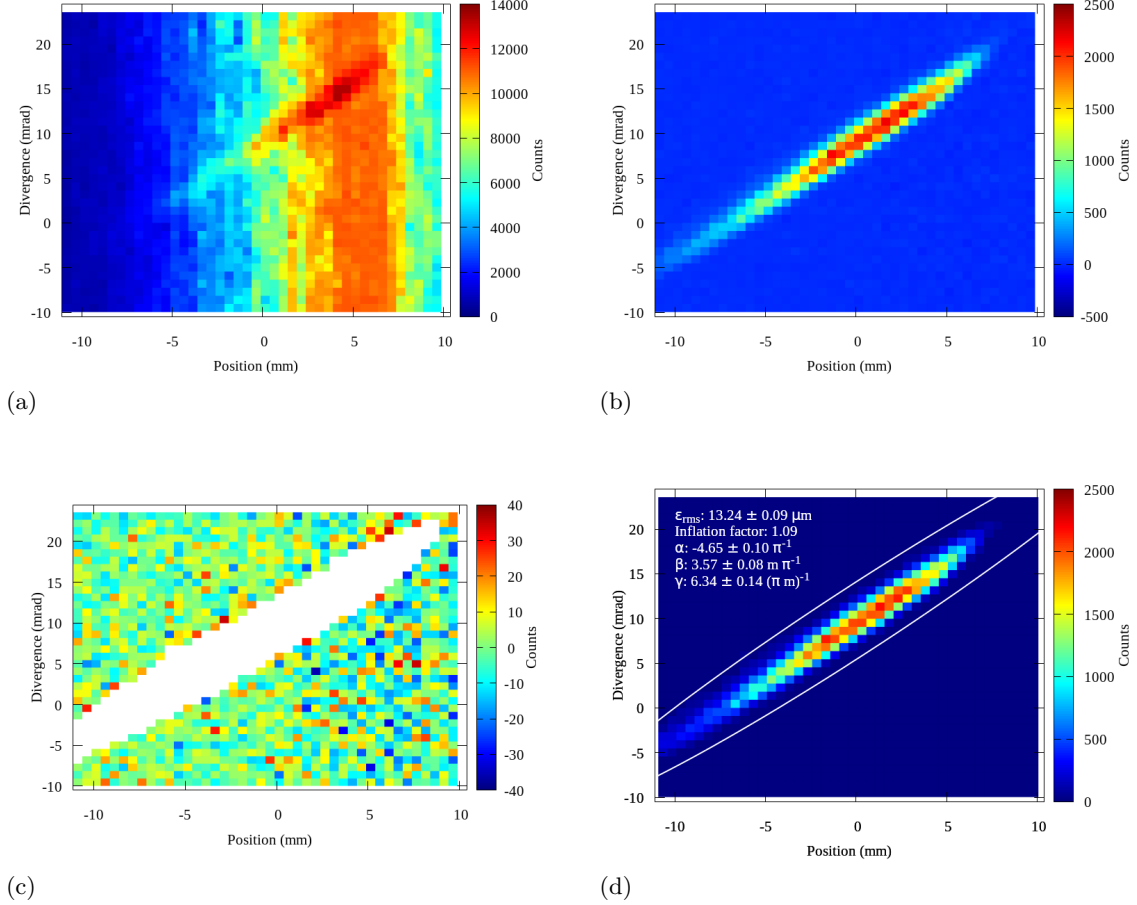


Figure 3.6: Emittance plots from one measurement of a  $^{133}\text{Cs}^+$  beam out of the TITAN CB with a standard operating parameters (described in text), showing different levels of processing of the number of ions detected at each position and divergence. a) An emittance plot with no processing of the ion counts, showing a large biasing effect due to drift in the MCS. b) An emittance plot with ion count normalization and time-profile background removed, but before a threshold was set to remove background counts for rms emittance calculation. c) The same emittance plot as b), but scaled in the z-axis to highlight the degree of variation of the background counts. Background variations on the level of 2% of the peak ion counts can be seen. d) An emittance plot after the complete ion-count processing described in the text. This plot includes the calculated rms emittance and Twiss parameters. A white ellipse calculated from the Twiss parameters is overlaid on the plot with the size set by the equivalent emittance  $4\epsilon_{rms}$

of the range). For the range of voltages measured the highest relative uncertainty had a value of  $\delta V/|V| = 5.5 \times 10^{-5}$ . Given that this value is one or more orders of magnitude smaller than other uncertainties relevant to calculating  $x'$ , this maximum  $\delta V/|V|$  was applied to all voltage measurements to be conservative.

The accuracy of  $g$  and  $L_{eff}$  were subject to the uncertainty determined by the tolerances specified for their manufacture.  $\delta g$  was estimated as 0.04 mm; however the process of determining  $\delta L_{eff}$  was complicated by the width of the slit through which ions enter the Allison meter (denoted as  $w$  in Figure 3.3 b). Because of the slit width, it is possible for ions to be crossing over the plate on a diagonal path, thus longer than if they had passed straight over the plate, creating a larger  $L_{eff}$ . We estimate an upper limit on this divergence from the length between slits in the Allison meter  $L$  and the slit width. We can calculate the maximum path length between slits as  $L_{max} = \sqrt{L^2 + (w/2)^2}$ . This gives a divergence  $> 2000$  mrad, which is an order of magnitude greater than that measured in the y-axis. Without having directly measured the  $x$ -axis emittance we take this as an acceptably pessimistic estimate of the uncertainty and use it to assign a relative uncertainty to  $L_{eff}$  of 0.021. Direct measurements of the  $x$ -axis emittance were not pursued due to the  $x$ - $y$  symmetry of the CB, by which we would predict identical emittance in either transverse direction.

There were two primary considerations in the measurements of ion counts: the normalization discussed in the previous section and the consistency of beam current. The individual data points  $N$  were estimated to have an uncertainty of  $\sqrt{N}$ . Standard error propagation techniques were used to incorporate these uncertainties. The uncertainty in the average background counts was estimated as the standard deviation of the mean. To account for variations in the beam current, the current was measured over  $\approx 24$  hours to see how it shifted and was found to vary by less than 1% per hour.

An additional concern here is whether the distribution can be accurately described as Gaussian. Fitting the distribution to a Gaussian function it was found that it follows a Gaussian distribution well except for a small cut off observable in the upper right corner of the phase space distribution shown in Figure 3.6. The apparent cut-off of beam is equivalent to 2% of the total ion counts. This is likely due to the edge of the beam being cut at an aperture in the beamline. The most likely position for these ion losses is the hole in the B1 bender plate. In simulation (see Figure 3.7) it was found to be the most common cause of ion losses.

Together, the uncertainties in the emittance measurements resulted in uncertainties of approximately 1% on the measurements performed.

## Results and comparison to simulation

The key results for the beamline studies discussed here were from measuring the emittance from the CB under standard operating conditions. This result is plotted in Figure 3.6 d), which shows an rms emittance of  $13.24 \pm 0.09 \mu\text{m}$  with an inflation factor of 1.09 for a bunched beam of  $^{133}\text{Cs}^+$  ions at an energy of 2.4 keV. The ion current out of the CB was set to release single ion bunches. This is in agreement with previous measurements of the CB emittance described in Reference [63] which reports an emittance of  $4 \pm 1 \pi \text{ mm mrad}$  at a beam energy of 4 keV. Scaling this previous measurement to 2.4 keV we find it to be  $16 \pm 4 \mu\text{m}$ .

This measurement was reproduced in simulation with the same operating parameters and a temperature set at 300 K, the result of which is shown in Figure 3.7. We can see here that the experimentally measured best estimate emittance is approximately 1.7 larger than that simulated. This same difference was seen in comparing experimental results in Reference [63] to simulations in Reference [65] on which these simulations were based. This suggests that

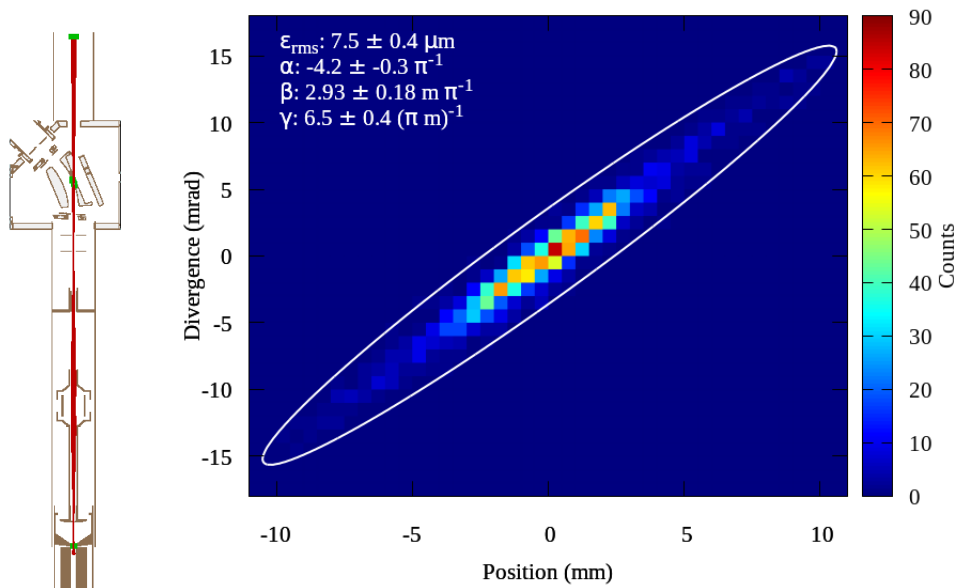


Figure 3.7: A simulation of the Allison meter emittance measurement of the TITAN CB beam shown in Figure 3.6. Left: SIMION simulation of ion trajectories (red) with collision points (green) and ion optical elements (brown). Right: Emittance plot with rms emittance, Twiss parameters, and the ellipse calculated from the Twiss parameters for equivalent emittance ( $4\epsilon_{rms}$ ) overlaid in white. For this simulation frequency was set at 480 kHz with a peak-to-peak voltage of 170 V, a gas pressure of  $10^{-2}$  mbar, and temperature of 300 K.

these CB simulations are consistently simulating the beam having a smaller phase space and thus being more cooled than what is achieved experimentally. A possible source of the larger experimental phase space is space charge effects within the CB. A significant portion of the ions cooled in the CB ( $\sim 10\%$ ) are lost before extraction. This means that when single ions are being extracted from the CB experimentally there may still be enough ions to inflate the phase space through Coulomb interactions. Such an effect is not currently being simulated. If the CB is to continue to be incorporated into future beamline simulations it may be necessary to use a more empirically defined initial phase space and extract ions immediately. Alternatively, the simulations of the cooling process may undergo further development to incorporate space charge effects.

### 3.1.3 Beam time profiles

One of the beam diagnostic devices permanently in the TITAN beamline is a set of MCPs whose locations are noted in Figure 3.1. MCPs are able to provide ion time-of-flight (ToF) data by recording how long after ejection from the CB ions are detected. MCPs are also sensitive to single-ion counts, useful for detecting low beam currents. The resulting beam time profiles have been used as a point of comparison between simulation and experiment.

To compare simulated and experimental time profiles, the experimentally chosen timing triggers and electrode voltages were used as input data into the simulation. Ions were created one at a time inside the CB, then cooled, then transported to the location of the relevant MCP where the ion position, velocity and ToF would be recorded for analysis. Two MCPs were used

for this comparison which we will refer to by TITAN nomenclature as MCP-0 (immediately before MPET), and MCP-1 (in the midpoint of the 90° bend section of the TITAN beamline), both shown in Figure 3.1.

Prior to transport through the TITAN beamline  $^{133}\text{Cs}^+$  ions were trapped in the TITAN CB with an RF frequency of 480 kHz, peak-to-peak voltage of 170 V, and helium buffer-gas pressure of approximately  $10^{-2}$  mbar. Voltages used on the electrostatic beamline elements are summarized in Appendix B. We note that the experimental voltages on the electrostatic ion optical elements appear to give a relatively high ion transmission in simulation without any modification as seen in Figure 3.9. Bender voltage differences of a few volts ( $< 1\%$ ) are sufficient to completely block transmission through TSYBL:DPA, thus suggesting that the electrostatic portion of the simulation provides a reliable model of the real beamline.

A comparison of experimental and simulated time profiles at MCP-1 and MCP-0 may be seen in Figure 3.8, including the results of Gaussian fits to the data. Figure 3.9 shows the simulated ion trajectories from the CB to MCP-0. The same settings were used for transporting beam to MCP-1 and MCP-0; thus the trajectories seen in Figure 3.9 would be the same in both cases. At both MCPs the simulated time of flight is approximately 4  $\mu\text{s}$  longer than in experiment and in both cases the Full Width at Half Maximum (FWHM) is larger. In the case of MCP-1 the simulated FWHM is 62% larger than in experiment and for MCP-0 the FWHM is 13% larger. These differences between simulation and experiment require some further discussion.

Examining the ion trajectories shown in Figure 3.9 we can see that there are multiple regions in the beamline where the beam passes very close to the ion optics, in some places colliding with electrodes. Since the experimental CB emittance is approximately 1.7 times larger than in simulation, this indicates that the probability of ions passing close to or colliding with electrodes is greater in the physical beamline. Experimentally, ion losses along the beamline have been detected by measuring radioactivity during online experiments. In particular, a large amount of ion loss was observed at the differential pumping aperture after the 90° bend (TSYBL:DPA), consistent with losses seen in simulation.

For the case of ions passing close to electrodes but not colliding, we expect a high sensitivity to fringe-field effects and misalignments. Close to the electrodes, small imperfections in the machining or alignment of electrodes will have a larger effect on ion trajectories. Similarly, the simulation of the electrodes and resulting electric fields has a finite resolution, which can also introduce field aberrations, particularly close to the electrodes. Over long distances the effects of sampling these field aberrations will become increasingly pronounced. This effect may be observed through an increase in rms emittance, though we could not expect this increase to be identical between simulation and experiment. In Figure 3.10 we can see in simulation this effect of the rms emittance growing as the beam travels through the beamline. A notable exception to this trend towards increasing emittance comes where the beam passes through TSYBL:DPA. A simulation of these ion losses is shown in Figure 3.11.

The large drop we see in the emittance after TSYBL:DPA results from the aperture acting as a collimator. TSYBL:DPA is 10 cm long with a 4 mm diameter which results in only a limited range of ion trace space properties being allowed to pass through. All other ions which would give the beam a larger emittance are removed. This beam collimation likely produces the closer agreement between simulation and experiment by removing many of the ions out of the CB which cause the experimental emittance to be larger than that simulated.

In Figure 3.9 we see that there are ion losses around the drift tube which sits at the location of MCP-1 when the MCP is not in the beamline. When MCP-1 is in the beamline it has a small 1.3 cm long section of drift tube before it which for a larger emittance beam may have some collimation effect. It is feasible that this is a factor in the smaller ToF FWHM measured

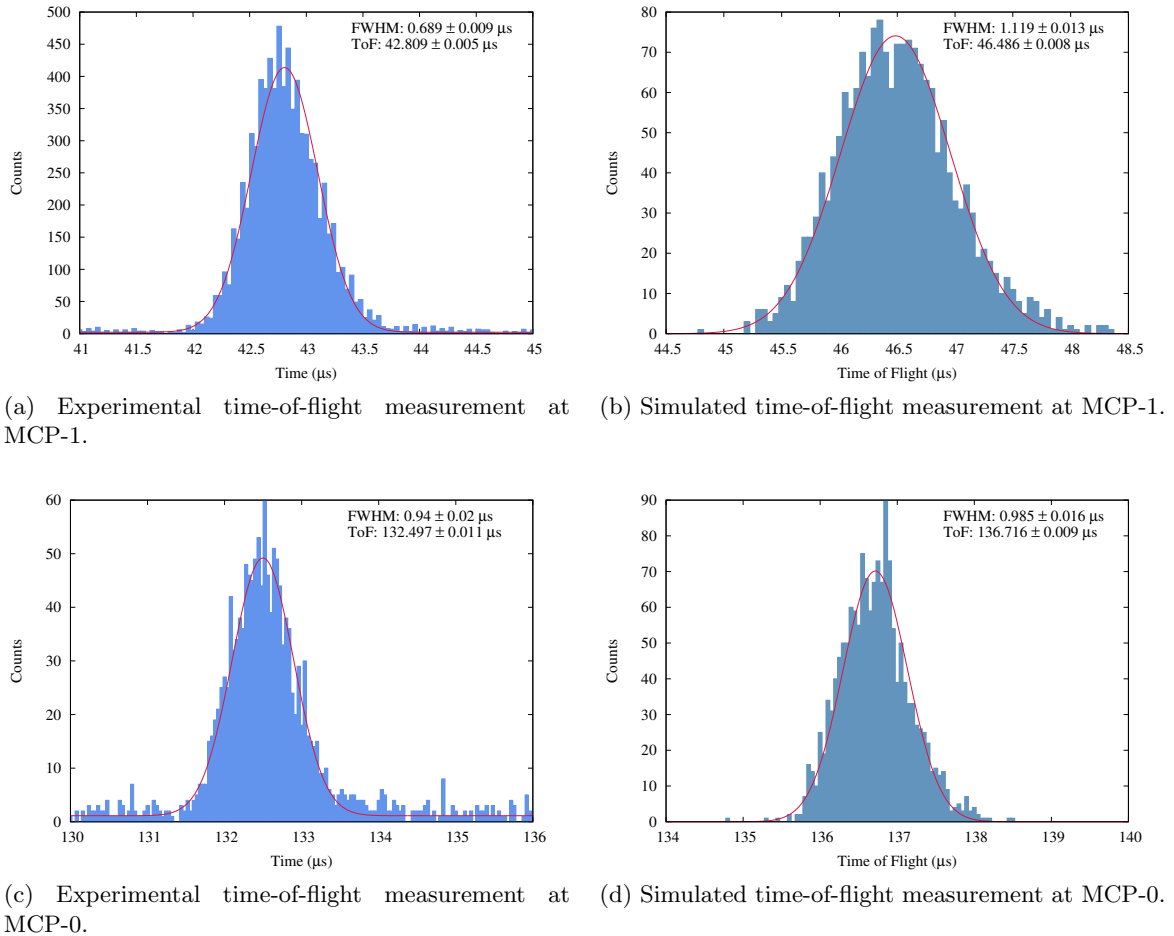


Figure 3.8: A comparison of simulated and experimental time-profiles obtained at MCP-1 (top) and MCP-0 (bottom).

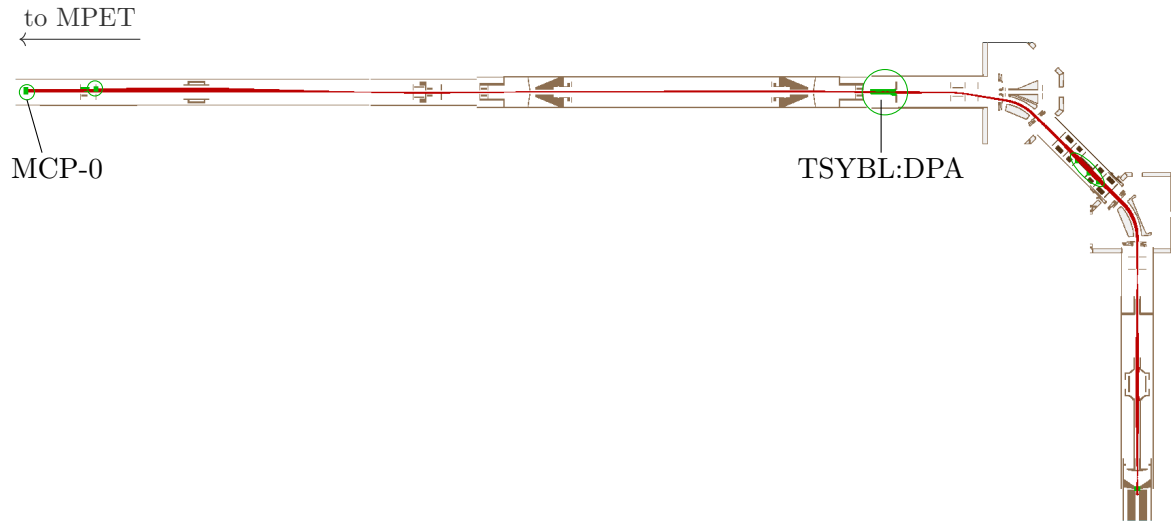


Figure 3.9: A SIMION simulation of the TITAN beamline between the CB and MPET. Beam trajectories are shown in red and points where ions collide with electrodes or reach the position of MCP-0 are marked in green with notable loss points circled in green. Most losses occur at TSYBL:DPA.

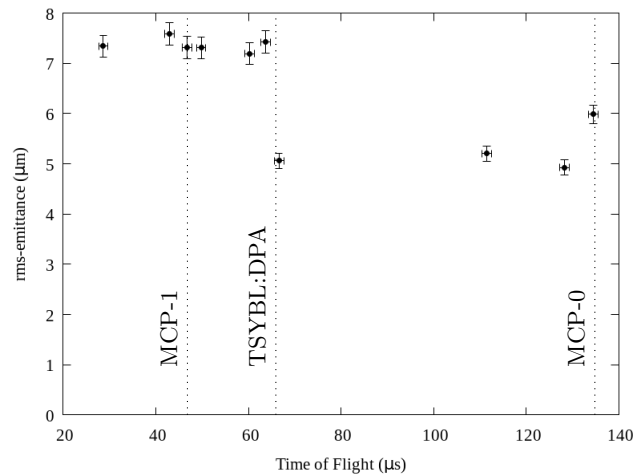


Figure 3.10: A plot of the change in transverse rms emittance as a function of beam time of flight from the CB.

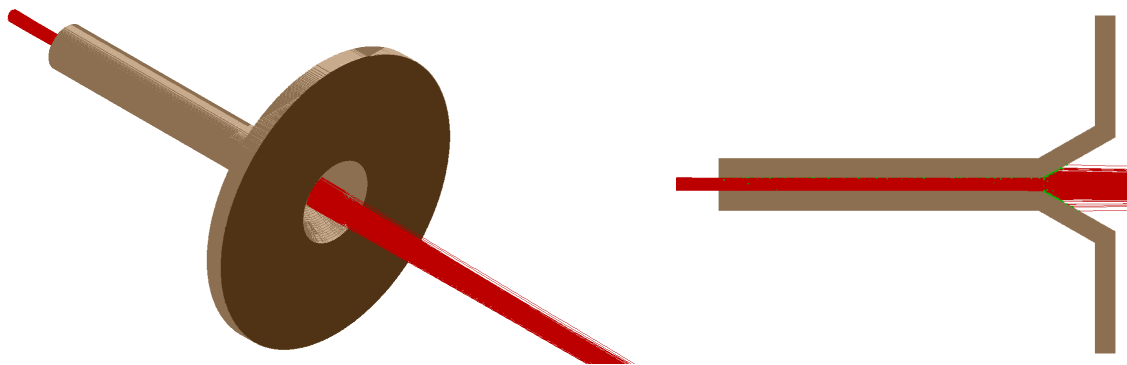


Figure 3.11: Simulated trajectories (red) of ions passing through the differential pumping aperture TSYBL:DPA, and the points at which some ions collide with the aperture structure (green). Trajectories are going right to left here. Simulations produced in SIMION [50].

experimentally.

We therefore conclude that these simulations can reproduce experimental measurements within a factor of 2. Inconsistencies appear to arise primarily from differences between the simulated and actual CB and the resulting sampling of fringe-field effects and ion losses as ions pass close to the beamline electrodes. Agreement between simulation and experiment appears to become closer for beam which has passed through TSYBL:DPA due to collimation effects from the aperture removing inconsistencies arising from limitations in the CB simulation.

A number of simulations were run to see if other effects could account for the disagreements between simulation and experiment, looking primarily at the output of the CB. Consideration was given to possible differences between experimental and simulated electrode voltages, and rise-times.

For voltages, the possibility that power supplies had not delivered the requested voltages to some CB electrodes was investigated. Simulations showed that to bring simulated ToF peaks into closer agreement (a few percent different), voltage differences would need to be increased by tens of volts. Such differences are much larger than anything which has been experimentally measured ( $< 1$  V), and thus this explanation was rejected.

No record was available of the electrode rise-time for switching the CB from cooling to extraction, only that it could be as long as  $10 \mu\text{s}$  [72]. Within this constraint simulations were run for a range of rise-times ranging from  $10 \text{ ns}$  to  $10 \mu\text{s}$ . Shorter rise-times can see decreases in the ToF ( $\sim 1 \mu\text{s}$ ) and ToF FWHM ( $\sim 100 \text{ ns}$ ) which bring simulation closer to experiment, but these effects were not sufficient to bring simulated ToF measurements into agreement with experiment. Thus, without any obvious indication that this might be the cause of the disagreement, adjustments in rise-time were set aside until such a time as it can be measured experimentally.

If a closer agreement between simulation and experiment is required for further beamline studies and development it may be necessary to apply a more empirical approach in simulating the beam. Using the measured transverse emittance and Twiss parameters it is possible to infer the transverse beam properties out of the CB using methods discussed in [47]. With measurements of the beam energy spread using an RFA, and ToF information from the MCPs an empirically derived longitudinal emittance could also be defined. Such an approach would however lose the freedom to easily simulate different cooling and extraction parameters in the CB. For this thesis there was not sufficient time to change to an empirically defined beam.

## 3.2 MR-ToF integration

Having developed simulations of the TITAN beamline we now turn our attention to the integration of the MR-ToF. The MR-ToF was designed to interface with the TITAN system at the 90° bend section indicated in Figure 3.1. This location allows beam from the CB to be injected into the MR-ToF transport system from below, undergo mass separation, then be ejected from the MR-ToF transport system towards MPET for high precision mass measurement, or to other experiments.

### 3.2.1 Beamline modification for MR-ToF

When the TITAN beamline was first designed the MR-ToF was not foreseen as part of the system [73][74]. Critically, there was no path for ions to enter the MR-ToF from the CB as the outer electrode of the B1 bender would be a barrier to passage. To allow ion transport through the B1 bender a new B1-OUT electrode was machined with a 7.9 mm diameter hole on the beam axis out of the CB to allow ion transmission. However, simulations of the beamline showed that the established TITAN optics were only able to provide 33% ion transmission at the beam energy the MR-ToF was designed to accept (1.4 keV). A key issue was that there were no focusing optics after the aperture TRFCBL:DPA and before the B1 bender. EL5 needed to focus beam on TRFCBL:DPA, resulting in a significant beam divergence and resulting ion losses at the position of the hole in B1-OUT.

To improve ion transmission it was necessary to introduce a new lens between TRFCBL:DPA and the B1 bender. An additional concern was beam steering to compensate for any possible beamline misalignments. Due to the limited space available between TRFCBL:DPA and B1 the decision was made to combine these steering and lensing properties into a single ion optic. This lens design was achieved by splitting the middle electrode of an Einzel lens into four quarters able to have independently set voltages providing simultaneous focusing and steering. We shall refer to this lens design as a split Einzel lens (SEL), photos of which are shown in Figure 3.12. The SEL was placed in the TITAN beamline in the location of the XCB0 benders.

Due to time constraints a quantitative analysis of the improvement to ion transmission afforded by the SEL was not possible. The SEL was installed amidst the process of measuring the beam energy with an RFA located above the B1 box. Prior to the SEL installation ion currents at the RFA were too low to be distinguished from background noise; however, after the SEL was installed, a very clear ion current was immediately detected, indicating a substantial gain in transport efficiency. This improvement in transmission is reflected by simulations which showed near 100% ion transmission into the MR-ToF upon introduction of the SEL (compared to the previous 33%).

### 3.2.2 MR-ToF acceptance

One component in the maximization of the beam transmission into the MR-ToF was an understanding of the MR-ToF acceptance. To investigate the acceptance of the MR-ToF, simulations were produced to examine the ion trace space properties which could enter the MR-ToF system input optics.

#### Acceptance simulation principles

The geometry of the input optics was reproduced in SIMION. Then ions were simulated as starting at the top of the B1 box and allowed to fly towards the input optics. Trace space



Figure 3.12: Photos of the split Einzel lens added to the TITAN beamline to facilitate high ion transport efficiency into the MR-ToF. Top: SEL prior to installation. Bottom: SEL installed in its location in the TITAN beamline.

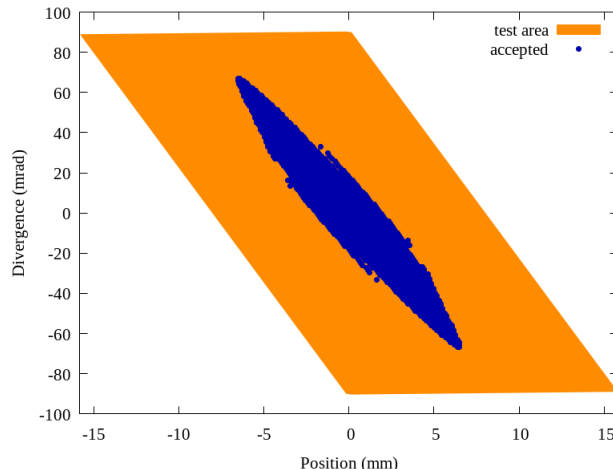


Figure 3.13: An example of the portion of trace-space tested (test area) and acceptance simulated in the investigation of the acceptance of the MR-ToF input optics.

properties of ions passed to the MR-ToF were defined in a rectangular grid  $2x_{max}$  wide by  $2x'_{max}$  high. Within these bounds,  $n_x$  initial  $x$  values and  $n_{x'}$   $x'$  values were defined, covering a total trace space area of  $4x_{max}x'_{max}$ , with a resolution of  $n_x \times n_{x'}$ . This rectangle could be rotated to match more closely the observed acceptance trace-space orientation (as in Figure 3.13) and limit the portion of trace space tested outside the acceptance, thereby reducing the number of ions which needed to be simulated in characterizing the device acceptance.

Having defined the portion of trace space to test, each ion with a set initial  $x$  and  $x'$  was flown towards the MR-ToF input optics. The initial properties of ions successfully entering the device were recorded to characterize the device acceptance. If it appeared the tested trace-space was too small to cover the device acceptance, the test area was increased until the total acceptance area was enclosed. An example of a chosen test area and acceptance are shown in Figure 3.13.

To numerically define the acceptance, each flown ion was assumed to represent a set fraction of the test trace space area,

$$\alpha_1 = \frac{4x_{max}x'_{max}}{n_x n_{x'}}. \quad (3.4)$$

From this we calculate the device acceptance  $\alpha$  from the number of accepted ions  $N_{accepted}$  as,

$$\alpha = N_{accepted} \cdot \alpha_1. \quad (3.5)$$

It should however be noted that this method of acceptance prediction should be considered an upper limit on the device acceptance. The acceptance may be filamented due to aberrations from ion optical elements, making it very difficult (though not impossible) to match beam emittance to. This consideration would be of particular importance in cases where the beam emittance is of a similar magnitude to the device acceptance.

### Application to MR-ToF acceptance

To study the MR-ToF acceptance it was important to look for optimal ion optical operating parameters to facilitate matching to the beam from the CB. A SolidWorks [75] model of the MR-ToF input optics is shown in Figure 3.14. The labels indicate the function of each ion

optical element. Some of the ion optical functions have been discussed in Chapter 2, specifically the Einzel lens (S-In-Lens), the contacts for the resistive RFQ rods (S-In-RFQBot and S-In-RFQTop), and the RFQ trapping segments (S-In-TrapS). Other electrostatic optics are: The steering electrodes (S-In-Steer1-4) which are individually controlled electrodes in a quadrupolar arrangement able to provide transverse beam steering. The deceleration stack, which is a set of four electrodes connected with a resistor chain where the bottom electrode is on ground and the top defined by the voltage S-In-DecTop. The deceleration stack is used to slow 1.4 keV beam to somewhere on the order of 10–100 eV. The apertures after the deceleration stack (S-In-A1–3) are a set of small apertures which restrict gas flow from the gas-filled RFQ section above while also allowing a small amount of electric field manipulation. For notational brevity in further discussion of the input optics we will neglect the “S-” prefix as it is present in all MR-ToF optics discussed in this chapter.

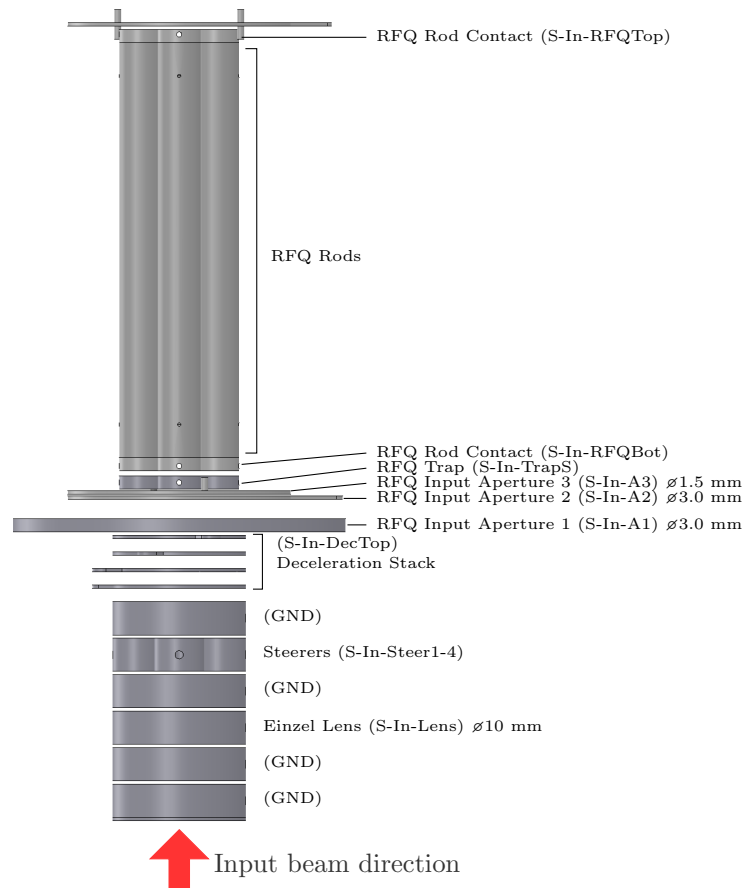


Figure 3.14: SolidWorks model of the MR-ToF input optics indicating the electrode nomenclature.

In defining the optimized operation parameters for the various electrodes in simulation there were a few necessary considerations. The deceleration stack was set using In-DecTop at 1380 V to reduce the beam energy to  $\approx 20$  eV before entering the RFQ. The DC voltages on the RFQ rods were set below that of the deceleration stack to guide the low energy ions in the desired direction. To this end, In-TrapS and In-RFQBot were given voltages of 1347.8 V and 1344.5 V respectively. In-RFQTop was set at the same voltage as In-RFQBot because we did

not need to simulate ion movement through the MR-ToF transport section, only ions entering the system, thus simulating the DC gradient in the RFQ section was unnecessary. Steerers were present to correct for any alignment issues. However, any misalignments in the physical device have not been reproduced in simulation, thus we set the steerers to ground. The apertures In-A2 and In-A3 were set at 1350 V to follow the choice of voltage used in offline testing of the MR-ToF. For In-A1 it was realized that by setting the voltage a few hundred volts lower than the neighbouring electrodes it can act as a small Einzel lens. The small length of the In-A1 aperture is still sufficient to have a noticeable effect due to the low energy of the ions passing through it. To examine the possible lensing effect of In-A1, a range of voltages were tested for simulating the MR-ToF acceptance. The final optical element which needed to have a voltage set was the In-Lens. A range of voltages were also examined for the In-Lens to determine an appropriate voltage for optimizing acceptance of the input optics.

Having identified two ion optical elements which we wish to examine more closely to simulate the MR-ToF acceptance we now look at some of the results. As mentioned above, ions were created in simulation at a location at the top of the B1 box with set trace space properties, then flown towards the MR-ToF. Ions which successfully entered the gas-filled RFQ section were counted as accepted by the device. Tests of the 2-dimensional parameter-space of the In-Lens and In-A1 voltages were performed to examine how they affect the MR-ToF acceptance. First a qualitative analysis was used to evaluate an appropriate range and step size for the voltages to be tested. It was decided to vary the In-Lens voltages from 0 to -2250 V in 150 V steps, In-A1 was varied from 200 to 1200 V in 200 V steps.

A sample of the results from varying the electrodes In-A1 and In-Lens is shown in Figure 3.15. First an observation can be made that all cases show that a converging beam would be optimal for matching beam emittance. For observations specific to particular optics, it was noted that changes in the In-Lens voltage had very little effect on the acceptance area, typically causing changes  $< 1\%$ . The effect of the In-Lens was primarily to change the focus point to which the beam is converging. This is reflected in changing trace space width and orientation of the acceptance. Variations of In-A1 had little effect on the focus point, instead increasing the width of beam which can be accepted, converging to a focus point set by In-Lens; this reflected by the linearly increasing acceptance coupled with a constant trace space orientation. The width of the trace space acceptance does not change noticeably with In-A1, meaning that it has little effect on improving acceptance of diverging beams.

Both measurements and simulations of the beam from the TITAN CB showed the beam emittance being much smaller than the acceptance values simulated here, but diverging. As a result, settings for In-A1 and In-Lens which allowed the largest portion of a divergent beam to be accepted was desired. It was believed that this could be best achieved with an In-A1 voltage of 800 V and an In-Lens voltage of -1050 V.

### Matching emittance to acceptance

Having investigated the MR-ToF acceptance, attention was then shifted to optimizing beam properties from the CB to match the MR-ToF acceptance. The available lenses for optimizing beam from the CB into the MR-ToF were EL5 and the new SEL. During normal operation EL5 would be set to focus on TRFCBL:DPA. However, at the time the MR-ToF was being integrated into the TITAN system, experiments were being done to test the effects of removing the narrow part of this aperture, meaning the voltage on EL5 could be changed much more freely. Thus a large degree of freedom was afforded to optimize EL5 and the SEL to maximize transmission into the MR-ToF.

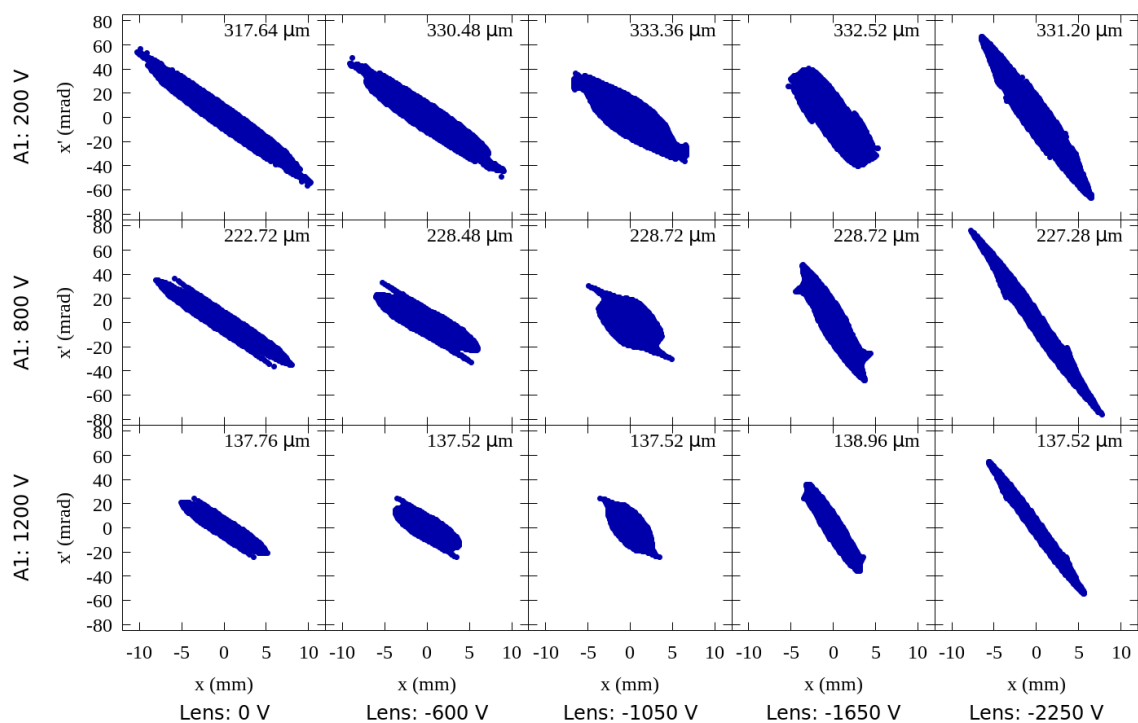


Figure 3.15: Samples of the acceptances simulated for the MR-ToF input optics across a range of chosen voltages. Numerical estimates of the acceptance are shown in the upper right corner of each plot. For this investigation the voltages on S-In-A1 and S-In-Lens were varied. Other voltage settings are indicated in the text.

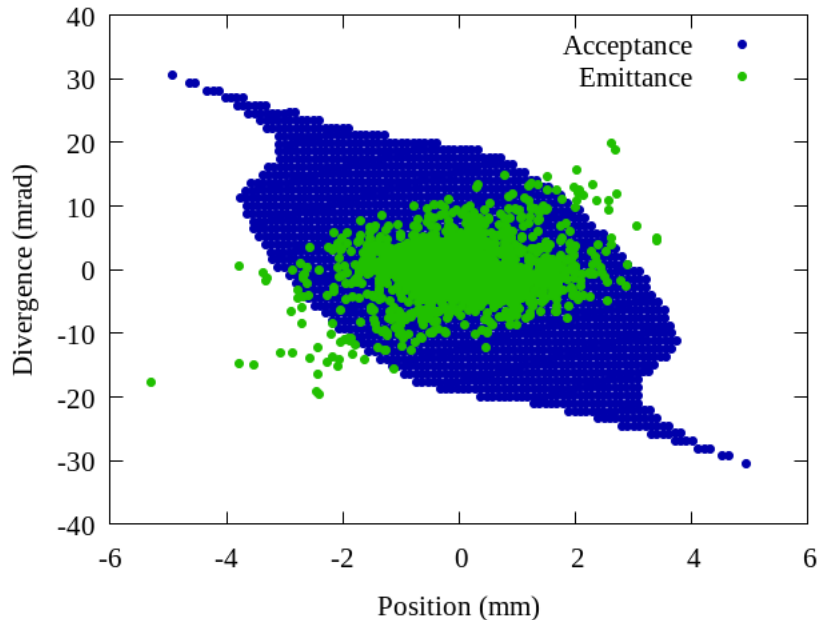


Figure 3.16: Simulated phase space of beam emittance (green) from the CB overlapped with the device acceptance (blue) of the MR-ToF input optics. This was achieved with EL5 set at -1650 V, SEL at -400 V, In-Lens at -1050 V and In-A1 at 800 V.

A range of voltage values were examined for EL5 and the SEL. For EL5, voltages from 0 V to -3600 V were tested and for the SEL, 0 to -3200 V. When a region in the resulting 2-dimensional parameter space was identified which provided high ion transmission, simulations were refined to a higher resolution in those areas. In the area of what appeared to be optimal parameters, voltages were adjusted in 50 V steps. The final result was an apparent optimal voltage of -1650 V on EL5 and -400 V on SEL for a beam energy of 1.4 keV. The Figure 3.16 shows an overlay of the simulated emittance over the simulated acceptance for these parameters.

When the MR-ToF was being commissioned with beam from ISAC these voltages were modified slightly, giving EL5 -1400 V and SEL -550 V. For the MR-ToF In-Lens was set to -1080 V and In-A1 was set to 250 V. This change was also accompanied by the decision to lower the voltage on In-DecTop to 1123 V, meaning a higher beam energy and lower emittance entering the gas-filled region of the MR-ToF input optics. Such a decrease in emittance makes it easier to maximize ion transmission into the MR-ToF. This difference in emittance would change the exact beam parameters which would allow matching beam emittance to device acceptance. Changing the operation of the MR-ToF input optics effectively used the input RFQ of the MR-ToF as a small CB, slowing the beam of a few hundred eV to a few eV for transport in the gas-filled transport section of the MR-ToF. In simulation this achieved an 84% transmission efficiency into the MR-ToF.

### 3.2.3 Beam profiles out of the MR-ToF

Having optimized beam transport into the MR-ToF the final step in interfacing the transport system of the MR-ToF to the rest of the TITAN beamline was to optimize beam transport out of the MR-ToF. A SolidWorks model of the MR-ToF output optics is shown in Figure 3.17. Ions were trapped in the region of the Out-TrapS electrode prior to ejection towards MPET.

Segments Out-A1 and Out-A2 were kept at a high potential prior to ejection from the trap, then pulsed to a low potential to eject ions from the trap. The beam energy was set by the voltage on Out-TrapS, for these simulations this was set to 1300 V to produce a 1.3 keV beam. The 1300 V potential is determined by the bias on the MR-ToF transport optics, used to achieve a 1.3 keV beam energy within the MR-ToF analyzer. A major constraint on possible ion optical settings was ensuring high transmission through TSYBL:DPA. As discussed above, this aperture has a small acceptance, greatly restricting the portion of ion trace space which can be transmitted.

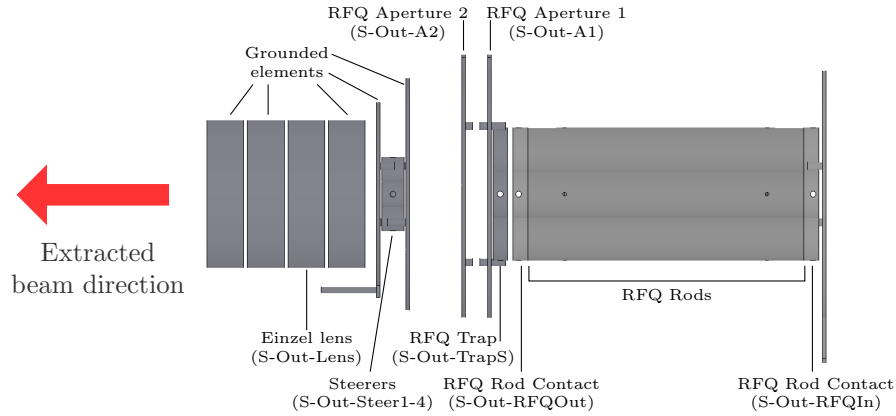
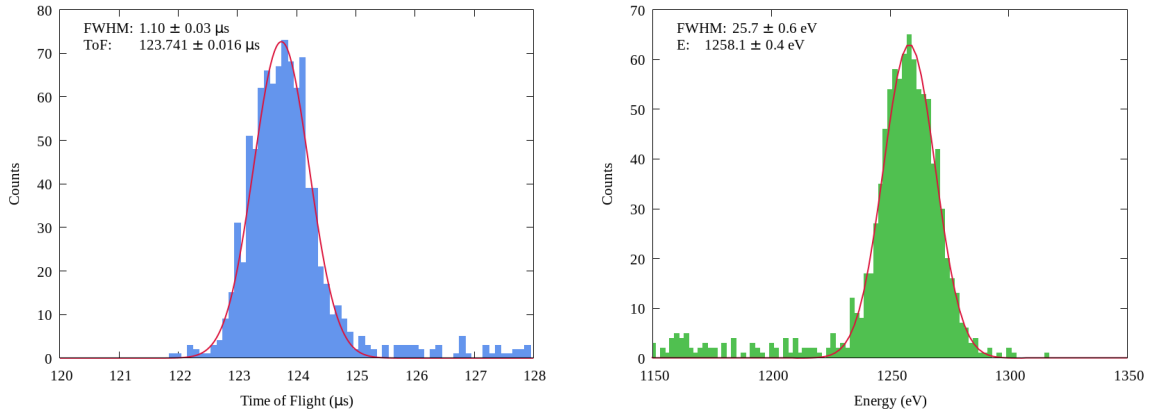


Figure 3.17: SolidWorks model of the MR-ToF output optics indicating electrode nomenclature.

The main lenses available for focusing beam from the MR-ToF through this differential pumping aperture are Out-Lens and B4-OUT. The B4 bender is built to allow beam to pass through from three different directions. For ions ejected from the MR-ToF, the central bore of the B4 bender may be used as an Einzel lens. In simulations the B4 bender was given an accelerating potential to achieve this Einzel lens functionality. It was found in simulation that transmission through the pumping aperture could be maximized by setting Out-Lens to -1900 V and B4-OUT to -1225 V.

Investigations of the extraction voltages on Out-A1 and Out-A2 suggested that Out-A1 should be set at -1100 V and Out-A2 somewhere at 1000 V. Figure 3.18 shows the corresponding beam ToF and energy plots at the position of MCP-0.. The spread in ToF appears consistent with what is achieved with beam from the TITAN CB, however the energy spread is much larger at around 25 eV.

The large energy spread merits further optimization which was not achievable with the settings on ion optical elements tested here. This investigation could be further expanded by varying the trap depth in the output RFQ prior to ejection to attempt to reduce the longitudinal emittance. It should also be possible to pulse the voltage on Out-RFQOut to introduce an added degree of freedom to optimize the longitudinal ion trace space distribution. We see in the simulated longitudinal emittance shown in Figure 3.19 that the trace space distribution is very long and narrow. This leads to either a wide ToF distribution, energy distribution, or both. For the investigation done thus far, this appears to have been the best achievable distribution. However, by introducing the aforementioned additional degrees of freedom to our beam optimization we may be able to achieve a wider, shorter trace space distribution. Such a distribution would enable a smaller spread in both ToF and energy.



(a) Simulated time-of-flight measurement at MCP-0. (b) Simulated energy measurement at MCP-0.

Figure 3.18: Simulations of, Left: expected time-of-flight peak (blue) and, Right: energy spread (green) from the MR-ToF output optics detected at the position of MCP-0 for a beam energy of 1.3 keV. Gaussian fits of the data are shown with key results on each plot. Results with Out-Lens at -1900V, B4-OUT at 1225 V, Out-A1 at 1100 V and Out-A2 at 1000 V.

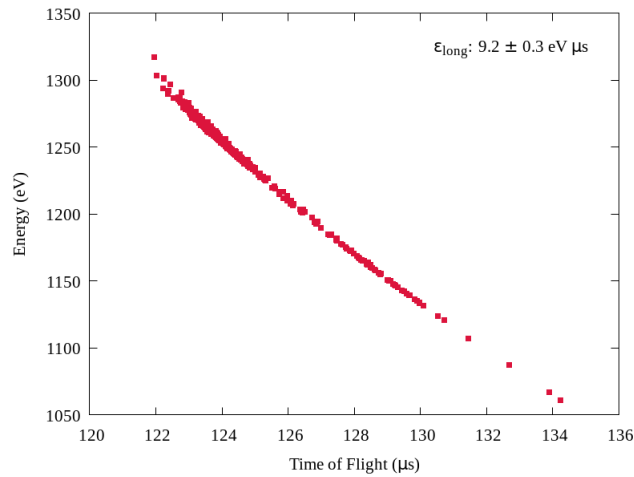


Figure 3.19: Simulated longitudinal emittance of beam ejected from the MR-ToF and detected at MCP-0 for a beam energy of 1.3 keV. This for the ion optical settings: Out-Lens at -1900V, B4-OUT at 1225 V, Out-A1 at 1100 V and Out-A2 at 1000 V.

### 3.2.4 Bypassing the MR-ToF

One final concern with the integration of the MR-ToF into the TITAN beamline was to ensure that measurements can still be performed using EBIT and MPET when bypassing the MR-ToF. For isolation of the MR-ToF vacuum a gate valve was installed before the MR-ToF input optics and after the output optics (along the beam path). In terms of ions optics, the only changes in the previously existing TITAN beamline was the introduction of the opening in the B1-OUT bender plate and the replacement of XCB0 with the SEL. Naively we would expect these to have a minimal impact on the beam through this section. The opening in B1-OUT is small (roughly an order of magnitude smaller than the bender radius), leaving most of the existing structure in place to provide the intended bending and focusing. Replacing XCB0 with the SEL should provide the same steering capacity while also introducing steering in the  $y$ -direction and additional focusing. However, to be thorough, this naive expectation was tested with simulations.

The section of beamline from the CB to just before TSYBL:DPA was simulated to evaluate the impact of the new optics for the MR-ToF integration. Simulations were done of  $^{133}\text{Cs}$  ions passing through this section at 2 keV without, and with the new optics. This beam energy is typical of operation of MPET and EBIT without the MR-ToF. For these simulations, no potential was put on the SEL so as to allow a more direct comparison between the two setups. Transverse emittance was simulated in these two situations and the results are overlaid in Figure 3.20. Numerically the rms emittance in the two cases agree within uncertainty, indicating that we should expect the same transmission efficiency to be achievable with the introduction of the SEL. Initial tests bypassing the MR-ToF to move ions directly into MPET support this conclusion.

We also note that the additional focusing of the lens and  $y$ -direction steering provide new degrees of freedom to improve ion transmission further. At present tests have not yet been performed to optimize ion optical parameters to maximize transmission using the SEL.

## 3.3 Summary

Through this chapter we have examined the transport of ions into and out of the MR-ToF as well as bypassing the MR-ToF. To accomplish this study, simulations were made in SIMION of the TITAN beamline from the CB to the MR-ToF or to MPET.

The simulations of the CB were validated through comparison of previous simulations, reproducing results reported in [65] within 35% or less. The cooler buncher simulations were also compared to measurements made with an Allison meter in the position where the MR-ToF is located. The cooler buncher simulations predicted an emittance of  $7.5 \pm 0.2 \mu\text{m}$  compared to the measured emittance of  $13.24 \pm 0.09 \mu\text{m}$ , giving a measured to simulated emittance ratio of 1.7. This same ratio was observed through cooler buncher simulations described in [65] and measurements described in [63].

Further comparisons of simulations to experiments were performed through measuring the beam time profiles at two MCPs in the TITAN beamline. At the first MCP the ToF FWHM was found to be 62% larger in simulation than experimentally, whereas at the later MCP there was a 13% disagreement. This difference was likely due to the beam passing close to, and sometimes colliding with, the edges of the beamline electrodes. This difference would be made greater by the difference between simulated and experimental beam emittance. The closer agreement is likely achieved by the collimation effect of the aperture TSYBL:DPA (shown in Figure 3.1).

Use of experimental electrostatic ion optical parameters in simulation produces high ion

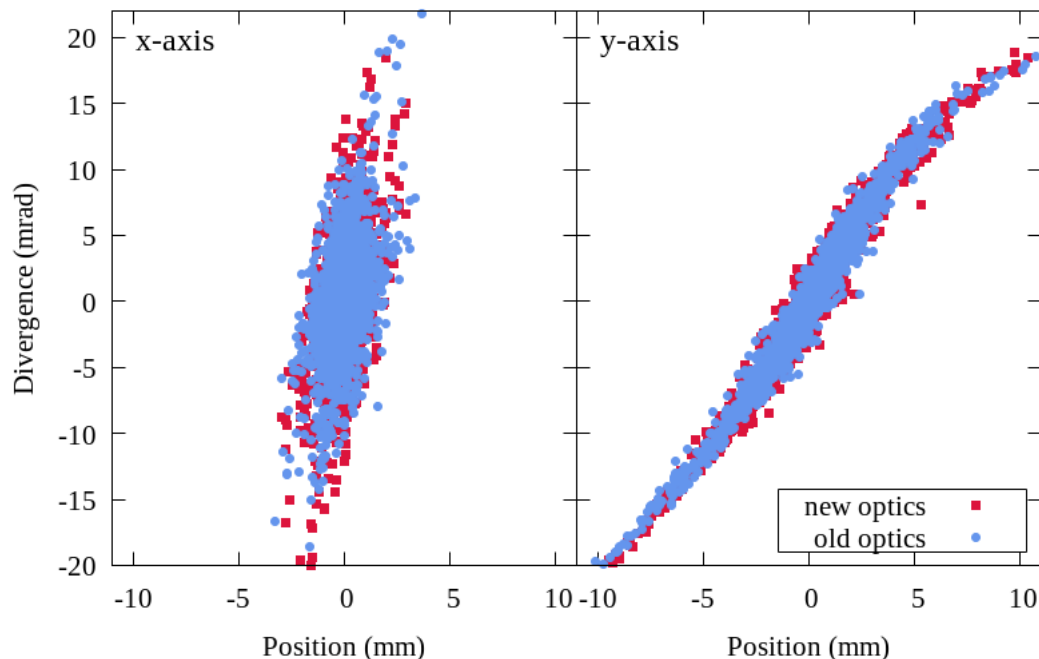


Figure 3.20: A comparison of transverse emittance simulated after the  $90^\circ$  bend in the TITAN beamline and before TSYBL:DPA without and with the new optics for ion transmission into the MR-ToF.

transmission in simulation. This transmission requires ions pass to through TSYBL:DPA for which differences in bender voltages of a few volts can completely stop ion transmission. Thus the electrostatic portion of the simulation appears to reflect experiment well.

For future use, the choice will need to be made between defining the initial phase space of the ion beam passing through the beamline using the CB simulation or empirically defined properties. The CB simulation allows users to explore effects of different cooling and extraction properties, but tests have shown it not able to reliably predict experimental results better than within a factor of 2. Using experimental measurements of the beam it is possible to empirically define initial beam properties in simulations, but this will be limited to simulating the beam as it was produced by the CB at the time of measurement.

Acceptance of the MR-ToF input optics was examined and a set of suggested optic voltages were determined which provided near 100% ion transmission into the MR-ToF in simulation. These voltages provided a basis for those chosen in experiment, for which similar settings were found to allow successful ion transport into the MR-ToF.

Simulations were done of the beam ejected from the MR-ToF towards MPET to determine optimal electrode voltages. Suggested settings were determined to optimize beam transport efficiency and quality, measurements of isobar separated beam in MPET and EBIT. Experimental verification is pending. Additional ion optical elements are suggested to provide more degrees of freedom for further optimization of MR-ToF output.

Additionally, the impact of implementing a split Einzel lens in the TITAN beamline and an aperture in the B1-out electrode was examined. Simulations showed the rms emittance before and after the introduction of these optics to agree within uncertainty. This indicates that we can expect the same ion transmission towards MPET and EBIT to be achievable while bypassing the MR-ToF as was the case before the addition of the MR-ToF. The lack of impact

### 3.3. Summary

---

on ion transmission is reflected experimentally. The addition of the SEL also introduces degrees of freedom for further improvement to ion transmission when bypassing the MR-ToF.

With this examination of the TITAN beamline and the interface of the MR-ToF with the TITAN beamline, we may now turn our attention to the first online tests of the MR-ToF itself to see how it has performed as a part of TITAN.

## Chapter 4

# First tests of MR-ToF integrated into TITAN

The MR-TOF was designed and assembled at the University of Giessen. It was shipped to TRIUMF and set up in an off-line testing area in the ISAC-I experimental hall. The device was tested and characterized with an additional ion source [44]. In parallel, the simulations and optics discussed in the previous chapter were prepared. Following the off-line preparation and installation of the additional ion optical elements, the MR-ToF was installed in the TITAN beamline (shown in Figure 4.1).

First a pair of gate valves were added to the TITAN beamline at the points of entry to and extraction from the MR-TOF as was the steering Einzel lens. These can be seen in Figure 4.2. The MR-TOF was installed, then optically aligned vertically with the cooler buncher and horizontally with the measurement Penning trap. A new high-voltage cage, its 3 kV transformer, and the electrical system were installed. The complete installed MR-TOF system is shown in Figure 4.3.

For operation, the control and data acquisition systems had been developed in Giessen and shipped with the device. The control system relied on a software called VCNew, a C-based computer code, which allows one to remotely control the optics and vacuum system. The data acquisition system, Massdata-Acquisition (MAc) [76], includes the timing generator, records signals from either an Analog-to-Digital Converter (ADC) or Time-to-Digital Converter (TDC), displays the data in real time, and allows for a simplified on-line analysis. The ADC is preferred for high count rates as it measures average MCP current rather than individual ions, leading to zero dead time. The TDC is favoured for low count rates ( $\ll 1$  ion/ns) as it allows the background from the detector to be excluded.

For this commissioning test, the ISAC OffLine Ion Source (OLIS) [77] was used to produce a beam of stable ions for testing the MR-TOF. This provided a reliable source of ions with a well known mass for benchmark purposes. These measurements were intended to demonstrate transport of externally produced beam into the MR-TOF, to estimate transport efficiencies, to perform a mass measurement, and to verify the resolving power. The expected performance parameters for the MR-ToF prior to construction were that it would achieve  $R \geq 20\,000$  for isobar separation and  $R \geq 100\,000$  for mass measurements within 10 ms and with a transport efficiency  $\geq 20\%$ . These tests and their results are described here.

### 4.1 Tests of MR-ToF with OLIS beam

A beam of  $^{40}\text{Ar}^+$  was produced in OLIS using the microwave source [78] which produces ions through a microwave discharge plasma. Also ionized are residual gases such as  $\text{N}_2$ . The beam was delivered at 20 keV to the TITAN cooler buncher (CB). It was then transported to the MR-ToF device at an energy of 1.4 keV. When an isobaric doublet was required,  $^{40}\text{K}^+$  was ionized in the MR-ToF ion source and merged with the OLIS beam in the MR-ToF switchyard. The

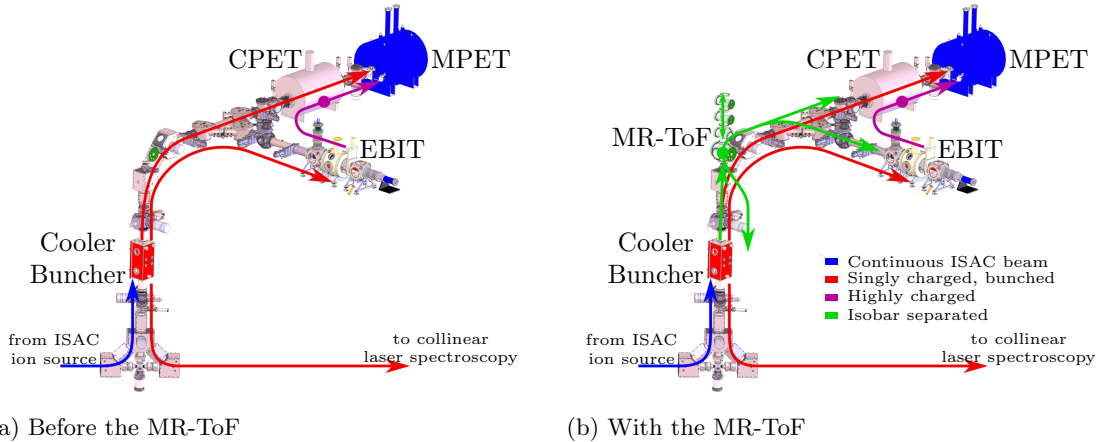


Figure 4.1: A schematic overview of the TITAN experiment a) before the MR-ToF and b) with the MR-ToF installed. Arrowed lines are used to indicate paths the ion beam may take to TITAN from the ISAC ion sources, inside TITAN, or from TITAN to the ISAC collinear laser spectroscopy experiment.

combined beam was then separated and measured in the analyzer. This allowed the performance of the MR-ToF using beam from ISAC as in online experiments to be studied. The purpose was to measure the device efficiency, to perform mass spectrometry, and to demonstrate the separation of the  $^{40}\text{Ar}^+$  and  $^{40}\text{K}^+$  isobars.

#### 4.1.1 Ion transport efficiency

The MR-ToF efficiency was estimated by comparing ion detections on MCPs, one located upstream of the buffer-gas-filled RFQ ion guides and another downstream of the analyzer section. Fluctuations of the ion source varied the count rate up to 30%. Multiple measurements were performed at different microchannel plate (MCP) bias voltages to ensure that the maximum detection efficiency was achieved and for a different number of turns in the analyzer. When the beam was transported directly through the analyzer section, that is without any reflections, the efficiency was 10.08(15)%. This is lower than the expected 20%, however we expect that greater efficiencies could be achieved when measuring isotopes of elements with a higher ionization energy than argon. This is because ions of elements with higher ionization energies have a larger probability of undergoing charge exchange when interacting with residual impurities in the helium buffer gas. As the number of turns was increased inside of the analyzer, the efficiency decreased due to collisions with residual gases from 10.08(15)% to 1.31(5)% for 600 turns at maximum resolving power. This loss in efficiency over longer flight times can most likely be improved by reducing the pressure within the analyzer. Expectations are that a pressure of  $\sim 10^{-8}$  mbar is a critical pressure at which this loss in efficiency with flight time mostly disappears [54].

#### 4.1.2 Mass measurement

To demonstrate the mass measurement capability of the MR-ToF with ISAC beam measurements were performed operating the MR-ToF at a rate of 50 Hz, taking  $^{40}\text{Ar}^+$  ions at a rate  $\leq 20$  ions/second. This was a sufficiently low rate to record the ion detections with the

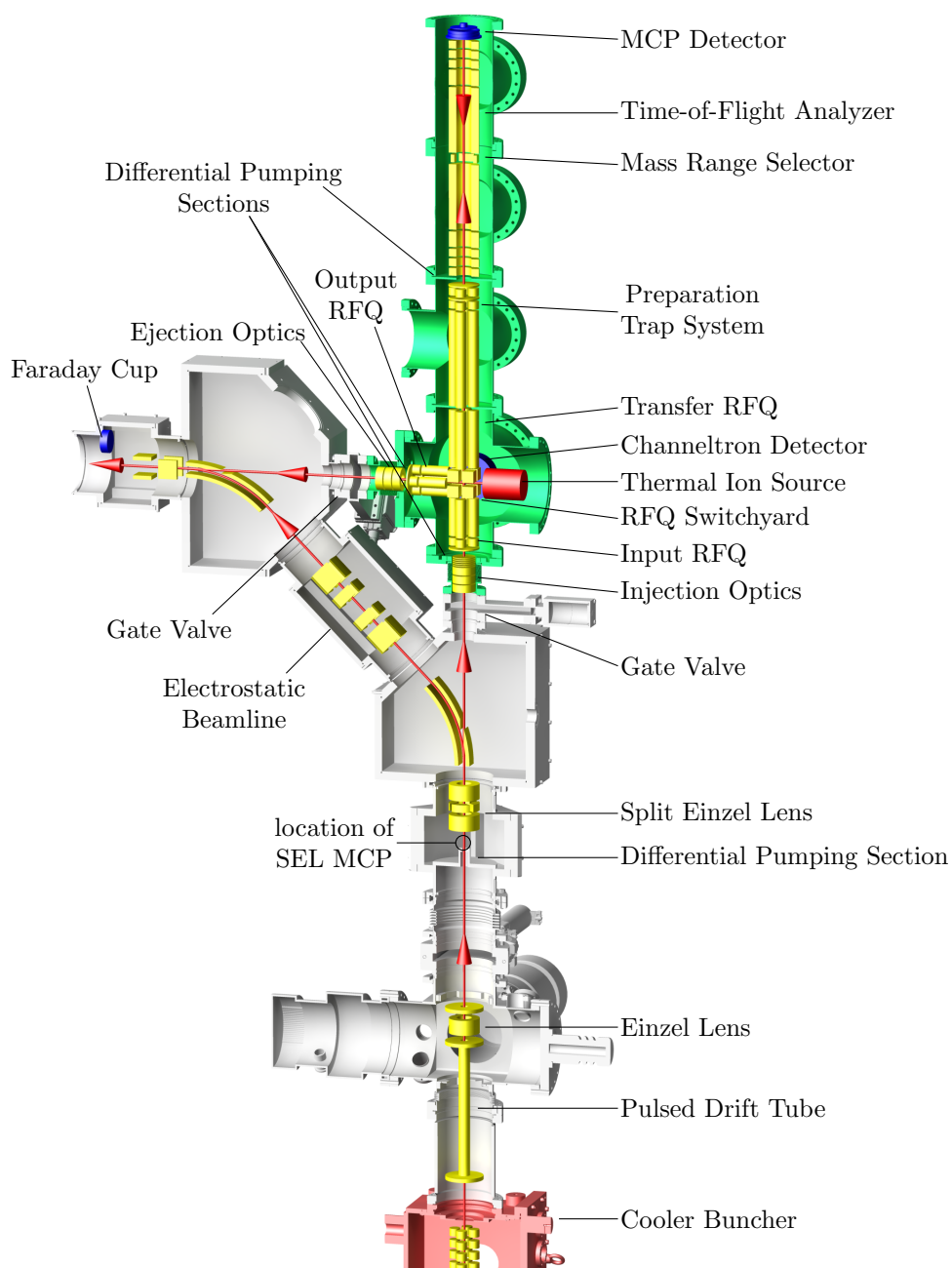


Figure 4.2: Schematic of the MR-ToF and its interface with the TITAN beamline. Ion optical electrodes are indicated in yellow; the MR-ToF vacuum chamber is highlighted in green; detectors are shown in blue; red arrowed lines are used to indicate possible beam paths through the TITAN beamline and MR-ToF.

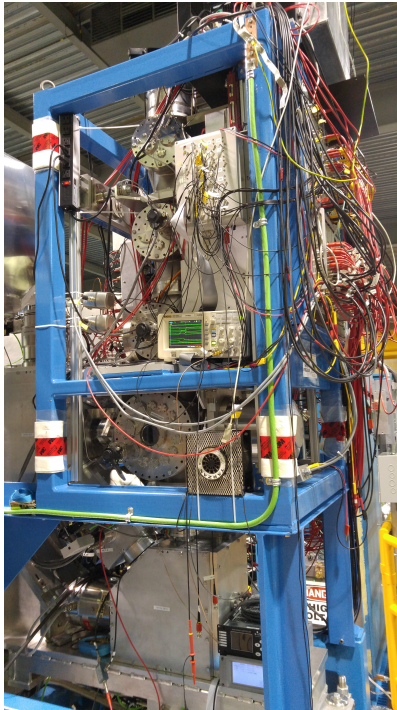


Figure 4.3: Photo of the MR-ToF installed and connected to the TITAN beamline.

TDC, meaning measurements were sensitive to single ion events. A series of mass measurements were performed around mass  $A = 40$ , first using the MR-ToF internal ion source to produce K isotopes  $^{39}\text{K}^+$  and  $^{41}\text{K}^+$  for calibration. After calibration, mass measurements were performed at increasing ion flight times to demonstrate the ability of the MR-ToF to identify a wide range of ions, accurately determine their masses, and resolve isobars at a resolving power greater than 100 000.

For all mass measurements discussed here time-of-flight (ToF) peaks have been fit with Lorentz functions to determine the peak FWHM  $\Delta t$  and average ion time of flight measured at the MR-ToF MCP  $t$ . The full ToF is determined as a combination of the delay after which ToF data starts to be recorded  $t_s$  and a constant signal delay caused by the electronics and transit time through the cables  $t_0$ . From these we determined,

$$\text{ToF} = t + t_s + t_0. \quad (4.1)$$

With the above we could calculate the mass resolving power as,

$$R = \frac{\text{ToF}}{2\Delta t}. \quad (4.2)$$

### Mass calibration

In order to ensure ion identification and mass measurement it is necessary to calibrate the conversion of ToF to mass using known masses. For this purpose, potassium from the MR-ToF internal ion source was used as a calibrant ion, for which a spectrum is shown in Figure 4.4. In the figure we see ToF peaks for  $^{39}\text{K}^+$  and  $^{41}\text{K}^+$ .  $^{40}\text{K}^+$  is not visible due to its low isotopic abundance (0.012%). Using these isotopes with known masses a calibration could be defined

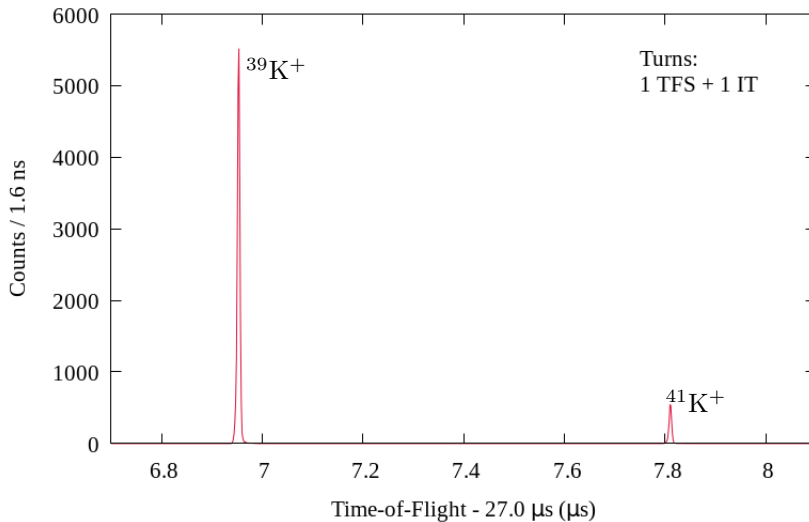


Figure 4.4: Time-of-flight spectrum of potassium isotopes used to calibrate the MR-ToF mass measurements.

Table 4.1: Literature masses [79] for isotopes of K and Ar used for calibration and comparison.

Isotope	Mass (u)
$^{39}\text{K}$	38.963706487(5)
$^{40}\text{K}$	39.96399817(6)
$^{41}\text{K}$	40.961825258(4)
$^{40}\text{Ar}$	39.9623831238(24)

as,

$$m = C (t - t_s - t_0)^2. \quad (4.3)$$

Here  $C$  is a calibration factor and  $m$  is the resulting calculated mass.  $t_s$  is calculated from the chosen timing signals, but  $C$  and  $t_0$  must be calculated using two or more known masses.  $C$  needs to be determined for each ToF spectrum, but  $t_0$  can be assumed constant as no cables and electronics have been changed between measurements. A fit was done of the  $^{39}\text{K}^+$  and  $^{41}\text{K}^+$  peaks shown in the spectrum in Figure 4.4 to determine the corresponding ToF data. The masses of these isotopes and corresponding uncertainties are found in [79] and shown in Table 4.1. Previous measurements of variations in  $t_s$  have shown it to have an uncertainty  $\sim 100$  ps [54]. The uncertainty in  $t$  was determined as the fit uncertainty of the mean ToF peak value. Thus using the available fit and mass data we calculate a value for  $t_0$  of  $126.1 \pm 2.4$  ns.

### High resolution mass measurement

Figure 4.5 shows a set of mass measurements performed in the MR-ToF ranging from a short to long ion flight times and the corresponding increase in resolving power. In these examples we refer to the process of an ion being reflected by both electrostatic mirrors and returning to an arbitrary start position as a “turn” in the analyzer. For each spectrum the ions went through one time focus shift (TFS) turn to set a constant time focus. After the TFS turn, the ions undergo a number of isochronous turns (IT) to provide the ToF by which the ion masses

Table 4.2: Comparison of the measured mass of  $^{40}\text{K}^+$  to the literature mass reported in Reference [79].

ToF (ms)	$^{40}\text{K}^+$ Mass		Relative Difference
	Measured	Literature	
7.4721(6)	39.964012(36)	39.963998166(6)	$4 \times 10^{-7}$

are resolved and measured.

The first spectrum in Figure 4.5 (1 IT) shows a broadband mass measurement performed with the MR-ToF using a short ToF. We see the  $^{40}\text{Ar}^+$  ions from OLIS along with molecules of  $\text{ArH}^+$  and a number of contaminant organic molecules. The dominant source of the contaminants is impurities introduced with the helium buffer gas which are ionized during MR-ToF operation. Increasing the number of IT and thereby the flight time we see the mass resolution increasing. In the 600 IT spectrum the MR-ToF internal ion source had been turned on to add  $^{40}\text{K}^+$  to the beam, demonstrating the capacity of the MR-ToF to resolve isobars.

Ions identified in Figure 4.5 were determined based on their mass calculated using the previously found  $t_0$  and calibrating  $C$  for each spectrum using the  $^{40}\text{Ar}^+$  peak. The results of the mass measurement of  $^{40}\text{K}^+$  in the 600 IT spectrum is shown in Table 4.2. This mass measurement agrees with the literature value within uncertainty [79], with a relative difference of  $4 \times 10^{-7}$ . Here a resolving power of 202 000 has been achieved, which is consistent with results seen during offline commissioning of the MR-ToF [44] as well as exceeding the expected performance by a factor of 2.

### 4.1.3 Isobar separation

The final functionality of the MR-ToF which needed to be tested was its capacity to remove isobaric contaminants from the ion beam through dynamic recapture in the preparation trap, which we call re-trapping here. Again a combination of  $^{40}\text{Ar}^+$  from OLIS and  $^{40}\text{K}^+$  from the MR-ToF internal ion source were delivered into the MR-ToF analyzer. The ions underwent 1 TFS and 256 IT before being ejected from the analyzer for re-trapping. After re-trapping a mass measurement would be performed in the analyzer to see the degree to which isobaric contaminants were removed.

To determine an optimal time to re-trap either  $^{40}\text{Ar}^+$  or  $^{40}\text{K}^+$  a range of re-trapping times were tested from 3212.68 to 3212.88  $\mu\text{s}$ . This allowed us to determine the re-trapping time where the contaminant isobar is completely removed while still leaving the largest possible amount of the ion of interest. For each re-trapping time the absolute number of ions counted by the TDC in each mass peak after 2 minutes was recorded, the results of this are shown in Figure 4.6 a. We can clearly see how changing the re-trapping time allows removal of one mass or the other. Figure 4.6 b shows an overlay of three mass measurement spectra, first with no re-trapping, then with specific re-trapping times to isolate either  $^{40}\text{Ar}^+$  or  $^{40}\text{K}^+$ . This demonstrates that either of these isobars can be successfully removed from the beam, providing at minimum a resolving power of 25 000, exceeding the expected performance of 20 000.

### Re-trapping efficiency

For this example of re-trapping, around 20% of the ions were successfully re-trapped as compared to a maximum of 35% achieved with ionized caffeine molecules in [42]. This efficiency will however vary with ion mass and the depth of the potential well used for re-trapping. In

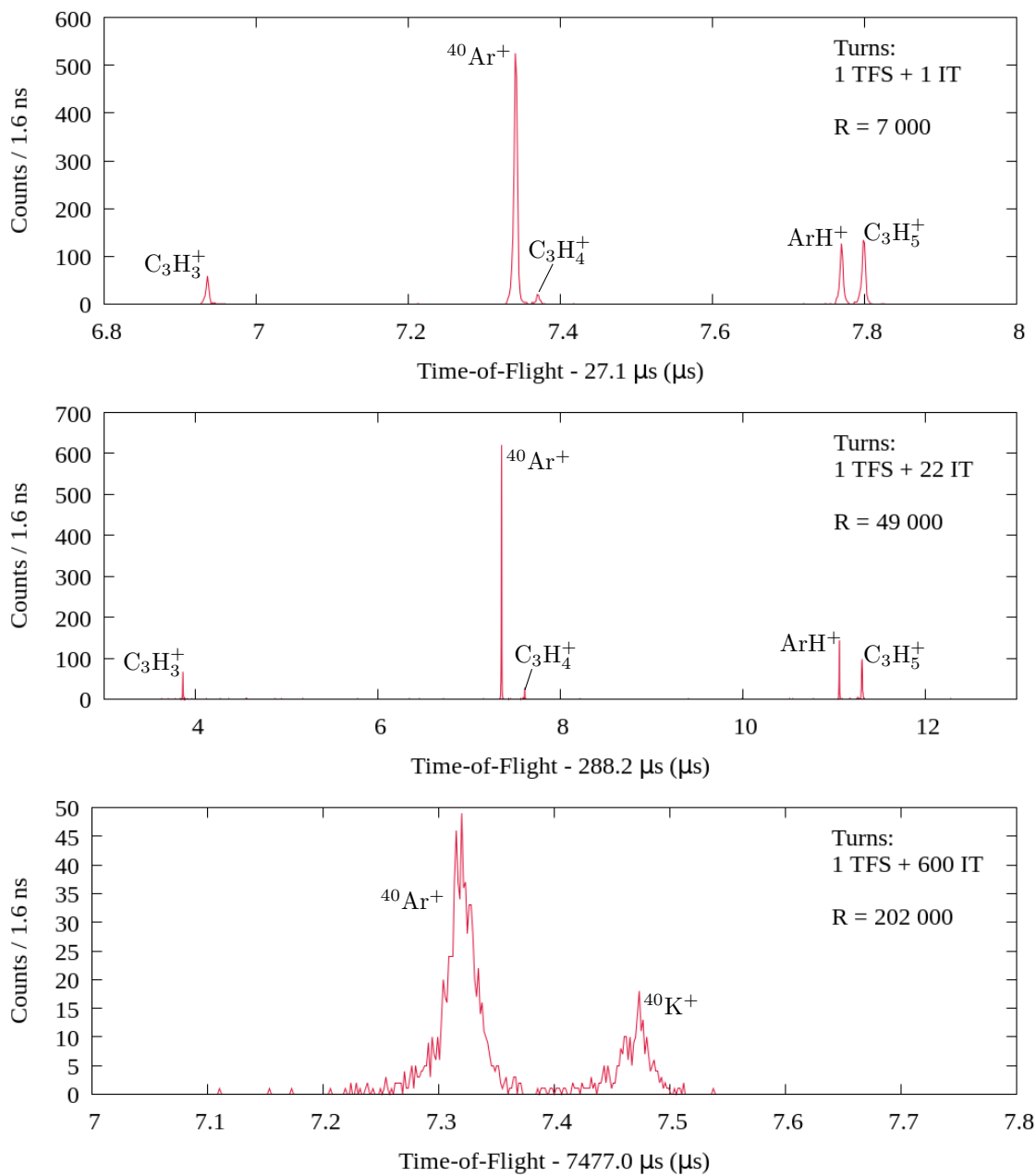
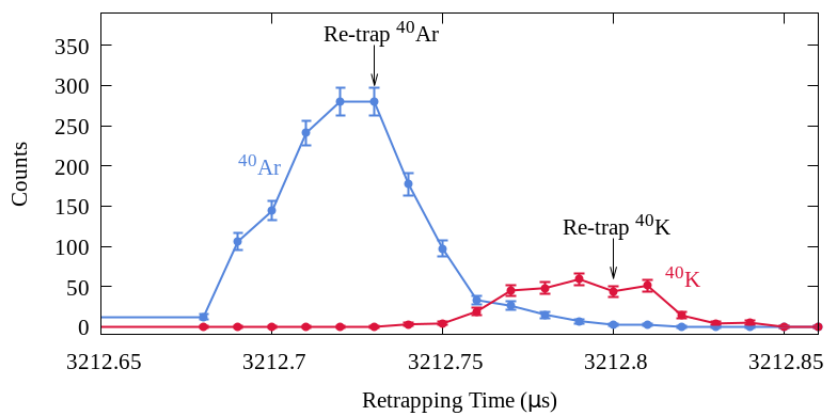
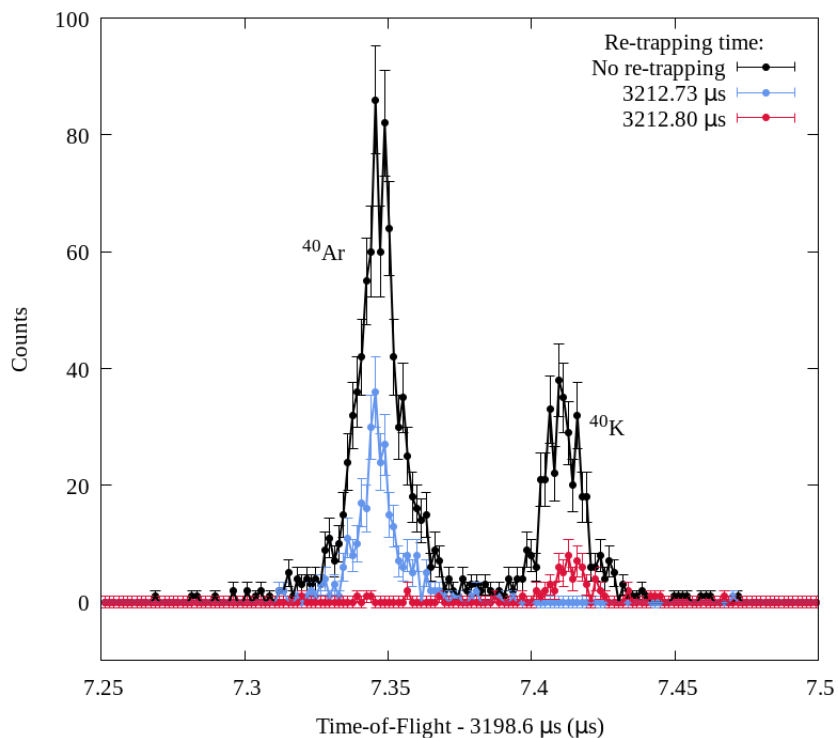


Figure 4.5: Three MR-ToF time-of-flight spectra used for mass measurements. Detected ions are marked in the plots; these ions were identified based on their mass. Time-of-flight mass measurements for each spectrum were calibrated use the  $^{40}\text{Ar}^+$  peak. For the bottom spectrum  $^{40}\text{K}^+$  was added to the beam using the MR-ToF internal ion source.



(a) Testing re-trapping times.



(b) Time-of-flight spectra after re-trapping.

Figure 4.6: An example of mass-selective re-trapping performed in the TITAN MR-ToF using  $^{40}\text{Ar}^+$  and  $^{40}\text{K}^+$  ions. a) Number of ions detected for  $^{40}\text{Ar}^+$  (blue) and  $^{40}\text{K}^+$  time-of-flight peaks for different re-trapping times. b) Time-of-flight spectra showing no re-trapping (black), then with different re-trapping times to capture either  $^{40}\text{Ar}^+$  (blue) or  $^{40}\text{K}^+$  (red) while removing the other isobar.

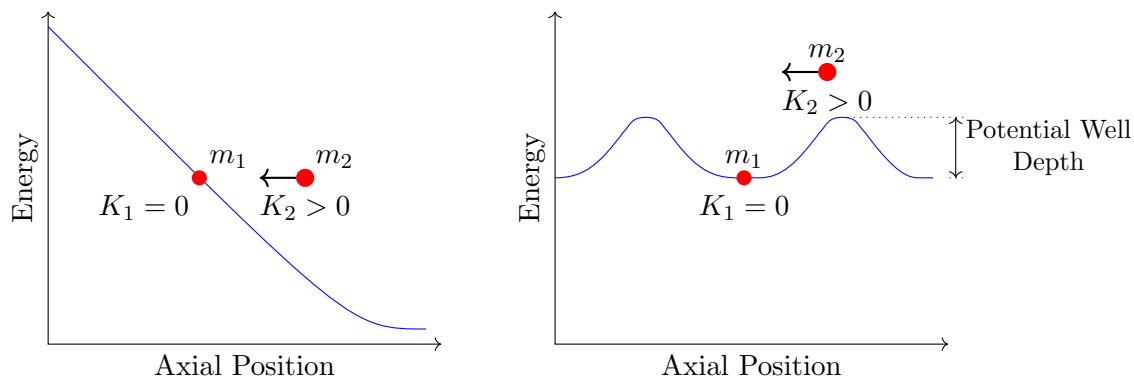


Figure 4.7: An example of ion motion in relation to axial potential during the process of isobar separation through re-trapping. Left: Retarding field slowing ions prior to trapping. Right: Shallow potential well applied to trap ion of interest. Ions are represented in red with the ion of interest and contaminant are represented as  $m_1$  and  $m_2$  respectively. Axial potentials are represented as blue lines.

re-trapping a retarding field is formed in the preparation trap until the moment the ion of interest has zero kinetic energy at which time the potential is switched to a shallow trapping potential (Figure 4.7). A shallow well is used so that contaminant ions still have sufficient kinetic energy to escape the trap. However, real ions will have a distribution in phase space rather than arriving at a single time and energy. The result is that some ions of interest will still have sufficient kinetic energy to escape a potential well shallow enough to exclude isobaric contaminants, reducing the ion capture efficiency. The well can be made deeper to improve capture efficiency, but this will also reduce the resolving power of the separation method. The result is a trade-off between increased resolving power and capture efficiency [42].

Another factor affecting re-trapping efficiency stems from the mass dependence of the ion of interest's speed. Ideally the trap would close instantaneously and ions would experience static axial electric fields from either the open or closed potential. However the actual switching time is around 100 ns, which results in ions sampling axial electric fields in an intermediate state between the open and closed state. Faster moving light ions will experience more of these intermediate fields as ions moving at higher speed they will be further from the trap centre when switching begins. Mass  $A = 40$  ions at 1300 eV will move at approximately 80 mm/ $\mu$ s, traversing a distance of 8 mm within 100 ns, comparable to the length of the trap which is 7 mm. The ions experience the electric potential dynamically increasing as they are slowed, thus increasing their kinetic energy in a fashion similar to how a pulsed drift tube decreases the total ion energy. The result is that trapping efficiency of lighter ions will be decreased.

## 4.2 Summary

The TITAN MR-ToF has now been installed into the TITAN beamline and it was demonstrated to be able to accept ISAC beam, perform mass measurements, and remove isobaric contamination through mass-selective re-trapping. An ion transport efficiency of around 10% was achievable with an  $^{40}\text{Ar}^+$  beam transported from the TITAN CB to the MR-ToF. This efficiency is below the expected 20%, though we expect higher efficiencies to be achievable when transporting elements with a lower ionization energy. The MR-ToF demonstrated a mass resolving power of 202 000 while measuring  $^{40}\text{Ar}^+$  and  $^{40}\text{K}^+$ , exceeding expectation by a factor

of 2. Also the MR-ToF was shown to be able to remove either of these two ion species through mass-selective re-trapping, requiring a minimum resolving power of 25 000; above the expected resolving power of 20 000. The mass measurement and isobar separation resolving powers are greater than the performance expectations and both were achieved within the required 10 ms. With the MR-ToF functioning as part of the TITAN system, as well as beam transport properties discussed in Chapter 3, the MR-ToF is ready for use with radioactive beam from ISAC to contribute to the scientific work of TITAN.

# Chapter 5

## Summary and outlook

The TITAN experiment at TRIUMF has had many years of successful Penning trap use. The incoming beam was prepared using a linear Paul trap and an EBIT for charge breeding to enable high precision mass measurements of rare isotopes. Now an additional type of ion trap has been added to TITAN to expand the possibilities for measurements, a Multi-Reflection Time-of-Flight (MR-ToF) mass spectrometer and isobar separator. Through this thesis the process of integrating an MR-ToF into the TITAN experiment has been discussed. This has involved studies of how to maximize ion transport into and out of the MR-ToF and demonstrating the capacity of the MR-ToF to perform mass measurement and isobar separation as part of the TITAN system.

A key component of the MR-ToF integration was understanding how to maximize the efficiency of ion transport through the TITAN beamline to, from, or bypassing the MR-ToF. We also desired to optimize beam emittance out of the MR-ToF for measurements using EBIT and MPET. To this end a set of SIMION simulations were produced of the TITAN beamline to study and optimize the movement of ions through the beamline. The starting point of these simulations was the TITAN cooler buncher (CB) which is a linear Paul trap used to prepare beam for measurements in TITAN. CB simulations were validated first through comparison to earlier CB simulations, then through comparison to experimental emittance measurements. An Allison meter was used to measure the transverse emittance of the beam ejected from the CB to the location of the MR-ToF input optics. Comparing transverse emittance measurements, the experimental measurement was found to be 1.7 times larger than simulation. Further comparisons between simulation and experiment were found through measuring and simulating the beam time profiles at two MCPs in the TITAN beamline. Disagreements as large as a factor of 2 have been observed in the time profiles. It appears that the ion phase space of the cooled ions simulated in the CB is different than what is achieved in experiment, possibly due to differences in available cooling time as well as the continuous input of ions from ISAC within the physical CB. For future use of these simulations it may be more effective to empirically define the initial phase space to have closer agreement between simulated and experimental emittance. An additional impediment to producing closer agreement between simulation and experiment is the interaction of ions with structures in the beamline. Ion trajectories passing close to beamline structures are sensitive to minor differences between simulation and experiment, likely contributing to disagreement between simulation and experiment. Again, this may merit a more empirical approach to simulating the initial ion phase space within the CB for future simulation work. Notably however, settings on electrostatic beamline elements reproduced in simulation show high ion transmission, even where differences in bender voltages  $< 1\%$  would completely prevent ion transmission. This appears to indicate a useful simulation of the electrostatic beamline in simulation. Thus an understanding was gained of how precisely these simulations could guide experimental beamline optimizations.

Using the beamline simulations, an exploration of optimal electrode settings for ion injection into the MR-ToF was performed. The MR-ToF injection ion optics were recreated in simulation to study the acceptance of the optics. The acceptance was simulated for a range of voltages

on two key electrodes to find optimal settings for matching the beam emittance from the TITAN CB. To improve efficiency of ion transport into the MR-ToF through matching the CB emittance to the MR-ToF acceptance a new split Einzel lens (SEL) was added to the TITAN beamline. Simulations were done of the TITAN beamline between the CB and MR-ToF input optics to find optimal settings of lenses EL5 and SEL for injection of a 1.4 keV beam into the MR-ToF. Simulations predict 95% efficiency of beam transport into the MR-ToF from the CB. Similar voltages to those suggested were used for successful ion transport into the MR-ToF in experiment. In addition to injection into the MR-ToF, simulations were used to provide suggested voltages for beam transport from the MR-ToF towards MPET. A maximum transmission of 19% was achieved for the variables adjusted. It may be possible to improve this transmission and the related phase space distribution by adjusting the depth of the trap potential well. Also we may explore the impact of switching the DC voltage on the close by RFQ electrodes.

Additional simulations were used to investigate the impact of MR-ToF integration on the TITAN beamline when bypassing the MR-ToF. To allow transport of ions into the MR-ToF the SEL was added to the TITAN beamline and a 7.9 mm diameter hole was created in the B1-OUT electrode; simulations were used to characterize the impact of these modifications. This was accomplished by examining the transverse emittance at a position past the section where the modifications were made. Comparisons show the calculated emittance before and after the changes agree within uncertainty and the emittance plots appear nearly identical. The lack of negative impact from the new optics has been supported by experimental observations.

The final step in integrating the MR-ToF into the TITAN system was the physical installation and tests of the MR-ToF using beam delivered from ISAC. These tests were performed using an  $^{40}\text{Ar}^+$  beam produced in the ISAC OffLine Ion Source (OLIS) to measure beam transport efficiency and demonstrate mass measurements as well as isobar separation in the MR-ToF. Efficiency measurements found it possible to achieve 10% transport efficiency of  $^{40}\text{Ar}^+$  beam from the CB to MR-ToF, lower than the anticipated 20%. A major factor in the loss of efficiency is due to charge exchange with contaminant ions in the helium buffer gas. Much of which is introduced by outgassing of the carbon-doped plastic RFQ rods in the MR-ToF transport system. We expect higher efficiencies can be achieved using elements with lower ionization energies which have a lower probability of charge exchange.

Mass measurements were performed for a range of ion flight times. One function was to perform broadband mass measurements to identify various beam constituents. A high resolution mass measurement was also performed, demonstrating a resolving power of 202 000, exceeding the expected 100 000 by a factor of 2. Isobar separation was demonstrated using mass-selective re-trapping. For this test a mixture of  $^{40}\text{Ar}^+$  and  $^{40}\text{K}^+$  was fed into the MR-ToF, then various re-trapping times were studied to show either isobar can be removed. This isobar separation showed the MR-ToF achieving at minimum a resolving power of 25 000, an improvement over the anticipated 20 000. Thus it was demonstrated that the MR-ToF can function as an integrated component of the TITAN system and work with externally produced beam delivered from ISAC.

Since online commissioning the MR-ToF has already begun to show its utility in TITAN. The MR-ToF was used as a complementary mass spectrometer for measurements of neutron-rich titanium measurements done in MPET. The MR-ToF was able to provide diagnostics of the beam constituents as well as measure isotopes arriving with too high a contamination level for measurement in MPET. It has also been used to measure yields of neutron-rich gallium isotopes produced in ISAC during beam development to explore the possibility of future experiments with Penning trap measurements.

The MR-ToF is now a working part of the TITAN experiment which opens up a range of

exciting new possibilities for measurements to be performed at TITAN.

# Bibliography

- [1] Y. Blumenfeld et al. “Facilities and methods for radioactive ion beam production”. In: *Physica Scripta* 2013 (2013), p. 14023.
- [2] G. Bollen et al. “The accuracy of heavy-ion mass measurements using time of flight-ion cyclotron resonance in a Penning trap”. In: *Journal of Applied Physics* 68.9 (1990), pp. 4355–4374.
- [3] T. Eronen et al. “Preparing isomerically pure beams of short-lived nuclei at JYFLTRAP”. In: *Nuclear Instruments and Methods in Physics Research B* 266 (2008), pp. 4527–4531.
- [4] S. Guan and A.G. Marshall. “Stored waveform inverse Fourier transform (SWIFT) ion excitation intrapped-ion mass spectrometry: theory and applications”. In: *International Journal of Mass Spectrometry and Ion Processes* 157-158 (1996), pp. 5–37. DOI: 10.1016/S0168-1176(96)04461-8.
- [5] F Herfurth et al. “A linear radiofrequency ion trap for accumulation, bunching, and emittance improvement of radioactive ion beams”. In: *Nuclear Instruments and Methods in Physics Research Section A: Accelerators, Spectrometers, Detectors and Associated Equipment* 469.2 (2001), pp. 254–275. DOI: [http://doi.org/10.1016/S0168-9002\(01\)00168-1](http://doi.org/10.1016/S0168-9002(01)00168-1).
- [6] A. Nieminen et al. “Beam cooler for low-energy radioactive ions”. In: *Nuclear Instruments and Methods in Physics Research Section A: Accelerators, Spectrometers, Detectors and Associated Equipment* 469.2 (2001), pp. 244–253. DOI: [http://dx.doi.org/10.1016/S0168-9002\(00\)00750-6](http://dx.doi.org/10.1016/S0168-9002(00)00750-6).
- [7] Wolfgang R. Plaß et al. “Isobar separation by time-of-flight mass spectrometry for low-energy radioactive ion beam facilities”. In: *Nuclear Instruments and Methods in Physics Research Section B: Beam Interactions with Materials and Atoms* 266.19–20 (2008). Proceedings of the {XVth} International Conference on Electromagnetic Isotope Separators and Techniques Related to their Applications, pp. 4560–4564. ISSN: 0168-583X. DOI: <https://doi.org/10.1016/j.nimb.2008.05.079>.
- [8] H. Wollnik and M. Przewloka. “Time-of-flight mass spectrometers with multiply reflected ion trajectories”. In: *International Journal of Mass Spectrometry and Ion Processes* 96.3 (1990), pp. 267–274. DOI: [http://dx.doi.org/10.1016/0168-1176\(90\)85127-N](http://dx.doi.org/10.1016/0168-1176(90)85127-N).
- [9] Hermann Wollnik. “History of mass measurements in time-of-flight mass analyzers”. In: *International Journal of Mass Spectrometry* 349 (2013). 100 years of Mass Spectrometry, pp. 38–46. DOI: <http://dx.doi.org/10.1016/j.ijms.2013.04.023>.
- [10] Georg Bollen. “Traps for Rare Isotopes”. In: *The Euroschool Lectures on Physics with Exotic Beams, Vol. I*. Ed. by Jim Al-Khalili and Ernst Roeckl. Berlin, Heidelberg: Springer Berlin Heidelberg, 2004, pp. 169–210. DOI: 10.1007/978-3-540-44490-9\_6.

- 
- [11] Lowell S. Brown and Gerald Gabrielse. “Precision spectroscopy of a charged particle in an imperfect Penning trap”. In: *Phys. Rev. A* 25 (4 Apr. 1982), pp. 2423–2425. DOI: 10.1103/PhysRevA.25.2423.
- [12] M. König et al. “Quadrupole excitation of stored ion motion at the true cyclotron frequency”. In: *International Journal of Mass Spectrometry and Ion Processes* 142.1 (1995), pp. 95–116. DOI: [http://dx.doi.org/10.1016/0168-1176\(95\)04146-C](http://dx.doi.org/10.1016/0168-1176(95)04146-C).
- [13] G. Bollen et al. “Resolution of nuclear ground and isomeric states by a Penning trap mass spectrometer”. In: *Phys. Rev. C* 46 (6 Dec. 1992), R2140–R2143. DOI: 10.1103/PhysRevC.46.R2140.
- [14] A.A. Kwiatkowski et al. “Isobaric beam purification for high precision Penning trap mass spectrometry of radioactive isotope beams with SWIFT”. In: *International Journal of Mass Spectrometry* 379 (2015), pp. 9–15. DOI: <http://dx.doi.org/10.1016/j.ijms.2014.09.016>.
- [15] M. Rosenbusch et al. “Buffer-gas-free mass-selective ion centering in Penning traps by simultaneous dipolar excitation of magnetron motion and quadrupolar excitation for interconversion between magnetron and cyclotron motion”. In: *International Journal of Mass Spectrometry* 325 (2012). Eugene N. Nikolaev 65th Birthday Honor Issue, pp. 51–57. DOI: <http://dx.doi.org/10.1016/j.ijms.2012.06.008>.
- [16] W. Paul and H. Steinwedel. “Notizen: Ein neues Massenspektrometer ohne Magnetfeld”. In: *Zeitschrift Naturforschung Teil A* 8 (July 1953), pp. 448–450. DOI: 10.1515/zna-1953-0710.
- [17] Wolfgang Paul. “Electromagnetic traps for charged and neutral particles”. In: *Rev. Mod. Phys.* 62 (3 July 1990), pp. 531–540. DOI: 10.1103/RevModPhys.62.531.
- [18] Raymond E. March and John F. J. Todd. *Quadrupole Ion Trap Mass Spectrometry*. John Wiley & Sons, Inc., 2005. ISBN: 9780471717980. DOI: 10.1002/0471717983.
- [19] Tsviki Y. Hirsh et al. “First operation and mass separation with the CARIBU MR-TOF”. In: *Nuclear Instruments and Methods in Physics Research Section B: Beam Interactions with Materials and Atoms* 376 (2016). Proceedings of the XVIIth International Conference on Electromagnetic Isotope Separators and Related Topics (EMIS2015), Grand Rapids, MI, U.S.A., 11-15 May 2015, pp. 229–232. DOI: <http://dx.doi.org/10.1016/j.nimb.2015.12.037>.
- [20] R.N. Wolf et al. “ISOLTRAP’s multi-reflection time-of-flight mass separator/spectrometer”. In: *International Journal of Mass Spectrometry* 349–350 (2013). 100 years of Mass Spectrometry, pp. 123–133. DOI: <https://doi.org/10.1016/j.ijms.2013.03.020>.
- [21] T. Dickel et al. “A high-performance multiple-reflection time-of-flight mass spectrometer and isobar separator for the research with exotic nuclei”. In: *Nuclear Instruments and Methods in Physics Research A* 777 (2015), pp. 172–188. DOI: <http://dx.doi.org/10.1016/j.nima.2014.12.094>.
- [22] Y. Ishida et al. “A time-of-flight mass spectrometer to resolve isobars”. In: *Nuclear Instruments and Methods in Physics Research Section B: Beam Interactions with Materials and Atoms* 219 (2004). Proceedings of the Sixteenth International Conference on Ion Beam Analysis, pp. 468–472. DOI: <http://dx.doi.org/10.1016/j.nimb.2004.01.104>.

- [23] A. Piechaczek et al. “Development of a high resolution isobar separator for study of exotic decays”. In: *Nuclear Instruments and Methods in Physics Research Section B: Beam Interactions with Materials and Atoms* 266.19 (2008). Proceedings of the XVth International Conference on Electromagnetic Isotope Separators and Techniques Related to their Applications, pp. 4510–4514. DOI: <http://dx.doi.org/10.1016/j.nimb.2008.05.149>.
- [24] P. Chauveau et al. “PILGRIM, a Multi-Reflection Time-of-Flight Mass Spectrometer for Spiral2-S3 at GANIL”. In: *Nuclear Instruments and Methods in Physics Research Section B: Beam Interactions with Materials and Atoms* 376 (2016). Proceedings of the XVIth International Conference on Electromagnetic Isotope Separators and Related Topics (EMIS2015), Grand Rapids, MI, U.S.A., 11-15 May 2015, pp. 211–215. DOI: <http://dx.doi.org/10.1016/j.nimb.2016.01.025>.
- [25] James M Kelly et al. “Multi-reflection time-of-flight mass spectrometer (MR-ToF) simulation and commissioning at the University of Notre Dame”. In: *APS April Meeting 2017*. Vol. 62. 1. To appear. 2017. URL: <http://meetings.aps.org/Meeting/APR17/Session/U13.2>.
- [26] Wolfgang R. Plaß, Timo Dickel, and Christoph Scheidenberger. “Multiple-reflection time-of-flight mass spectrometry”. In: *International Journal of Mass Spectrometry* 349-350 (2013), pp. 134–144.
- [27] M. Marchetto, R. A. Baartman, and R. E. Laxdal. “ARIEL front end”. In: *Hyperfine Interactions* 225.1 (Jan. 2014), pp. 275–282. DOI: 10.1007/s10751-013-0908-4.
- [28] A. A. Kwiatkowski et al. “TITAN: An ion trap facility for on-line mass measurement experiments”. In: *Hyperfine Interactions* 225.1 (2014), pp. 143–155. DOI: 10.1007/s10751-013-0892-8.
- [29] J. Dilling, R. Krücken, and G. Ball. “ISAC overview”. In: *Hyperfine Interactions* 225.1 (2014), pp. 1–8. DOI: 10.1007/s10751-013-0877-7.
- [30] J. Dilling et al. “The proposed TITAN facility at ISAC for very precise mass measurements on highly charged short-lived isotopes”. In: *Nuclear Instruments and Methods in Physics Research Section B: Beam Interactions with Materials and Atoms* 204 (2003). 14th International Conference on Electromagnetic Isotope Separators and Techniques Related to their Applications, pp. 492–496. DOI: [http://dx.doi.org/10.1016/S0168-583X\(02\)02118-3](http://dx.doi.org/10.1016/S0168-583X(02)02118-3).
- [31] I. Bylinskii and M. K. Craddock. “The TRIUMF 500 MeV cyclotron: the driver accelerator”. In: *Hyperfine Interactions* 225.1 (2014), pp. 9–16. DOI: 10.1007/s10751-013-0878-6.
- [32] M. Dombisky and P. Kunz. “ISAC targets”. In: *Hyperfine Interactions* 225.1 (2014), pp. 17–23. DOI: 10.1007/s10751-013-0879-5.
- [33] P.G. Bricault et al. “Rare isotope beams at ISAC—target & ion source systems”. In: *Hyperfine Interactions* 225 (1 2014), pp. 25–49. DOI: 10.1007/s10751-013-0880-z.
- [34] T. Brunner et al. “TITAN’s digital RFQ ion beam cooler and buncher, operation and performance”. In: *Nuclear Instruments and Methods in Physics Research, Section A: Accelerators, Spectrometers, Detectors and Associated Equipment* 676 (June 2012), pp. 32–43. DOI: 10.1016/j.nima.2012.02.004.

- [35] A. Lapiere et al. “The TITAN EBIT charge breeder for mass measurements on highly charged short-lived isotopes—First online operation”. In: *Nuclear Instruments and Methods in Physics Research Section A: Accelerators, Spectrometers, Detectors and Associated Equipment* 624.1 (2010), pp. 54–64. DOI: <https://doi.org/10.1016/j.nima.2010.09.030>.
- [36] Matthew Foster. “An Upgrade of the TITAN-EBIT High Voltage Operation for Investigations into Decay Rate Modifications by Highly Charged Ions”. MSc. University of Surrey, 2017.
- [37] T. Brunner et al. “In-trap decay spectroscopy for  $2\nu\beta\beta$  decay experiments”. In: *Hyperfine Interactions* 199.1 (Apr. 2011), p. 191. DOI: [10.1007/s10751-011-0313-9](https://doi.org/10.1007/s10751-011-0313-9).
- [38] Dinko Atanasov et al. “Between atomic and nuclear physics: radioactive decays of highly-charged ions”. In: *Journal of Physics B: Atomic, Molecular and Optical Physics* 48.14 (2015), p. 144024.
- [39] K.G. Leach et al. “The TITAN in-trap decay spectroscopy facility at TRIUMF”. In: *Nuclear Instruments and Methods in Physics Research Section A: Accelerators, Spectrometers, Detectors and Associated Equipment* 780 (2015), pp. 91–99. DOI: <http://dx.doi.org/10.1016/j.nima.2014.12.118>.
- [40] M. Brodeur et al. “Verifying the accuracy of the {TITAN} Penning-trap mass spectrometer”. In: *International Journal of Mass Spectrometry* 310 (2012), pp. 20–31. DOI: <https://doi.org/10.1016/j.ijms.2011.11.002>.
- [41] M. Smith et al. “First Penning-Trap Mass Measurement of the Exotic Halo Nucleus  $^{11}\text{Li}$ ”. In: *Phys. Rev. Lett.* 101 (20 Nov. 2008), p. 202501. DOI: [10.1103/PhysRevLett.101.202501](https://doi.org/10.1103/PhysRevLett.101.202501).
- [42] Timo Dickel et al. “Isobar Separation in a Multiple-Reflection Time-of-Flight Mass Spectrometer by Mass-Selective Re-Trapping”. In: *Journal of The American Society for Mass Spectrometry* (2017), pp. 1–12. DOI: [10.1007/s13361-017-1617-z](https://doi.org/10.1007/s13361-017-1617-z).
- [43] Christian Jesch. “The Multiple-Reflection Time-of-Flight Isobar Separator for TITAN and Direct Mass Measurements at the FRS Ion Catcher”. PhD. Justus-Liebig-Universität Gießen, 2016.
- [44] Devin Short. “Nuclear Isobar Separation for Penning Trap Mass Measurements at TRIUMF”. Master of Science. Simon Fraser University, 2017.
- [45] R B Moore et al. “Production, transfer and injection of charged particles in traps and storage rings”. In: *Physica Scripta* 1995.T59 (1995), p. 93.
- [46] Martin Reiser. *Theory and Design of Charged Particle Beams*. Wiley-VCH, 2004.
- [47] Hermann Wollnik. *Optics of Charged Particles*. San Diego, California 92101: Academic Press, Inc., 1987.
- [48] Mikhail Yavor. “Optics of Charged Particle Analyzers”. In: *Advances in Imaging and Electron Physics*. Ed. by Peter W. Hawkes. Vol. 157. Academic Press, 2009.
- [49] R. V. Latham. *High voltage vacuum insulation: basic concepts and technological practice*. London: Academic, 1995.
- [50] Inc. Scientific Instrument Services. *SIMION*. Software. Version 8.1.1.32-2013-05-20. May 20, 2013. URL: <http://simion.com/>.

- 
- [51] Richard Baartman. “ISAC LEBT”. In: *Hyperfine Interactions* 225.1 (2014), pp. 69–77. DOI: 10.1007/s10751-013-0883-9.
- [52] B. A. Mamyrin et al. “The mass-reflectron, a new nonmagnetic time-of-flight mass spectrometer with high resolution”. In: *Sov. Phys-JETP* 37.1 (July 1972).
- [53] R. Kutscher et al. “A transversally and longitudinally focusing time-of-flight mass spectrometer”. In: *International Journal of Mass Spectrometry and Ion Processes* 103.2 (1991), pp. 117–128. DOI: [http://dx.doi.org/10.1016/0168-1176\(91\)80083-Y](http://dx.doi.org/10.1016/0168-1176(91)80083-Y).
- [54] M.P. Reiter. personal communication. 2017.
- [55] Timo Dickel et al. “Dynamical time focus shift in multiple-reflection time-of-flight mass spectrometers”. In: *International Journal of Mass Spectrometry* 412 (2017), pp. 1–7. DOI: <https://doi.org/10.1016/j.ijms.2016.11.005>.
- [56] Y Toker et al. “The kick-out mass selection technique for ions stored in an Electrostatic Ion Beam Trap”. In: *Journal of Instrumentation* 4.09 (2009), P09001.
- [57] Gholamreza Javahery and Bruce Thomson. “A segmented radiofrequency-only quadrupole collision cell for measurements of ion collision cross section on a triple quadrupole mass spectrometer”. In: *Journal of the American Society for Mass Spectrometry* 8.7 (1997), pp. 697–702. DOI: [http://dx.doi.org/10.1016/S1044-0305\(97\)00027-5](http://dx.doi.org/10.1016/S1044-0305(97)00027-5).
- [58] A. Dodonov et al. “A new technique for decomposition of selected ions in molecule ion reactor coupled with ortho-time-of-flight mass spectrometry”. In: *Rapid Communications in Mass Spectrometry* 11.15 (1997), pp. 1649–1656.
- [59] A. Takamine et al. “Improvement of slow RI beam transport using carbon-OPIG”. In: *RIKEN Accelerator Progress Report*. Vol. 40. 2007.
- [60] M.D.N. Lunney, F. Buchinger, and R.B. Moore. “The Temperature of Buffer-gas Colled Ions in a Paul Trap”. In: *Journal of Modern Optics* 39.2 (1992), pp. 349–360. DOI: 10.1080/09500349214550341.
- [61] John F. O’Hanlon. *A User’s Guide to Vacuum Technology*. 3rd ed. Hoboken, New Jersey: John Wiley & Sons, Inc., 2003.
- [62] Wolfgang R. Plaß et al. “High-performance multiple-reflection time-of-flight mass spectrometers for research with exotic nuclei and for analytical mass spectrometry”. In: *Physica Scripta* 2015.T166 (2015), p. 014069.
- [63] Laura Gail Blomeley. “First Tests of a Square Wave Radio Frequency Quadrupole Cooler and Buncher for TITAN”. MSc. McGill University, 2007.
- [64] D. Manura and D. Dahl. *SIMION (R) 8.0 User Manual*. Ringoes, NJ 08551: Scientific Instrument Services, Inc., 2008. URL: <http://simion.com/>.
- [65] Matthew Jonathon Smith. “A Square-Wave-Driven Radiofrequency Quadrupole Cooler and Buncher for TITAN”. Master of Science. The University of British Columbia, 2005.
- [66] P. W. Allison, J. D. Sherman, and D. B. Holtkamp. “An Emittance Scanner for Intense Low-Energy Ion Beams”. In: *IEEE Transactions on Nuclear Science* 30.4 (Aug. 1983), pp. 2204–2206. DOI: 10.1109/TNS.1983.4332762.
- [67] Joseph Ladislav Wiza. “Microchannel plate detectors”. In: *Nuclear Instruments and Methods* 162.1–3 (1979), pp. 587–601. DOI: [https://doi.org/10.1016/0029-554X\(79\)90734-1](https://doi.org/10.1016/0029-554X(79)90734-1).

- [68] Richard Baartman. personal communication. Apr. 2017.
- [69] J. Arol Simpson. “Design of Retarding Field Energy Analyzers”. In: *Review of Scientific Instruments* 32.12 (1961), pp. 1283–1293. DOI: 10.1063/1.1717235.
- [70] Ruben Schupp. “Determination of beam properties of highly-charged ions extracted from TITAN’s electron beam ion trap”. MSc. University of Heidelberg, 2016.
- [71] C. Babcock. personal communication. Mar. 2017.
- [72] Mathew Smith et al. “First tests of the TITAN digital RFQ beam cooler and buncher”. In: *Hyperfine Interactions* 173.1 (2006), pp. 171–180. DOI: 10.1007/s10751-007-9554-z.
- [73] P. Delheij et al. “The TITAN mass measurement facility at TRIUMF-ISAC”. In: *Hyperfine Interactions* 173.1 (Nov. 2006), pp. 123–131. DOI: 10.1007/s10751-007-9573-9.
- [74] J. Dilling et al. “Mass measurements on highly charged radioactive ions, a new approach to high precision with TITAN”. In: *International Journal of Mass Spectrometry* 251.2 (2006). ULTRA-ACCURATE MASS SPECTROMETRY AND RELATED TOPICS Dedicated to H.-J. Kluge on the occasion of his 65th birthday anniversary, pp. 198–203. DOI: <http://dx.doi.org/10.1016/j.ijms.2006.01.044>.
- [75] 2014.
- [76] Alexander Pikhteleev and Julian Bergmann. *MAc*. Software. Version 0.9. 2009-2017.
- [77] K. Jayamanna. “Off line ion source terminal”. In: *ISAC and ARIEL: The TRIUMF Radioactive Beam Facilities and the Scientific Program*. Ed. by Jens Dilling, Reiner Krücken, and Lia Merminga. Dordrecht: Springer Netherlands, 2014, pp. 51–62. DOI: 10.1007/978-94-007-7963-1\_5.
- [78] K. Jayamanna et al. “Microwave-driven multipurpose ion source”. In: *Review of Scientific Instruments* 67.3 (1996), pp. 1061–1063. DOI: 10.1063/1.1146758.
- [79] Meng Wang et al. “The AME2016 atomic mass evaluation (II). Tables, graphs and references”. In: *Chinese Physics C* 41.3 (2017), p. 030003.

# Appendix A

## Introduction to SIMION

SIMION is a software package able to numerically calculate electric and magnetic fields and the resulting trajectories of charged particles flying through these fields [64]. By default these fields are simulated as static, however dynamic changes may be simulated through user programming implemented via scripts in the programming language Lua 5.1. In this thesis, Lua scripts were used to implement time-varying effects in the simulations such as switching of RF fields and other electrode potentials, as well as buffer-gas collisions. Scripts were also used to vary simulation parameters such as electrode voltages, gas pressure, and different timing parameters. The varying of simulation parameters was achieved by inputting a list of values to be used for a given parameter.

Electric fields are calculated through solving the Laplace equation based on a defined electrode geometry and potentials. Magnetic fields were not simulated for this thesis, so we shall neglect a discussion of how they are rendered. Geometries are defined by filling in points in a three dimensional grid, wherein each point is either part of an electrode, grounded, or empty space. The resolution with which a given geometry is modelled depends on the length per grid unit defined for each linear direction ( $x$ ,  $y$ , and  $z$ ). Resolutions are expressed as grid units per mm (gu/mm). A major limiting factor in the resolutions which can be achieved is the computer memory requirements to produce high resolution simulations. These electrode geometries and the resulting Laplace solutions are saved in Potential Array (PA) files.

Where electrode geometries are simple, measurements could be taken directly from drawings and models of the beamline to define the geometries within SIMION. The direct definition of simulation geometries is done using geometry or *GEM* files. The commands available to define GEM files are limited in their scope, making it difficult to render complex geometries. Thus for more complex structures it is desirable to define an electrode model in some external software, such as SolidWorks [75], which can be imported into SIMION.

If a geometry has been saved as a STereoLithography (STL) model, it is possible to convert the geometry into a PA. This conversion of STL models was used—for example—in defining the spherical benders in the TITAN beamline, which were significantly more difficult to reproduce using the the tools available in SIMION. STL models do however have the limitation that symmetry planes cannot be defined to reduce the computational load of simulating the PA. Conversions of STL models are also prone to small aberrations in the geometries which can produce unphysical inhomogeneities in the resulting electric fields. Such inhomogeneities were observed in some beamline simulations where the ion beam was passing straight through sections converted from STL models and experienced steering effects where there should be none. In such cases, simplified GEM file versions of the electrodes were defined to simulate scenarios where the beam is not being steered.

## Appendix B

# Experimental operating parameters for emittance and time profile measurements

Table B.1: A summary of the voltages applied to the TITAN beamline electrodes for the time-profile measurements discussed in Section 3.1.3. Positions of the electrodes in the TITAN beamline are indicated in Figure 3.1.

Beamline Section	Electrode	Set Voltage (V)
TRFC	RFQ18	4.8
	RFQ19	4
	RFQ20	3.2
	RFQ21	2.4
	RFQ22	1
	RFQ23	-14
	RFQ24	20
	RFQ22 (extraction)	1
	RFQ24 (extraction)	-21
	Bias	20000
	PB5	17600
	EL5	-3600
TRFCBL	XCB0	100
	CCB0	100
	B1-IN	334
	B1-OUT	388
	Q1	250
	Q2	250
	XCB4	105
	YCB4T	222
	YCB4B	-222
TSYBL	EL1	2100
	EL3	2780
	CCB2	250
	XCB9	262
	YCB9	250
	EL4	2350
MPETBL	EL2	1770
	CCB3	250
	XCB3	254
	YCB3	258

# Appendix C

## Allison meter data analysis methodology

To summarize the process of converting the raw time profile data into ion counts for a particular Allison meter setting, let us make reference to the summary of data presented in Figure 3.5. We shall refer to the number of counts in an individual time profile bin as  $N_{ij}$ , where  $i$  corresponds to the Measurement Index in Figure 3.5 and  $j$  refers to the time profile bin. Specific time intervals were chosen to cover time profile data from the Allison meter MCP, MCP-1, and a sample of the background counts. We represent the start and end indices of the Allison meter MCP data as  $Al_0$ – $Al_1$ . Then, expressing the normalization for a given measurement as  $\nu_i$  and the mean of the background counts as  $\langle N^{BG} \rangle_i$ , we may approximate the real ion counts at the Allison meter MCP  $\hat{N}_i$  as,

$$\hat{N}_i = \nu_i \sum_{j=Al_0}^{Al_1} (N_{ij} - \langle N^{BG} \rangle_i). \quad (\text{C.1})$$

With the number of counts for a given Allison meter position and voltage determined, we finally combine this with the meter position and the divergence calculated with Equation 3.1 to produce a plot of the emittance. Without the normalization and background subtraction of ion counts the result is Figure 3.6 a, but with this processing we instead get Figure 3.6 b. We see in Figure 3.6 c the result of rescaling the  $z$ -axis of the emittance plot to highlight the fluctuations in the background noise of the data. The processing of ion counts removes most of the noise, but there remains a fluctuation in the background  $\leq 2\%$  of the maximum ion count. In order to calculate the rms emittance we need to ensure that we are not changing the results by counting of background noise.

To correct for the background counts in the rms emittance calculation a threshold was set under which any counts would be set to zero. The level of this threshold was chosen by examining how the calculated rms emittance varies as a function of where the threshold level was set, as shown in Figure C.2. The threshold was calculated as a multiple of the standard deviation of a section of background far away from the real ion counts to allow easy adaptation to different levels of background variations. For the example here we can see the effect that there are more negative background counts than positive, which reduces the rms emittance calculation to zero for a threshold below  $\approx -1.5$  (we note that the value would actually be imaginary due to taking a square root of a negative value, but the key point here is that the result of a low threshold is a calculation which does not reflect physical reality). The calculated emittance approaches a maximum as the threshold goes to zero due to negative background counts being removed while the effect of positive background noise remains. We can see where the inflating effect from the background is removed when the rms emittance decreases steadily as a function of threshold. In the example of Figure C.2, this inflating effect disappears at a threshold of  $\approx 3$  background standard deviations. For higher threshold values we see a slow, but steady decrease in calculated emittance due to real counts being removed by the threshold.

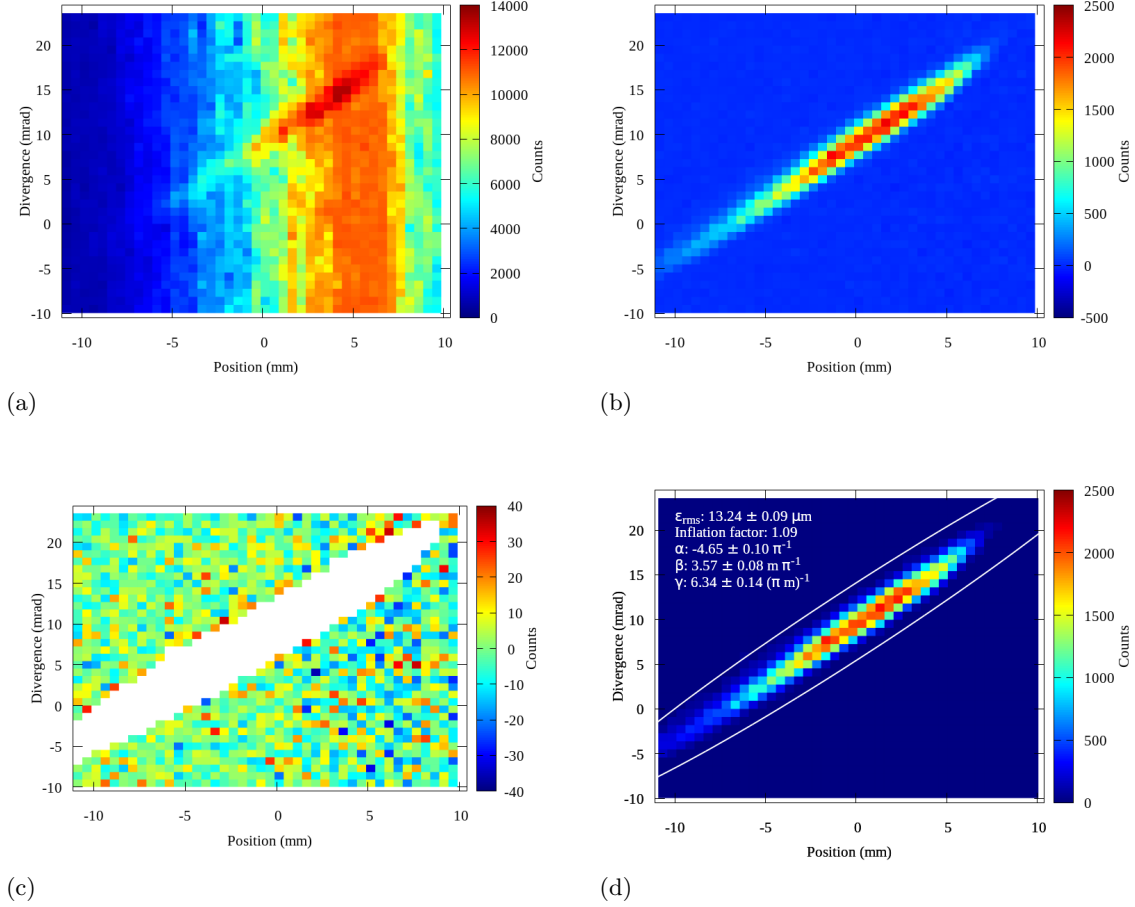


Figure C.1: Emittance plots from one measurement of the beam out of the TITAN CB with the current standard tune, showing different levels of processing of the number of ions detected at each position and divergence. a) An emittance plot with no processing of the ion counts, showing a large biasing effect due to drift in the MCS. b) An emittance plot with ion count normalization and time-profile background removed, but before a threshold was set to remove background counts for rms emittance calculation. c) The same emittance plot as b), but scaled in the z-axis to highlight the degree of variation of the background counts. Background variations on the level of 2% of the peak ion counts can be seen. d) An emittance plot after the complete ion count processing described in the text. This plot includes the calculated rms emittance and Twiss parameters. A white ellipse calculated from the Twiss parameters is overlaid on the plot with the size set by the equivalent emittance  $4\epsilon_{rms}$

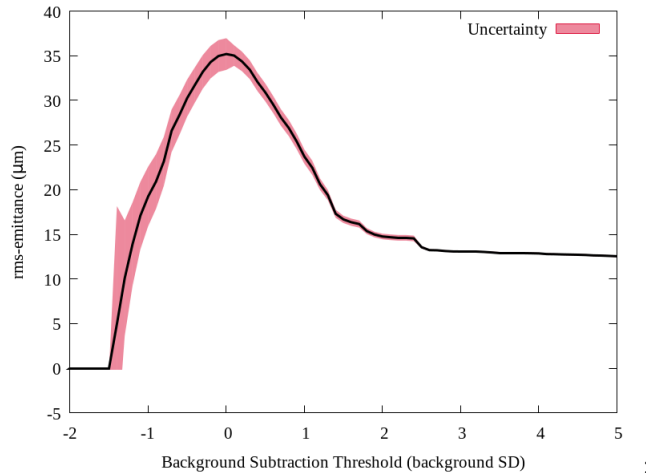


Figure C.2: A plot of the calculated rms emittance as a function of the threshold for setting background noise to zero.

A complication introduced by zeroing all counts below the threshold is that some quantity of real ion counts will be removed along with the noise, thereby artificially lowering the emittance calculated. To estimate this effect of lowering the calculated emittance we shall introduce an inflation factor,  $ifac$ . This inflation factor is the ratio of total ion counts to ion counts removed by the threshold, assuming a bi-Gaussian trace space distribution. To calculate the inflation factor we will define the following terms,

$$pfac = \frac{peak}{thresh}, \quad (C.2)$$

where  $peak$  is the peak number of counts in the emittance distribution, and  $thresh$  is the set threshold value in counts. We can then calculate the inflation factor as,

$$ifac = \frac{pfac}{pfac - (1 + \log(pfac))}. \quad (C.3)$$

In order to exclude data with excessive noise a standard was set that emittance calculations yielding an inflation factor greater than 1.5 would be rejected. Above this inflation factor it could be that more than 33% of the real ion counts have been removed, calling into question the reliability of the results. With the inflation factor calculated, we expect that the actual emittance will be somewhere between the calculated  $\epsilon_{rms}$  and  $ifac \cdot \epsilon_{rms}$ .

The final result of this analysis for beam from a standard tune of the TITAN CB is shown in Figure 3.6 d.

The implementation of this analysis was done through a Lua script, shown in Appendix D. The methodology is adapted from that described in Reference [63] which in turn was based on MATLAB code developed for beam analysis use at TRIUMF [68].

## Appendix D

# Allison meter data analysis Lua code

```
local inputFilename = "4129"
local csvInput = string.format("%s.csv", inputFilename)
local outputFilename = inputFilename
local calFile = string.format("%scal", inputFilename)
cal = require(calFile)

local setSecBounds = cal.setSecBounds -- boolean to
    decide whether or not to use manually defined section bounds
    local sectionIndex0, sectionIndex1 = cal.sec0, cal.sec1 -- sets bounds of
        where in dataset measurement is happening (minimum is 0)
local trBound0, trBound1 = 0,2040 -- sets bounds
    on integration of trace
local alliPk0, alliPk1 = cal.alliPk0, cal.alliPk1 -- sets trace index
    boundaries on Allison MCP peak
local normPk0, normPk1 = cal.normPk0, cal.normPk1 -- sets trace index
    boundaries on MCP-1 normalisation peak
local bkGnd0, bkGnd1 = cal.bkGnd0, cal.bkGnd1 -- sets trace index
    boundaries background

-- Conversion and range parameters for interpreting raw Allison meter data to give
    physical results
local pos0, pos1, posDelta = cal.pos0, cal.pos1, cal.posDelta -- sets position bounds
    and step size
local volt0, volt1 = cal.volt0, cal.volt1 --
    sets voltage bounds
local ampRatio = cal.ampRatio -- ratio by which soft daq voltage is multiplied
    by amplifier to give readout voltage
local KE = cal.KE -- beam energy
local voltCol = cal.voltCol -- sets column to reference for Allison
    meter voltage used (mainly to choose between softdac or readback)
local trStart = cal.trStart -- column where trace data starts (in case
    there are other variables in the data)
local voltInvert = cal.voltInvert -- input 1 or -1 - this is to invert the voltage
    to account for plates being reversed (can also apply global multiplicative factor,
    but probably don't need that...)

local posCal = 1.0 -- calibration on position [mm/step
]
local Leff = 69.85 -- length of Allison meter plates [
mm]
local gap = 4.0 -- gap between Allison meter plates
[mm]

local x_err = 0.0032*posCal -- [mm] (stepper motor resolution of 200
steps/turn)
```

```

local V_errR = 5.5e-5
local KE_err = 4.0
local Leff_errR = 0.021
local gap_errR = 0.01

local equivEmit = 4 -- factor determines size of plotted
    emittance ellipse by calculating equivalent emittance from rms-emittance with this
    factor

-- Set which functions to run:
local _writeEmitPlotData = true -- Function to write emittance plot
    data and produce plot
    local tMinX,tMaxX = cal.tMinX,cal.tMaxX -- x boundaries on
        background region for thresholding
    local tMinXP,tMaxXP = cal.tMinXP,cal.tMaxXP -- x' boundaries on
        background region for thresholding
    local threshold = cal.threshold -- [BG SD] threshold
        under which all data is cut off, set in units of the background standard
        deviation
    local lablx,lably = 0.05,0.92 -- Graph position of label giving
        calculated rms-emittance results

local gpExec = "gnuplot" -- gnuplot executable (
    needed for migrating code to other computers)

local csvLines = {}
local parsedData = {}

--[[General utility functions]]--
-- Function to check if two numbers are the same within some tolerance
function equalish(number,target,tolerance)
    if tonumber(number) > target-tolerance and tonumber(number) < target+tolerance
        then
            return true
        else
            return false
        end
end

-- Function to round a number to the nearest integer value
function round(number)
    if number - math.floor(number) < 0.5 then return math.floor(number)
    else return math.ceil(number) end
end

-- Sum all numbers in list from index "start" to index "finish"
function integrate(list,start,finish)
    sum = 0
    for i = start, finish do
        sum = sum + tonumber(list[i])
    end
    return sum
end

-- Function to calculate average of a list
function average(list)

```

```

    result = 0
    if #list ~= 0 then
        for i=1, #list do
            result = result + tonumber(list[i])
        end
        return result/#list
    else
        return 0
    end
end
-- Calculates average from a list. Code acquired from rosettacode.org - 2017-02-16
function median (numlist)
    if type(numlist) ~= 'table' then return numlist end
    table.sort(numlist)
    if #numlist %2 == 0 then return (numlist[#numlist/2] + numlist[#numlist/2+1]) / 2
    end
    return numlist[math.ceil(#numlist/2)]
end
-- Function to calculate standard deviation list
function stdDev(list)
    mean = average(list)
    dev2 = {}
    for i = 1, #list do dev2[i] = (list[i] - mean)*(list[i] - mean) end
    return math.sqrt(average(dev2))
end

--[[Parsing the csv data]]--
-- Read csv data into list of strings
local i = 1
local f = assert(io.open(csvInput,'r'))
    if f then
        for line in f:lines() do
            csvLines[i] = line
            i = i+1
        end
    else
        error("File went bye bye. :(")
    end
f:close()

-- Break up strings at commas to isolate individual elements (probably should be part
of previous part, but, ugh)
for i=1, #csvLines do
    parsedData[i] = {}
    local j=1
    for token in string.gmatch(csvLines[i], "([^\,]+),%s*") do
        parsedData[i][j] = token
        j = j + 1
    end
end

--[[Analysing the parsed data]]--
-- Calculate rms-emittance
function rmsEmit(sec0,sec1,trBound0,trBound1,parsedData,thresh,maxPk)

```

```

local points = {x = {}, xp = {}, xp_err2 = {}, Nx = {}, Nxp = {}, N = {}, nu =
    {}, Nnorm = {}, ABG = {}, BGSD = {}, NA1 = {}}
local norm = 0      -- integrate over first normalization peak for reference
local BGSD_table = {}

-- Take raw parsed data and assign it to variables for calculations
local n = 1
for i=sec0, sec1 do
    local bkGnd,BGSD,normRatio = 0,0,1.0

    local bkGndList = {}
    for j=1, bkGnd1-bkGnd0 do bkGndList[j] = parsedData[i][trStart+bkGnd0
        -1+j] end

    bkGnd = average(bkGndList)
    points.ABG[n] = bkGnd -- save average background for error propagation

    -- calculate list of variations from mean if mean background is being
    -- subtracted
    bkGndList = {}
    for j=1, bkGnd1-bkGnd0+1 do bkGndList[j] = (parsedData[i][trStart+
        bkGnd0-1+j]-bkGnd)^2 end

    -- calculate standard deviation from list of variations for error
    -- propagation
    points.BGSD[n] = math.sqrt(integrate(bkGndList,1,#bkGndList)/#bkGndList
        )

    if i == sec0 then norm = integrate(parsedData[sec0],trStart+normPk0,
        trStart+normPk1) - bkGnd*(normPk1-normPk0+1) end

    if (integrate(parsedData[i],trStart+normPk0,trStart+normPk1) - bkGnd*(
        normPk1-normPk0+1)) < 1 then
        normRatio = 0 -- norm -- set counts to zero where normalization
        falls below the background
    else
        normRatio = norm/(integrate(parsedData[i],trStart+normPk0,
            trStart+normPk1) - bkGnd*(normPk1-normPk0+1))
    end

    end

    points.nu[n] = 1/(integrate(parsedData[i],trStart+normPk0,trStart+
        normPk1) - bkGnd*(normPk1-normPk0+1)) -- saving normalization ratio
        for error propagation
    if points.nu[n] ~= points.nu[n] then print(points.nu[n]) end
        -- shows if normalization = "nan"
    points.Nnorm[n] = integrate(parsedData[i],trStart+normPk0,trStart+
        normPk1) -- saving normalization peak counts for error propagation
    points.NA1[n] = integrate(parsedData[i],trStart+allPk0,trStart+allPk1
        ) -- saving Allison peak counts for error propagation
    if points.Nnorm[n]<1 then points.Nnorm[n] = 1 end -- prevent divide by
        zero errors

    bkGnd = normRatio*bkGnd      -- apply normalization to average
        background for foregoing calculations

```

```

points.x[n] = parsedData[i][2] * posCal
points.xp[n] = parsedData[i][voltCol] * 250*Leff/(KE*gap)*voltInvert
points.xp_err2[n] = points.xp[n]*points.xp[n] * ((V_errR*parsedData[i]
] [5]+4e-6*(volt1-volt0))^2 + (Leff_errR)^2 + (KE_err/KE)^2 + (
gap_errR)^2)

if normRatio*integrate(parsedData[i],trStart+alliPk0,trStart+alliPk1) -
bkGnd*(alliPk1-alliPk0+1) > thresh then
    points.Nx[n] = parsedData[i][2]*posCal * (normRatio*integrate(
        parsedData[i],trStart+alliPk0,trStart+alliPk1) - bkGnd*(
            alliPk1-alliPk0+1))
    points.Nxp[n] = parsedData[i][voltCol]*250*Leff/(KE*gap)*
        voltInvert * (normRatio*integrate(parsedData[i],trStart+
            alliPk0,trStart+alliPk1) - bkGnd*(alliPk1-alliPk0+1))
    points.N[n] = normRatio*integrate(parsedData[i],trStart+alliPk0
        ,trStart+alliPk1) - bkGnd*(alliPk1-alliPk0+1)
else
    points.Nx[n] = 0
    points.Nxp[n] = 0
    points.N[n] = 0
end
n = n + 1
end

local tot = integrate(points.N,1,#points.N)
local avgX = integrate(points.Nx,1,#points.Nx) / tot
local avgXP = integrate(points.Nxp,1,#points.Nxp) / tot

local dX2 = {}; for i=1, #points.x do dX2[i] = points.N[i]*(points.x[i] - avgX
)^2 end -- variance of x
local sdX2,avg_dX2 = integrate(dX2,1,#dX2), integrate(dX2,1,#dX2) / tot
-- save sum and average
local dXP2 = {}; for i=1, #points.xp do dXP2[i] = points.N[i]*(points.xp[i] -
avgXP)^2 end -- variance of x'
local sdXP2,avg_dXP2 = integrate(dXP2,1,#dXP2), integrate(dXP2,1,#dXP2) / tot
-- save sum and average
local dXdXP = {}; for i=1, #points.x do dXdXP[i] = points.N[i]*(points.x[i] -
avgX)*(points.xp[i]- avgXP) end -- covariance
local sdXdXP,avg_dXdXP = integrate(dXdXP,1,#dXdXP), integrate(dXdXP,1,#dXdXP)
/ tot -- save sum and average of covariance terms

local temp = avg_dX2*avg_dXP2 - avg_dXdXP^2
if temp < 0 then temp = 0 end -- prevent sqrt(negative) error
local emittance = math.sqrt(temp) -- pi mm mrad
local emitErr = 0
local avg_dX2_err,avg_dXP2_err,avg_dXdXP_err = 0,0,0

function errorCalc()
    function calcN_err(i,N) -- function for calculating error in N
        local nBGSD = 1 -- multiplicative factor on background
        error (not currently in use)
        if points.N[i] > thresh then --> thresh
            return points.nu[i]*math.sqrt( ((normPk1-normPk0+1)*N-(

```

```

        all iPk1-all iPk0+1))^2*points.ABG[i]/(bkGnd1-bkGnd0+1)
        + points.NAl[i] + N^2*points.Nnorm[i] + (0.02*N/
        points.nu[i])^2)
    else
        return 0
    end
end
end

if emittance > 0 then
    local sN_term = 0    -- summing over ( Ni_err/(2*N*emit) * [
        avgX2*(dXP2-avgXP2) + avgXP2*(dX2-avgX2) - 2*avgXXP*(dX*dXP-
        avgXXP) ] )^2
    local sx_term = 0    -- summing over ( xi_err /(emit)*Ni/N * [
        dX*avgXP2 - dXP*avgXXP ] )^2
    local sxp_term = 0   -- summing over ( xpi_err/(emit)*Ni/N * [
        dXP*avgX2 - dX*avgXXP ] )^2

    for i=1, #points.x do
        if points.nu[i] > 0 then -- and points.N[i] > thresh
            local Ni = points.N[i]/norm
            sN_term = sN_term + ( calcN_err(i,Ni)*norm/(2*tot
                *emittance) * ( avg_dX2*((avgXP-points.xp[i])
                ^2-avg_dXP2) + avg_dXP2*((avgX-points.x[i])^2-
                avg_dX2) - 2*avg_dXdXP*((avgX-points.x[i])*(
                avgXP-points.xp[i])-avg_dXdXP) ) )^2
            sx_term = sx_term + ( Ni*x_err*norm/(tot*
                emittance) * ( (avgX-points.x[i])*avg_dXP2 - (
                avgXP-points.xp[i])*avg_dXdXP ) )^2
            sxp_term = sxp_term + ( Ni*points.xp_err2[i]*norm
                /(tot*emittance) * ( (avgXP-points.xp[i])*
                avg_dX2 - (avgX-points.x[i])*avg_dXdXP ) )^2

            end
        end

        emitErr = math.pi*math.sqrt(sN_term + sx_term + sxp_term)
    else
        emitErr = 0
    end

    avg_dX2_err,avg_dXP2_err,avg_dXdXP_err = emitErr/emittance*avg_dX2,
        emitErr/emittance*avg_dXP2,emitErr/emittance*avg_dXdXP
end
errorCalc()

if thresh < 1e-12 then thresh = 1e-12 end
local pfac = maxPk/thresh
local ifac = pfac/(pfac-(1+math.log(pfac)))
local pfac_err = pfac/math.sqrt(maxPk)
local ifac_err = math.abs( math.log(pfac)*pfac_err/(1-pfac+math.log(pfac))^2 )
print("rms-emittance: " .. math.pi*emittance .. " +/- " .. emitErr .. " um")
print("Inflation factor: " .. ifac .. " +/- " .. ifac_err)
return math.pi*emittance,emitErr, ifac, avgX,avgXP, avg_dX2,avg_dXP2,avg_dXdXP
    , avg_dX2_err,avg_dXP2_err,avg_dXdXP_err -- [um]
end
end

```

```

-- Function to write emittance plot data
function writeEmitPlotData(sectionIndex0,sectionIndex1,pos0,pos1,posDelta,parsedData,
    filename)
    -- Process data
        local sec0,sec1 = 2, #parsedData
                                -- default range of
                                measurements to analyse
        if setSecBounds then sec0,sec1 = sectionIndex0+2,sectionIndex1+2 end --
            optional custom range of indices to analyse

        local position = pos0
        local points = {x = {}, xp = {}, N = {}}
        local BG1 = 0

        for i=sec0, sec1 do
            local bkGnd,BGSD,normRatio = 0,0,1.0

            local bkGndList = {}
            for j=1, bkGnd1-bkGnd0+1 do bkGndList[j] = parsedData[i][trStart
                +bkGnd0-1+j] end
            bkGnd = average(bkGndList)
            if i == sec0 then BG1 = bkGnd end

            local norm = (integrate(parsedData[sec0],trStart+normPk0,trStart
                +normPk1) - BG1*(normPk1-normPk0+1))-- integrate over first
                normalization peak for reference
            if (integrate(parsedData[i],trStart+normPk0,trStart+normPk1) -
                bkGnd*(normPk1-normPk0+1)) < 1 then
                normRatio = 0 --norm
            else
                normRatio = norm/(integrate(parsedData[i],trStart+normPk0
                    ,trStart+normPk1) - bkGnd*(normPk1-normPk0+1))
            end

            local counts = 0
            counts = round(normRatio*(integrate(parsedData[i],trStart+
                alliPk0,trStart+alliPk1) - bkGnd*(alliPk1-alliPk0+1)))
            if equalish(parsedData[i][2],position,0.1) then
                points.x[i-sec0+1] = position*posCal
                points.xp[i-sec0+1] = parsedData[i][1]*250*Leff/(KE*gap)*
                    ampRatio*voltInvert
                points.N[i-sec0+1] = counts
            elseif tonumber(parsedData[i][2]) < position-0.01*posDelta then
                i = i+1
            else
                position = position + posDelta
                points.x[i-sec0+1] = position*posCal
                points.xp[i-sec0+1] = parsedData[i][1]*250*Leff/(KE*gap)*
                    ampRatio*voltInvert
                points.N[i-sec0+1] = counts
            end
        end
    end
end

```

```

-- Calculate standard deviation of selected background region and identify
  peak counts
local peakMax = 0
local BGList = {}
local n=1
for i=1, #points.N do
  if points.x[i] >= tMinX and points.x[i] <= tMaxX and points.xp[i] >=
    tMinXP and points.xp[i] <= tMaxXP then
    BGList[n] = points.N[i]      -- gather counts in selected
      background region for calculating SD
    n = n+1
  end
  if peakMax < points.N[i] then peakMax = points.N[i] end
end
local BGSD = stdDev(BGList)

-- Write data to file
local f = assert(io.open(string.format("%s_emit.txt", filename), 'w'))
  f:write(string.format("#Position (mm)\tDivergence (mrad)\tNormalized
    Counts\n"))
  if points.N[1] < threshold*BGSD then
    f:write(string.format("%f\t%f\t%d\n", points.x[1],points.xp
      [1],0))
  else
    f:write(string.format("%f\t%f\t%d\n", points.x[1],points.xp[1],
      points.N[1]))
  end
  for i=2, #points.x do
    if points.N[i] < threshold*BGSD then
      if points.x[i] > points.x[i-1]+0.2*posDelta then
        f:write(string.format("\n%f\t%f\t%d\n", points.x[i]
          ],points.xp[i],0))
      else
        f:write(string.format("%f\t%f\t%d\n", points.x[i],
          points.xp[i],0))
      end
    else
      if points.x[i] > points.x[i-1]+0.2*posDelta then
        f:write(string.format("\n%f\t%f\t%d\n", points.x[i]
          ],points.xp[i],points.N[i]))
      else
        f:write(string.format("%f\t%f\t%d\n", points.x[i],
          points.xp[i],points.N[i]))
      end
    end
  end
end
f:close()

-- Calculate rms-emittance
local emittance,emitErr, ifac, avgX,avgXP, x2,xp2,xxp, x2_err,xp2_err,xxp_err
  = rmsEmit(sec0,sec1,alliPk0,alliPk1,parsedData,threshold*BGSD,peakMax)
end
if _writeEmitPlotData then writeEmitPlotData(sectionIndex0,sectionIndex1,pos0,pos1,

```

```
posDelta,parsedData,outputFilename) end
```